Fritz Haber Institute of the Max Planck Society
Department of Physical Chemistry
Research Group Melanie Müller

Master's thesis

Light-Matter Interaction of Ultra-thin ZnO Films on Ag(111) investigated by STM-induced Luminescence

Henrik Wiedenhaupt

Freie Universität Berlin

Examining board:

Prof. Dr. Martin Wolf
Fritz Haber Institute of the Max Planck Society,
Department of Physical Chemistry

Prof. Dr. Thomas Risse
Freie Universität Berlin,
Department of Biology, Chemistry, Pharmacy

12. September 2022 - 27. March 2023

Contents

1 Introduction

The wide range of functional properties of oxide materials from superconducting to semiconducting and insulating properties makes them important for technical applications.[1] In the past, a lot of studies have been done on bulk oxide materials with the first research on ZnO dating back many decades.[2, 3, 4, 5, 6] The development of thin-film deposition techniques has made it feasible to grow epitaxial thin oxide films on substrates.[7] The transition from bulk oxides to oxide films and the reduction of the film thickness to a few monolayers (ML, ultra-thin films) revealed functional properties depending on its thickness.[8, 1] Besides the usage of ultra-thin oxide films on well-defined metal surfaces as model supports for metallic nanoparticles[9] and as model systems in heterogeneous catalysis[10], they themselves exhibit interesting properties deviating from their bulk properties originating from confinement effects and electronic and structural interactions at the interface.[11, 12] Nowadays, a large number of important applications of oxide films (including ZnO-based materials) are already known such as heterogeneous catalysis, electronic devices, gas sensors and optoelectronics.[10, 13, 14, 15, 12, 16, 17, 18] For instance, the heterogeneous catalyst $Cu/ZnO/Al_2O_3$ plays an important role for the methanol synthesis.[19, 16] This wide variety in applications of ZnO-based materials is originating from the attractive structural, electronic and optoelectronic properties of ZnO such as the wide direct band gap ($\approx 3.3\,\mathrm{eV}$), which can be tuned by doping, and the large exciton binding energy ($\approx 60\,\mathrm{meV}$).[6, 20] Important physical properties which depend on the thickness are lattice constants, the band gap, the work function and optoelectronic properties.[12, 21] Defects in the oxide films alter the electronic structure and their properties.[6] In order to locally probe ultra-thin oxide films and their properties, spectroscopic and imaging methods with high spatial resolution in the Ångström range such as Scanning Tunneling Microscopy (STM) are applied.[22, 12] Surface science was revolutionized by the invention of STM in 1981 by Heinrich Roher and Gerd Binnig which was awarded the Nobel Prize in Physics in 1986.[23, 24] STM enables the investigation of the surface morphology of conducting samples with very high spatial resolution originating from the exponentially vanishing tunneling current between the metallic tip and conducting surface.[25] By sweeping the bias voltage between tip and surface, the local electronic structure of the surface sample is accessible (Scanning Tunnel-

ing Spectroscopy, STS).[26] By means of STM-induced Luminescence (STML), inelastic electron tunneling in the STM junction can locally excite molecules or extended systems whose luminescence is detected and analyzed with a high spatial resolution down to the sub-nanometre regime.[27, 28, 29, 30] For instance, STML elucidates quasiparticles such as localized surface plasmons (LSPs)[31, 30] and excitons in semiconductors[32], electronic and vibrational structures[28, 33, 34], dipole-dipole coupling between monomers[35] and energy transfer between molecules[36] and between a LSP and a molecular exciton[37].
The first ZnO layers on the Ag(111) surface with ordered domains have been prepared by Kourouklis and Nix in the year 1994.[38] In the last decade, the topography and electronic structure of ultra-thin ZnO layers on Ag(111) have been studied.[39, 40, 12, 41, 42] While Pan et al. only observed the bilayer ZnO (2 ML) on Ag(111), Shiotari et al. observed also trilayers (3 ML).[39, 40] Liu et al. measured the conduction band edge (CBE) at 1.8 V and 1.6 V for 2 ML and 3 ML, respectively.[42] The surface state of the bare Ag(111) becomes an interface state (IS) in the ZnO/Ag(111) system at -0.2 V such that the transition between IS and the CBE requires 2 eV and 1.6 eV for 2 ML and 3 ML, respectively.[42] The IS to CBE transition of 2 ML and 3 ML ZnO on Ag(111) plays an important role in TERRS (Tip-Enhanced Resonance Raman Spectroscopy) as chemical enhancement is necessary to strongly enhance the signal.[42] A recent study of Liu et al. showed much larger photo-currents on 3 ML ZnO compared to 2 ML ZnO with a 780 nm fs-laser (1.6 eV).[43] The IS-CBE resonance in the 3 ML ZnO film was used to locally probe coherent phonons with a spatial resolution of about 2 nm.[43] The understanding so far is that the coherent phonons modulate the electronic structure of the 3 ML ZnO film and thus the probability of the IS-CBE transition which has an influence on the measured photo-current.[43]
In this thesis, the light-matter interaction of ultra-thin ZnO films on Ag(111) has been investigated by means of low-temperature STML. The mentioned previous studies on TERRS and nanoscale coherent phonon spectroscopy on ultra-thin ZnO films on Ag(111) indicate a strong coupling between the localized surface plasmon of the junction and the IS-CBE transition.[42, 44] Preliminary STML measurements of the group of M. Müller showed a relative reduction of higher photon energies. Krane et al. observed only a plasmonic response from the Au(111)-Au tip STM junction on the MoS_2 monolayer on Au(111).[30] However, the transition metal dichalcogenide on Au(111) exhibits no (occupied) interface state in the band gap and the IS-CBE transition in ultra-thin ZnO films on Ag(111) promotes some interesting physical behaviour.[30, 43, 42] Hence, the hypothesis is examined whether the observed quenching of higher photon energies of the alleged plasmon might originate from an energy transfer with the IS-CBE transition. Up until now, only the interaction of the local-

ized surface plasmon of the junction with discrete (electronic) states of single molecules via energy transfer resulting in fano lineshapes has been described in the literature.[37, 27, 45] This investigation might also help to better understand preceding studies on ultra-thin ZnO films on Ag(111) such as the mentioned study on coherent phonons and their excitation via displacive excitation.[43]

The next chapter covers the theoretical background which describes the theory behind the experimental methods and the system at hand. Following, the experimental details are explained. In the fourth chapter, the results are shown and discussed starting with the bias-dependent STML measurement on bare Ag(111) followed by bias-dependent STML measurements on 2 and 3 ML ZnO at positive and negative bias voltages as well as spatially resolved STML measurements. In the last part of the thesis, the results are summarized and an outlook for further measurements is given.

2 Theoretical Background

In the first section 2.1, Scanning Tunneling Microscopy (STM) is introduced alongside with Scanning Tunneling Spectroscopy (STS, in 2.1.1), STM-induced Luminescence (STML, in 2.1.2) and plasmon-assisted resonant electron tunneling (2.1.3). The subsequent section 2.2 describes the plasmonic cavity of a Ag tip on Ag(111) with a description of the Ag(111) surface (2.2.1) and general introduction on localized surface plasmons (2.2.2). The fourth and last section 2.3 describes the state of knowledge on ultra-thin ZnO layers on Ag(111) subdivided in atomic (2.3.1) and electronic structure (2.3.2).

2.1 Scanning Tunneling Microscopy (STM)

Scanning Tunneling Microscopy (STM) was invented in 1981 by Heinrich Rohrer and Gerd Binnig who later won the Nobel Prize in Physics in 1986 for their invention.[23, 24] STM revolutionized surface science due to its ability to image conducting surfaces with very high spatial resolution in real space.[46, 47] One could even use the tunneling electrons to locally probe the electronic and plasmonic structure and vibrational and optical properties of surfaces and single molecules with high spatial resolution by means of Scanning Tunneling Spectroscopy (STS) (see subsection 2.1.1) and STM-induced Luminescence (STML) (see subsection 2.1.2).[26, 48, 31, 32, 33, 30, 28, 34, 37]
This high spatial resolution of conducting surfaces is achieved by exploiting the quantum-mechanical tunnel effect and its exponentially vanishing tunnel current between a metal tip and the conducting surface (see equation 2.3) if a bias voltage V_{bias} is applied to the junction. The tunnel effect describes the ability of electrons to tunnel across a potential barrier which is classically forbidden. Figure 2.1 exhibits the tunneling effect in one dimension with a tip-sample distance d, the Fermi levels of tip and sample $E_{\mathrm{F}}^{\mathrm{t}}$ and $E_{\mathrm{F}}^{\mathrm{s}}$, the work functions Φ^{t} and Φ^{s} and the vacuum levels $E_{\mathrm{vac}}^{\mathrm{t}}$ and $E_{\mathrm{vac}}^{\mathrm{s}}$. The electron wave function Ψ in one-dimension for a rectangular barrier with potential Φ is given by

$$\Psi(d) = \Psi(0)e^{-kd} \tag{2.1}$$

with

$$k = \frac{\sqrt{2m(\Phi - E)}}{\hbar} \tag{2.2}$$

where m is the electron mass and E the energy of the tunneling electron.[46] The tunneling current I is proportional to the probability distribution. Using eV as the unit of the work function and Å as unit of the decay constant following relation is obtained[49]:

$$I \propto \exp(-1.02\sqrt{\Phi(eV)}\text{Å}^{-1}d). \tag{2.3}$$

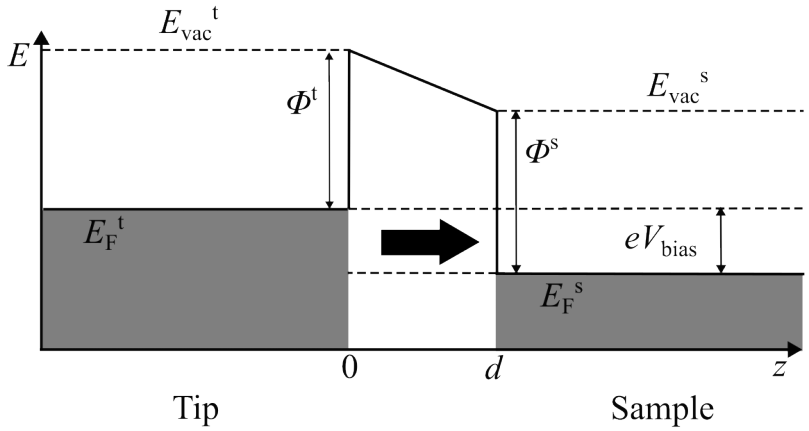

Figure 2.1: One-dimensional energy diagram of the quantum-mechanical tunnel effect: Electrons tunnel from tip (t) to surface sample (s) with distance d. Denoted are the vacuum levels E^{s}_{vac} and E^{t}_{vac}, Fermi energies E^{s}_{F} and E^{t}_{F}, work functions Φ^{s} and Φ^{t} and the potential difference V_{bias}. Figure drawn according to [46].

Work functions of metals are typically around 5 eV.[50] Thus, the tunneling current decreases by about one order of magnitude by increasing the distance d by 1 Å which renders the tunneling current very localized under the tip apex.[50] A theoretical extension of the tunneling current I to the three-dimensional STM junction for a small bias voltage can be done by the approach of Bardeen[51] and the Tersoff-Hamann approximation[52, 53]:

$$I \propto \rho_{t}(E_{F})\rho_{s}(r_{0}, E_{F}) \tag{2.4}$$

with the density of states (DOS) of the tip $\rho_{t}(E_{F})$ and the local DOS of the sample surface

at E_F and the position of the tip apex r_0 given by[46]

$$\rho_\mathrm{s}(r_0, E_\mathrm{F}) = \sum_\mathrm{s} |\Psi_\mathrm{s}(r_0)|^2 \delta(E_\mathrm{s} - E_\mathrm{F}). \tag{2.5}$$

Thus, the tunneling current additionally depends on the LDOS of the sample surface.[46] In order to obtain a two-dimensional image of the sample surface, the metal tip scans the conducting sample surface in a grid with a certain distance while a bias voltage is applied (see Figure 2.2). The requirement of a very precise control of the tip position is realized by three piezoelectric elements as shown in Figure 2.2. The resulting tunneling current is detected and amplified at each position. One has to distinguish two imaging modes: constant height mode and constant current mode.[46] In constant height mode, the absolute height is held constant which leads to a change in the distance between surface sample and tip. This change causes a change in the tunneling current which is imaged. In the constant current mode, the tunneling current is held constant by a so-called feedback loop. Thus, the distance between sample surface and tip is similar at each position if the local DOS does not vary across the scanned area. In this case the sample's topography is obtained by plotting the absolute height of the tip. Compared to constant height mode, a drawback of constant current mode is the longer acquisition time due to the feedback loop. However, the constant current mode and feedback loop can prevent the tip from crushing into the sample surface which has e.g. step edges.[46]

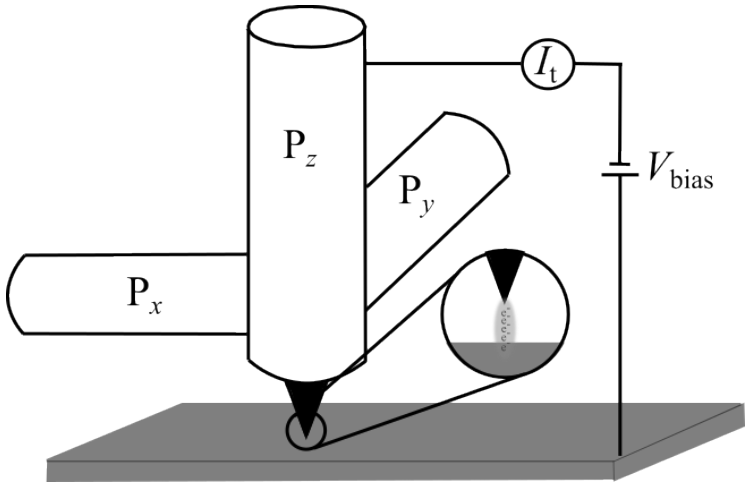

Figure 2.2: Schematic principle of STM. A bias voltage V_bias is applied between a very fine tip and a conducting sample surface with atomic distance which leads to a tunneling current I_t. The tip is precisely positioned by three piezocrystals. Figure drawn according to [46].

STM is commonly operated under ultrahigh vacuum (UHV) conditions and at cryogenic temperatures (Low-Temperature STM, LT-STM) because it is crucial to have a clean surface and the drift of the piezodriven tip is reduced as well as the base pressure and the thermal noise.[46]

2.1.1 Scanning Tunneling Spectroscopy (STS)

As seen in the previous subsection and in eq. 2.4, the tunneling current depends on the electronic structure of the surface which enables us to probe the surface electronic structure with high spatial resolution. By further elaborating eq. 2.4, the tunneling current for small bias voltages can be obtained by integration over the electron energy, giving the following equation

$$I(r_0, V) = \frac{2\pi}{\hbar} \int_{E_\mathrm{F}}^{E_\mathrm{F}+eV} \rho_\mathrm{t}(r_0, E - eV) T(r_0, E - eV) \rho_\mathrm{s}(r_0, E)\, dE \tag{2.6}$$

with the transmission coefficient T which depends on the energy of the involved states, the bias voltage, the sample-tip distance and the work functions of sample and tip.[46, 54] Thus, the three parameters tunneling current, bias voltage and sample-tip distance are interconnected. STS can be done by measuring the relation between two parameters (f.e. bias voltage and tunneling current, I-V curves) and by keeping the third parameter fixed (here the sample-tip distance).[54] Under the assumption of a constant tip DOS and transmission coefficient in the voltage range, the tunneling current differentiated with respect to the bias voltage (differential conductance) is proportional to the sample surface local DOS at the potential difference eV:

$$\frac{dI}{dV} \propto \rho_\mathrm{t}(r_0, E_\mathrm{F}) T(r_0, E_\mathrm{F} + eV) \rho_\mathrm{s}(r_0, E_\mathrm{F} + eV). \tag{2.7}$$

Thus, the electronic structure of the sample surface is probed by determining the differential conductance.[54] Fig. 2.3 exhibits the principle of STS schematically with sample DOS. By changing the sign of the bias voltage, it is possible to not only probe unoccupied sample states but also occupied sample states by applying a positive (Fig. 2.3 A) and negative bias voltage (Fig. 2.3 B), respectively.[46] Experimentally, the differential conductance is obtained by using a lock-in amplifier. The bias voltage V_bias is modulated with a sinusoidal voltage V_mod with frequency ω:

$$V_\mathrm{bias} = V_0 + V_\mathrm{mod} \sin(\omega t). \tag{2.8}$$

However, the modulation voltage V_{mod} has to be small with respect to V_0. Hence, this modulation causes a sinusoidal response in the tunneling current which can be Fourier decomposed with respect to the frequency ω:

$$I(V_{\mathrm{bias}}) = I_0 + V_{\mathrm{mod}} \frac{dI(V_{\mathrm{bias}})}{dV} \sin(\omega t) + \frac{1}{4} V_{\mathrm{mod}}^2 \frac{d^2 I(V_{\mathrm{bias}})}{dV^2} \sin(2\omega t) + \dots \,. \tag{2.9}$$

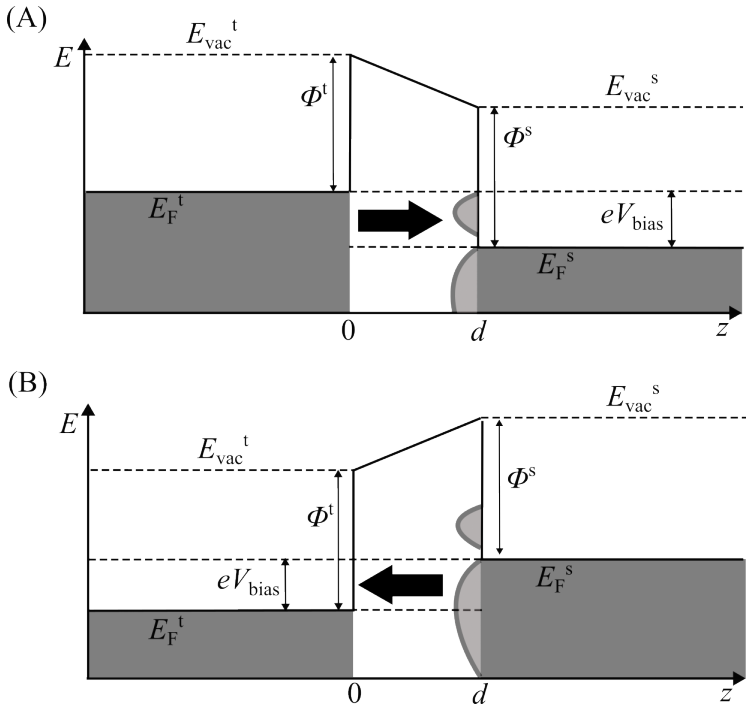

Figure 2.3: Scanning Tunneling Spectroscopy (STS) with positive bias voltage to probe unoccupied states of the sample surface (A) and negative bias to probe occupied states of sample surface (B). Figure drawn according to [46].

The second summand (first harmonic) is proportional to the differential conductance ($\frac{dI}{dV}$). The amplitude can be determined by lock-in detection. The electronic structure can be probed by measuring the differential conductance in constant tunneling current mode such that the feedback loop is on and the tip is retracted while the bias voltage is swept.[12, 54] However, the signal obtained from the lock-in detection is not proportional to the local DOS of the surface anymore because the gap distance changes. The obtained differential conductance is proportional to $\frac{dz}{dV}$.[12, 54] Compared to constant height measurements, a much larger range of differential conductance signal can be measured in the constant current measurement.[12] Stepwise changes in the spectra of constant height measurements appear as peaks in the constant current measurements because when the DOS increases the tip

is retracted by the feedback loop in order to keep the current constant.[12] There is also the possibility to map the differential conductance by setting the bias voltage to a distinct state and using lock-in detection. This can be done parallel to taking a constant current topographic image.[46, 54]
Besides the elastic tunnel process, there can be inelastic electron tunneling caused by excitation of vibrations ($\hbar\omega$) of adsorbed molecules on the surface sample. The opening of inelastic channels renders vibrational spectroscopy feasible (Inelastic electron tunneling spectroscopy, IETS).[55, 56] As an inelastic channel opens, the differential conductance increases slightly which is seen in the derivative of the differential conductance. In order to determine this derivative, the third summand (second harmonic) is determined using lock-in detection.

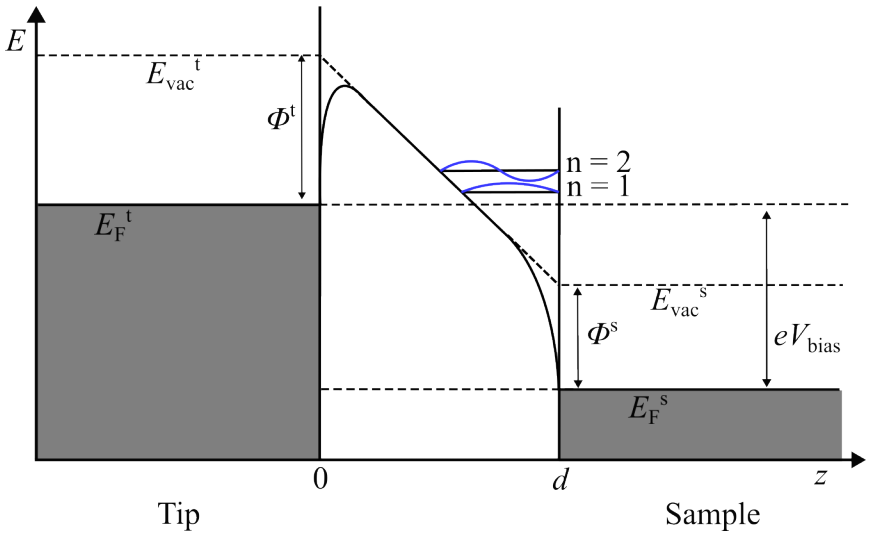

Figure 2.4: Schematic energy diagram of the STM junction with a bias voltage larger than the sample's work function. The first two FER states are shown in the triangular potential which present the standing electron waves in the junction. Figure drawn according to [54].

At high bias voltages when it exceeds either the tip or the sample work function, the STS spectra show not only features of the samples DOS but also tunneling through field emission resonance (FER) states which are the result of standing electron waves in the STM junction as shown in Fig. 2.4.[22, 54] These FER states exist in a nearly triangular potential well resulting from the crystal potential and the field potential from the bias applied (see Fig. 2.4).[22, 54] In the STS spectra (constant current measurement), the FER states appear as a Rydberg-like series.

2.1.2 STM-induced Luminescence (STML)

The first reports of light emission (luminescence) from a tunneling junction consisting of two metallic electrodes separated by a thin oxide layer are from 1976[57] and from a STM junction consisting of an iridium tip and polycrystalline tantalum from 1988.[58] As already seen in the previous subsection, electrons can inelastically tunnel between the tip and the sample surface and lose energy during electron tunneling (see Fig. 2.5). Although inelastic tunneling is the bedrock of STML, the origin of the luminescence depends on the matter in the STM junction. Inelastic electron tunneling in the STM junction can locally excite localized surface plasmons (LSP), molecules and extended systems (excitons and vibrations) whose luminescence is detected and analyzed with a very high spatial resolution down to the sub-nanometre regime.[32, 33, 59, 27, 28, 29, 30, 34, 37]

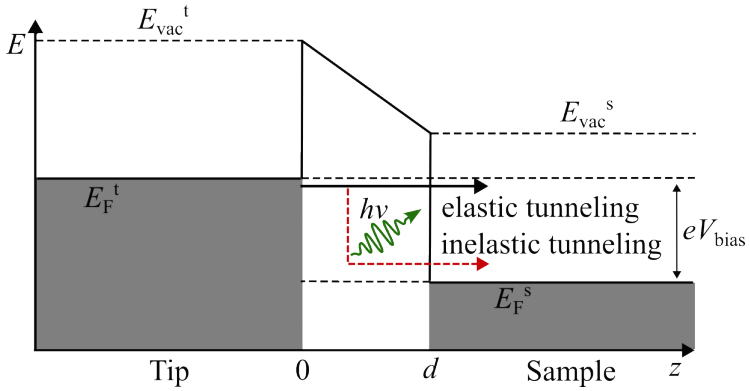

Figure 2.5: One-dimensional energy diagram of the STM junction exhibiting elastic and inelastic tunneling processes. Inelastic tunneling can excite the LSP of the junction, excitons in semiconductors and single molecules adsorbed on the surface. The detected luminescence originates from the radiative decay of the excited states. Figure drawn according to [60].

The observed luminescence from a coin metal STM junction is broadband and the luminescence's cutoff matches the energy of the bias applied between tip and substrate.[59] Thus, this quantum cutoff is determined by the bias voltage (see Fig. 2.6 (A)). The observed luminescence originates from the excitation and radiative decay of the LSP of the STM junction.[59] The broadbandness is originating from inelastic tunneling with transitions of smaller energies.[61] LSPs generate strong field enhancement and are associated with the collective oscillation of conduction electrons of sample and tip along the tip-sample axis (more details on plasmons in subsection 2.2.2).[60, 31]

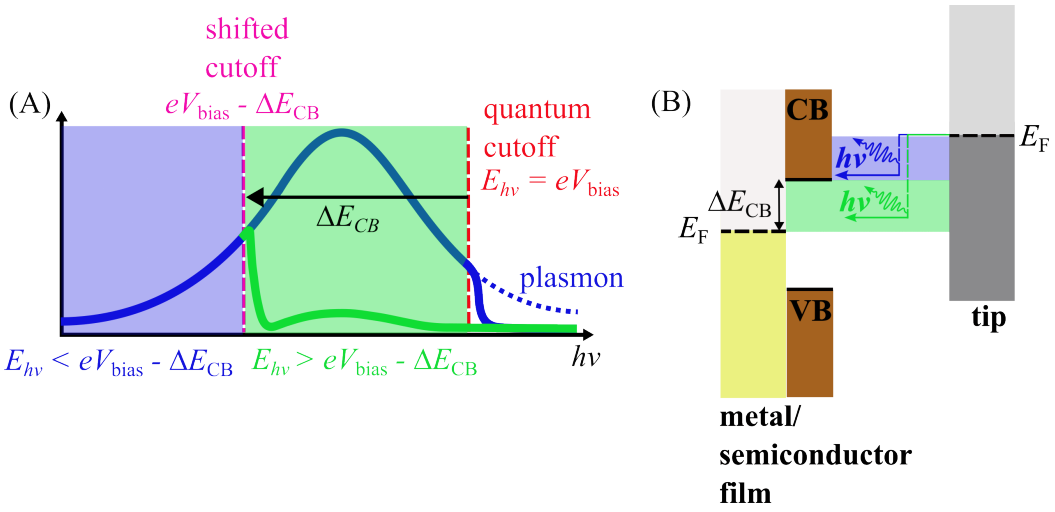

Figure 2.6: (A) The luminescence (plasmonic response) shows a quantum cutoff at the bias voltage ($eV_{\text{bias}} = E_{h\nu}$). Additionally, it might be quenched above a shifted cutoff ($eV_{\text{bias}} - \Delta E_{\text{CB}}$) as observed by Krane et al.[30] due to a lack of DOS in the band gap. (B) The energy diagram elucidates where the shifted cutoff originates from.

By means of STML, Krane et al. investigated the electronic structure and band gap of a two-dimensional semiconductor MoS_2 on Au(111) with high spatial resolution.[30] Their investigation comprised the measurement of STML spectra in dependence of the bias voltage.[30] They reported that there is an additional shifted cutoff of the luminescence by the conduction band edge (CBE) energy ($eV_{\text{bias}} - \Delta E_{\text{CB}}$) due to a lack of DOS in the band gap (see Fig. 2.6 (A) and (B)) of quasi-freestanding MoS_2 nanopatches on Au(111) whereas this shifted cutoff was missing for MoS_2 on Au(111) due to inelastic tunneling into the band gap.[30] The luminescence was ascribed to a purely plasmonic (extrinsic) origin.[30, 61] Below the shifted cutoff, the inelastic tunneling rate is higher because of a high DOS of MoS_2 in the CB.[30] Above this shifted cutoff, the DOS inside the band gap is low and thus the inelastic tunneling rate.[30] Hence, the final state of the tunneling electron and the corresponding DOS determine the inelastic tunneling rate.[30] Schuler et al. also observed a plasmonic (extrinsic) response due to inelastic tunneling into the CB and additionally into discrete defect states on monolayers of WS_2 on 2LG/SiC.[62] Other studies on TMDs revealed intrinsic luminescence originating from the formation of excitons and their radiative recombination.[63, 64] The formation of the exciton can be caused by either energy transfer[63] or charge injection[64]. In order to excite excitons via energy transfer, the bias voltage has to be equal or larger than the corresponding transition (optical bandgap) independent on the polarity.[61] The requirement for excitation

via charge injection is electron tunneling into the CB or from the VB of the emitting medium.[61] Hence, there is a correlation between the electronic structure and observed luminescence.[61] So far, only STML studies on TMDs have been discussed, but there are also STML studies on thin oxide films on metal substrates.[29, 21] Stavale et al. reported to not only observe the band recombination peak but also multiple peaks related to defects in ZnO$(000\bar{1})$/Au(111).[29] They ascribed the hole formation in the VB and defect states to the ionization by electrons from the tip.[29] Nilius et al. investigated the luminescence of thin Cu_2O films on Au(111) and observed an interesting bias dependence at positive bias voltages.[21] At bias voltages matching the CBE of the thin Cu_2O films a strong and broad response was observed and above the CBE the STML intensity (integral intensity) was reduced.[21] Nilius et al. ascribed this behaviour to tunneling into the CB of Cu_2O and radiative transition with initial states at the CBE and final states close the Fermi level whereby the luminescence's nature is plasmonic.[21] According to them, the CB states near the CBE are more localized and have a higher recombination probability with holes and hence are more light emitting.[21] At higher bias voltages the electrons tunnel into more delocalized states which are then transported to the interface and into the Au bulk (non-radiative loss).[21] Fig. 2.7 summarizes the observation on thin Cu_2O films on Au(111) and the explanation from Nilius et al.[21] Another way to reduce the plasmonic response of the junction (integral intensity) is by opening new tunneling channels such as tunneling via FER states observed in a Ag tip-Ag(111) junction by Martínez-Blanco et al.[59]
The detection of single-molecules (ultrasensitive spectroscopy) is only feasible due to the LSP with its strong field enhancement (Purcell effect).[31, 65, 32, 66] In order to decouple the adsorbed molecules from the metal surface, thin insulating films of NaCl have been used.[35, 34] Doppagne et al. resolved vibrational features of the fluorescence of the phthalocyanine molecule on NaCl/Ag(111) with a submolecular spatial resolution.[34] The same molecule was used in studies to spatially investigate the dipole-dipole coupling between multiple monomers resulting in a larger transition dipole.[35] Imada et al. showed that STML is able to probe resonance energy transfer between a heterogeneous dimer.[36] They reported in a different study that the LSP and a molecular exciton interact via energy transfer (see Fig. 2.8) which results in fano lineshapes and showed the lateral distance dependence.[37]

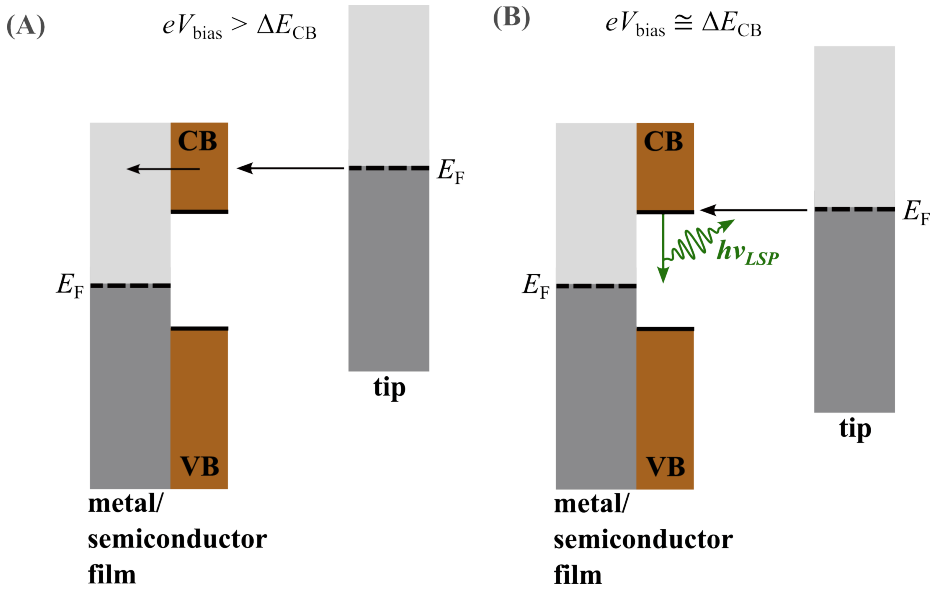

Figure 2.7: (A) Tunneling into more delocalized CB states of the thin semiconductor film which leads to non-radiative loss due to transport into the metal bulk. (B) Tunneling into CBE states which are spatially more localized and show strong luminescence. Figure drawn based on reference [21].

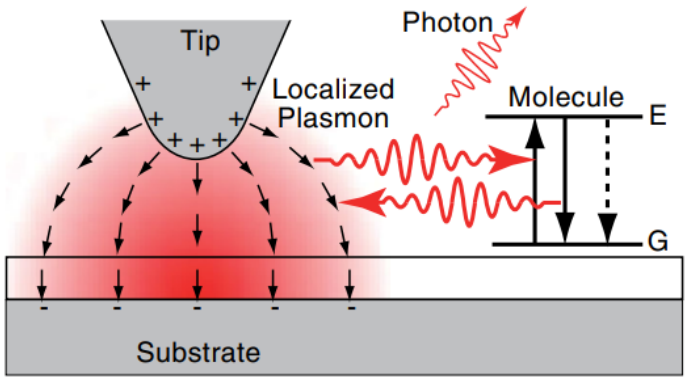

Figure 2.8: Schematic drawing of the plasmon-exciton interaction via energy transfer. The transitions in the molecule are from ground state (G) to excited state (E). Taken from reference [37].

2.1.3 Plasmon-Assisted Resonant Electron Tunneling in STM

Besides tunneling with electrons exhibiting energies around the Fermi level as depicted in Fig. 2.1, plasmon-assisted tunneling is also observed in STM junctions.[31] As shown in Fig. 2.9, plasmon-assisted tunneling of an electron is observed from an excited state of the tip and the electrons tunnel through the potential barrier if an electronic state is available

at the corresponding energy.[31] Both channels compete with each other.[31]
Conducting STM experiments with optics for focusing light into the STM junction, Liu et al. found the shift in the STS spectra of FER states (Rydberg-like electronic states) with and without illumination of STM junctions consisting of a Ag tip or a Au tip on a Ag(111) surface corresponds to the incident photon energy.[31, 22] Thus, plasmon-assisted resonant tunneling for these systems is achievable through FER states in the STM junction.[31] By examining the shift with both tips, various incident photon energies and p- and s-polarization, they concluded that field enhancement from LSPs is fundamental.[31] This light-induced shift can be used to characterize the plasmonic response of the Ag tip on the Ag(111) surface.

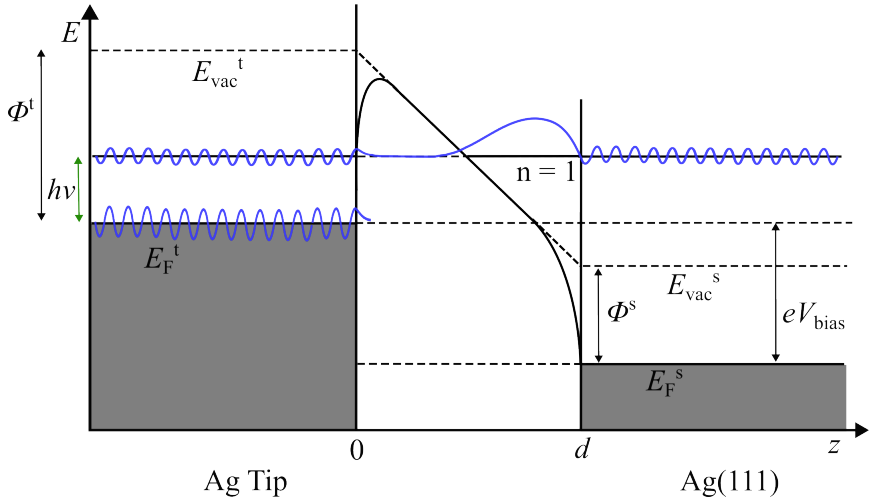

Figure 2.9: Energy diagram of the Ag tip-Ag(111) surface STM junction under illumination with the incident photon energy ($h\nu$) and the first FER state (n = 1) shown. The solid blue lines represent the electron wave functions. The bias voltage (eV_{bias}) fulfills $eV_{\textbf{bias}} = E_{\text{FER, n=1}} - h\nu$ where $E_{\text{FER, n=1}}$ is the energy of the first FER state with respect to the Fermi level. This figure was drawn according to [31].

2.2 Ag Tip on Ag(111) Surface: Plasmonic Cavity

2.2.1 Ag(111) Surface

Silver (Ag) is a transition metal and crystallizes in a face-centered cubic structure (fcc structure) with a lattice constant of 4.079 Å.[67] The band structure of Ag close to the regime of the Fermi level (E_F) consists of a broad, nearly-free-electron-like s-p band which overlaps and hybridizes with a narrow d-band complex.[68] As for an element of the 11th group, the d-bands are full. The position of the d-band relative to E_F is about $-3.5\,\text{eV}$ which

makes interband transitions with visible light impossible.[68] Cutting the bulk such that the (111) surface is exposed (as depicted in Figure 2.10), yields a hexagonal surface structure (closest-packed surface) with an interatomic distance of 2.98 Å.[40] The step height of Ag(111) is 2.36 Å.[40] The surface state of the Ag(111) surface is found close to the Fermi level (E_F) between −0.08 eV and −0.06 eV.[12] A clean Ag(111) surface has a work function of 4.74 eV according to photoemission spectroscopy.[69] Due to silvers negative and complex dielectric function, it supports strong surface plasmons in the visible light regime.[60, 70] If the cutoff energy of the plasmons in STML is not determined by the quantum cutoff, it is determined by the interband transition which is around 4 eV for Ag.[31, 71, 59]

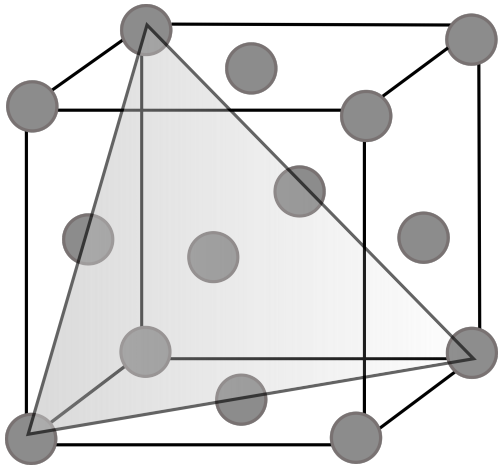

Figure 2.10: Schematic drawing of Ag atoms (light grey) in fcc structure. Diagonal plane represents (111) surface.

2.2.2 Localized Surface Plasmons

The collective oscillations of the electrons about the positive ions in the metal bulk are termed bulk plasmons.[61] If the real part of the dielectric constant changes sign across the interface, similar oscillations occur at the interface. These so-called propagating surface plasmons are associated with collective oscillations of free conduction electrons which create confined electromagnetic waves that propagate along the interface between a metal and a dielectric as depicted in Fig. 2.11 (A).[60] As depicted in Fig. 2.11 (A), the electric field is normal to the surface. They are non-radiative due to the exponential decay of the electric field and do not couple to photons because the momentum of a surface plasmon is always larger than of a photon with the same energy (momentum mismatch). However, defects on the surface which break the symmetry or the interaction with tunneling electrons permit

the radiative decay.[60, 72]
Charge oscillations inside metallic nanoparticles are confined to its volume and hence called localized surface plasmons (LSP). These localized surface plasmon modes intrinsically couple to photons. By placing a nanostructure such as a metallic tip above a metallic surface, the LSP of the tip and surface plasmon of the metallic surface hybridize and create LSPs inside the STM junction (sometimes referred as gap plasmons).[61] So these LSPs in a STM junction are collective oscillations of conduction electrons of tip and sample along the tip-sample axis (see Fig. 2.11 (B)).[60] The resonance modes of the LSP are spatially localized in the STM junction. These LSPs can be excited by either electrons or photons and the corresponding luminescence from the radiative decay is broad in nature. The structure of the STM tip apex and the dielectric properties of tip and surface have an effect on the plasmon and the spectral characteristics of its light emission.[73, 74, 75, 59, 76] Martínez-Blanco et al. showed that the LSP modes of a Ag tip on Ag(111) strongly depend on the tip geometry.[59] Independent on the exact plasmonic structure, the intensity in a STML spectra covers almost the whole visible light range.[31, 59] It has been shown that the plasmonic structure of a STM junction can be manipulated by applying a focused ion beam (FIB).[73]

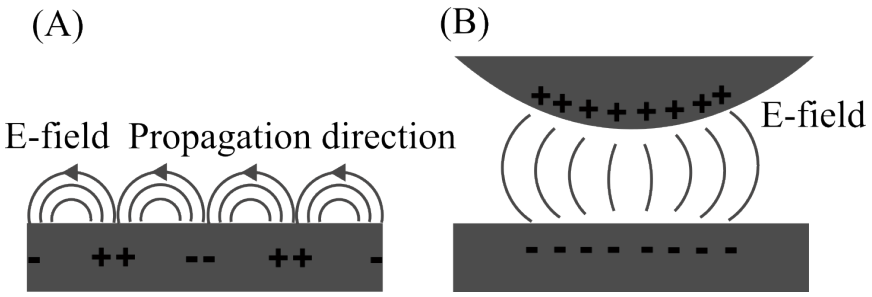

Figure 2.11: Scheme of a surface plasmon propagating along the interface of a metal and a dielectric which exponentially decays normal to the interface (A) and of a localized surface plasmon (LSP) in a STM junction (B). LSPs shows strong field enhancement. The electric fields are represented by gray lines. Figure drawn according to [77].

The LSP shows enhancement in two processes: excitation and radiation.[78, 79] The plasmonic field which can be excited by incident light, is strongly enhanced with respect to the electromagnetic field of the incident light.[60] This strong enhancement is responsible for the observed plasmon-assisted resonant electron tunneling in the Ag tip-Ag(111) junction described in the previous section when exciting with p-polarized light.[31] Hence, the

excitation rates are increased by many orders of magnitude.[60, 31] The light of the radiative decay is also enhanced due to an increase in the decay rate by coupling to the LSP modes.[60, 80] This is the so-called Purcell effect which describes the enhancement of the radiative decay rate of an emitter in a resonator due to the high photonic DOS originating from the LSP modes.[66, 81]

2.3 Ultra-thin ZnO Layers on Ag(111) (ZnO(0001)/Ag(111))

2.3.1 Atomic Structure

The wurzite structure (as depicted in Fig. 2.12) is the most stable structure of bulk ZnO at ambient conditions.[6] The zinc atoms form a hexagonal close-packed (hcp) sublattice while the oxygen atoms occupy half the tetrahedral sites. Each atom in bulk ZnO exhibits a tetrahedral coordination. Bulk ZnO is a wide band-gap semiconductor.[6]
Kourouklis and Nix prepared the first ZnO layers via oxidation of Zn films on various silver surfaces (low indices) and reported based on low-energy electron diffraction (LEED) that ordered domains appeared just upon annealing to 500 K.[38, 40] The structure of the ordered domains was similar to ZnO(0001) which is a polar surface with a dipole moment normal to the surface.[38, 82, 40] The (0001) plane is also shown in Fig. 2.12.

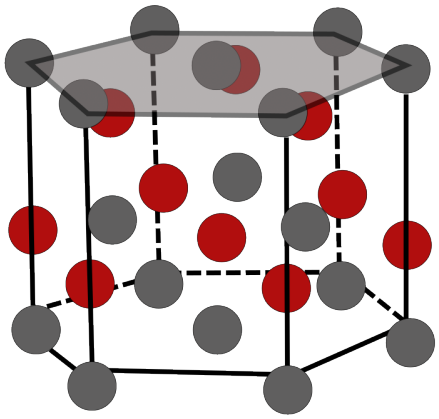

Figure 2.12: Schematic drawing of the wurzite structure with the Zn atoms (dark grey) forming a hcp sublattice and O atoms (red) filling half the tetrahedral sites. The grey plane represents the (0001) surface.

Shiotari et al. studied the structure of ZnO layers on Ag(111) locally at 5 K using non-contact atomic force microscopy (nc-AFM) and LT-STM.[40] The ultra-thin layers were

grown on Ag(111) by the reactive deposition method based on a publication from Pan et al.[39] Zinc is deposited on the Ag(111) surface at room temperature with a O_2 background (1×10^{-5} mbar) followed by annealing to 600 K.[39] While the results of Pan et al. based on LEED, AES and STM suggested only the growth of bilayer ZnO (2 ML) on the Ag(111) surface, Shiotari et al. suggested that under the same conditions also trilayers (3 ML) are present.[39, 40] The apparent height of 2 ML ZnO is 3.8 Å and of the 3 ML ZnO 5.8 Å.[40] Kumagai et al. observed rare 4 ML ZnO under the same conditions with an apparent height of 8.2 Å.[12] They did not grow layers with more than 4 ML or cover the Ag(111) surface completely which they ascribed to an annealing temperature close to the desorption temperature of the ZnO layers.[40] For 2 ML to 3 ML and 4 ML, a transition of the flat ZnO(0001) layers from the hexagonal boron-nitride structure (h-BN) to the wurtzite structure was observed by Tusche et al.[41] This transition creates a surface dipole.[83]

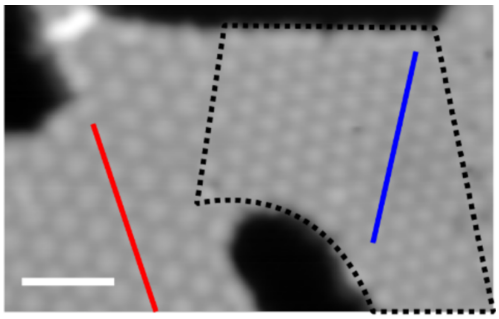

Figure 2.13: STM image of 2 ML ZnO on Ag(111) ($V_{\text{bias}} = 1$ V, $I = 0.05$ nA). The scale bar is 5 nm. The red line indicates the high-symmetry direction of the Ag(111) surface. The black dashed lines frame the misaligned Moiré pattern with the direction indicated by the blue line. Figure taken from reference [40].

Shiotari et al. reported the formation of a moiré pattern for ultra-thin layers.[41, 40] The moiré pattern is caused by a mismatch in the lattice of the ultra-thin ZnO layer and the Ag(111) surface.[40] Shiotari et al. found two distinct moiré pattern on the 2 ML ZnO as indicated in Fig. 2.13 where the misaligned moiré pattern is framed by black dashed lines.[40] The red line in Fig. 2.13 coincides with the high-symmetry direction of the Ag(111) surface which means the moiré pattern shows the same high-symmetry direction.[40] It shows a periodicity of about 23 Å which can be explained by a ZnO(0001)-(7x7)/Ag(111)-(8x8) coincidence structure (as depicted in Fig. 2.14 (A)).[40, 12] As indicated by the blue line in Fig. 2.14, the misaligned moiré pattern is rotated 30° with respect to the high-symmetry direction of the Ag(111) surface.[40] It exhibits a periodicity of about 16 Å which might

correspond to a ZnO(0001)-(5x5)/Ag(111)-($3\sqrt{3}$x$3\sqrt{3}$) R30° structure (as shown in Fig. 2.14 (B)).[40, 12] The misaligned moiré pattern is less stable explained by a strongly contracted lattice of the ZnO layer ($a_{\mathrm{ZnO,layer}} = 3.00\,\text{Å}$) compared to the bulk lattice constant ($a_{\mathrm{ZnO,bulk}} = 3.25\,\text{Å}$).[40] The lattice constant of the more stable moiré pattern which forms larger domains is $a_{\mathrm{ZnO,layer}} = 3.30\,\text{Å}$.[40] By comparison of STM and nc-AFM measurements, Shiotari et al. found that the moiré pattern results from a corrugation in the local DOS due to the lattice mismatch.[40, 84] The ZnO layers form an atomically flat, non-rippled structure on the Ag(111) surface.[40, 85]

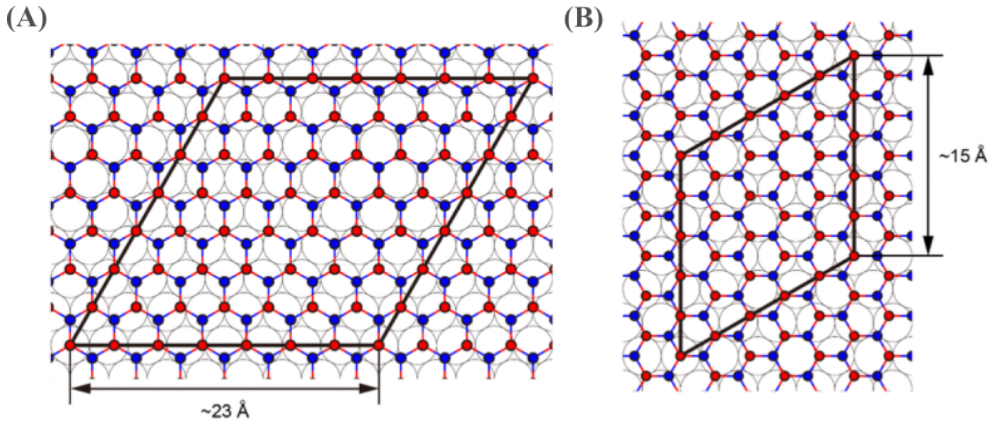

Figure 2.14: The unit cells of the moiré pattern: ZnO(0001)-(7x7)/Ag(111)-(8x8) coincidence structure (A) and ZnO(0001)-(5x5)/Ag(111)-($3\sqrt{3}$x$3\sqrt{3}$) R30° coincidence structure (B). Zn, O and Ag atoms are indicated as blue and red dots and gray circles, respectively. Figure taken from reference [40].

2.3.2 Electronic Structure

Kumagai et al. probed the local electronic structure of 2 ML, 3 ML and 4 ML ZnO on Ag(111) by means of STS.[12] The conduction band edges (CBE) are observed at 1.9 V, 1.6 V and 1.5 V for 2 ML, 3 ML and 4 ML, respectively.[12] Thus, with increasing thickness, the onset of conduction band (CB) is shifted to smaller energies.[12] As reported by Liu et al., the surface state of the bare Ag(111) surface is shifted to −0.2 V for the ZnO/Ag(111) and becomes an interface state (IS).[42, 86] They measured onset voltages of the CB at 1.8 V and 1.4 V for 2 ML and 3 ML ZnO on Ag(111).[42] Hence, they assigned the energies 2.0 eV and 1.6 eV to the transition between the IS and the CBE around the Γ-point for 2 ML and 3 ML ZnO.[42] By means of FER spectroscopy, Kumagai et al. reported that besides the FER states on the various ZnO layers, an interface state of the ZnO/Ag(111) interfaces is found at 4.5 V.[12] Respectively, for 2 ML, 3 ML and 4 ML ZnO, they estimated

the local work functions to be 4.0 eV, 2.8 eV and 2.8 eV applying an one-dimensional model for the FER states.[12] This large decrease from 2 ML to 3 ML ZnO and the same work function for 3 ML and 4 ML supports the observation of a structural transition between 2 ML and 3 ML.[12, 87] Shiotari et al. and Kumagai et al. showed that it is possible to differentiate the various ZnO layers by mapping the differential conductance (at constant current) for the CBE.[40, 12] The valence band maximum is not resolved by STS measurements as reported by Kumagai et al. because of masking by the Ag d-band whose onset is at around −4 V.[12] However, it is expected at approximately −4 V.[12] The electronic structure of 2 ML and 3 ML ZnO on Ag(111) is schematically summarized in Fig. 2.15.

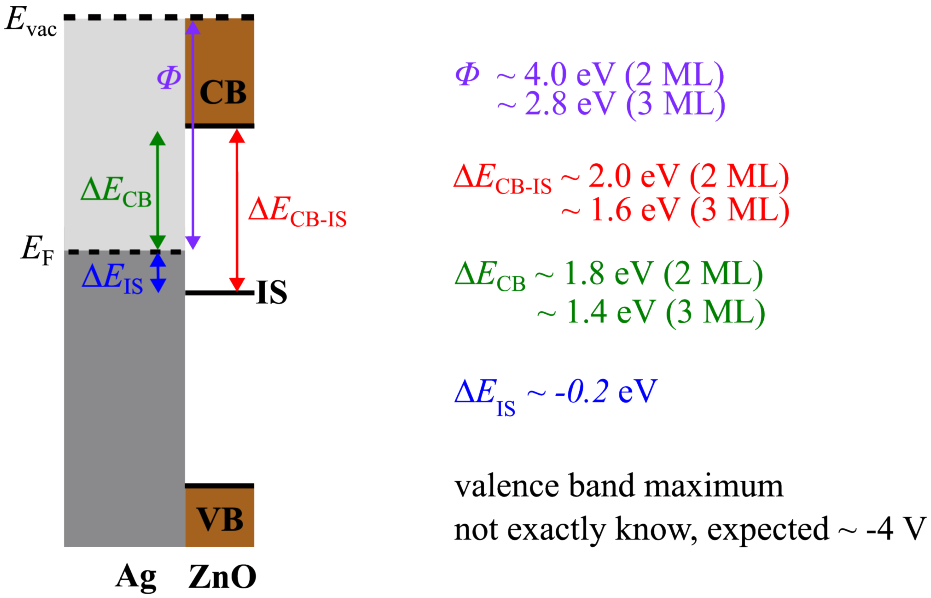

Figure 2.15: Schematic energy diagram of 2 ML and 3 ML ZnO on Ag(111) with the interface state (IS), the conduction band (CB) and valence band (VB). Besides the energies of the CBE and IS with respect to the Fermi level, the IS-CBE transition energy and the local work function Φ on 2 and 3 ML ZnO are given.

The integral intensity in a line scan of TERRS (Tip-Enhanced Resonance Raman Spectroscopy) spectra (see Fig. 2.16 (A)) drops significantly by moving from 2 ML ZnO (red) to 3 ML ZnO (blue) with the excitation wavelength (633 nm) corresponding only to the IS-CBE transition energy of 2 ML ZnO.[42] On 3 ML ZnO a TERRS signal was only obtained with an excitation wavelength of 780 nm matching the IS-CBE transition energy of 3 ML ZnO.[42] Hence, Liu et al. showed that the transition from the IS to CBE of 2 ML and 3 ML ZnO on Ag(111) plays an important role in TERRS as chemical enhancement (resonance Raman scattering) is necessary to strongly enhance the signal.[42]

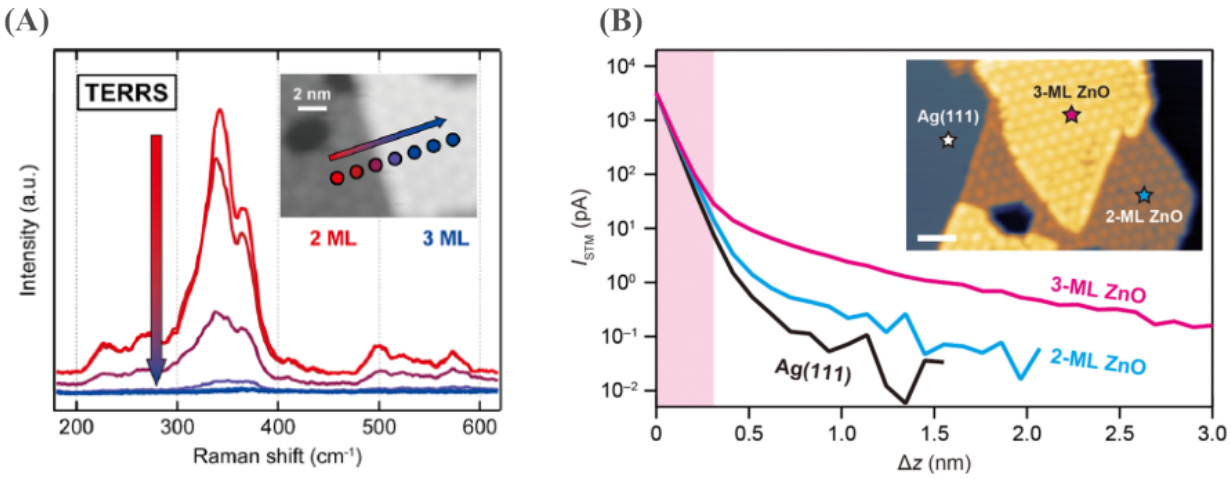

Figure 2.16: (A) Line scan of TERRS spectra with an excitation wavelength of 633 nm from 2 ML (red) to 3 ML ZnO (blue). The corresponding STM image and positions of the TERRS spectra (colour-coded) are given in the inset. Figure taken from reference [42]. (B) I-Δz curves on Ag(111), 2 ML and 3 ML ZnO with the positions marked in the STM image (inset) and $\Delta z = 0$ being the gap distance given by $V_{\text{bias}} = -2\,\text{V}$ and $I_{\text{t}} = 3\,\text{nA}$. The junction is illuminated by a 780 nm fs-laser. The photo-current is evident outside the conventional STM regime (pink area). Figure taken from reference [44].

TERS measurements on 2 ML ZnO showed that the optical transition of IS-CB (by a 633 nm cw-laser) plays also a significant role in the local heating of the film when the bias voltage is below the CBE.[44] When the bias voltage is above the CBE, the local heating originates from inelastic tunneling electrons (electron-phonon coupling) from the tip into the CB of ZnO.[44]

In a more recent publication of Liu et al., they were able to measure much larger photo-currents on 3 ML ZnO compared to 2 ML ZnO with a 780 nm fs-laser (see Fig. 2.16 (B)) which is in resonance with the IS-CBE transition of 3 ML ZnO.[43] This electronic resonance in the 3 ML ZnO film was used to locally probe optical coherent photons which are excited via the displacive excitation mechanism driven by the LSP of the STM junction with a spatial resolution of about 2 nm.[43] The idea behind this nanoscale coherent phonon spectroscopy is that the coherent phonons modulate the electronic structure of the 3 ML ZnO film and thus the probability of the IS-CBE transition which has an influence on the measured photo-current.[43] It seems, the IS-CBE transition in ultra-thin ZnO films on Ag(111) promotes some interesting behaviour and the mentioned studies on TER(R)S and nonscale coherent phonon spectroscopy indicate a strong coupling between the LSP of the junction and the IS-CBE transition.

3 Experimental Setup

The first section 3.1 of the experimental setup gives an insight into the low-temperature scanning tunneling microscope and its optical setup. The following section 3.2 describes the cleaning of the Ag(111) and Au(111) surface and the preparation of the ultra-thin ZnO films on Ag(111) as well as the ZnO preparation chamber. Following this, section 3.3 shows how the ultra-thin ZnO films are characterised via STM and STS. The subsequent section 3.4 describes the in-situ preparation of plasmonic Ag and Au tips and its characterisation via STML and plasmon-assisted resonant electron tunneling. The last section 3.5 covers the normalization procedure of the STML spectra.

3.1 Low-Temperature Scanning Tunneling Microscope

The measurements have been conducted with a LT-STM system (modified USM-1400, UNISOKU) which is depicted in Fig. 3.1. The LT-STM system consists of a preparation chamber, measurement chamber and a cryostat. Inside the preparation and measurement chamber UHV conditions with a base pressure of around 10^{-10} mbar are maintained by two ions pumps connected under both chambers. Preparation and measurement chamber are separated by a gate valve in order to prevent contamination. Sample and tip transfer inside the system is done with transfer rods and they can be stored in the measurement chamber. For the transfer in and out of the UHV system, a load-lock is connected to the preparation chamber via a gate valve. The load-lock prevents breaking the UHV and it is pumped by a turbo and membrane pump. After venting the load-lock, the base pressure of around 3×10^{-10} mbar inside the load-lock was reobtained by baking out over night. Additionally, a separated chamber is attached to the preparation chamber in order to prepare ZnO films (see section 3.2).
The cleaning of the sample and tip is done inside the preparation chamber. Annealing and sputtering are done on the manipulator stage. The sputter gun with an inlet for Ar gas is attached to the preparation chamber. There are two heating modes available for annealing: direct current and electron emission. During annealing, the temperature of the sample is measured via a pyrometer (PYROSPOT DG 56N, from DIAS) which is outside the system.

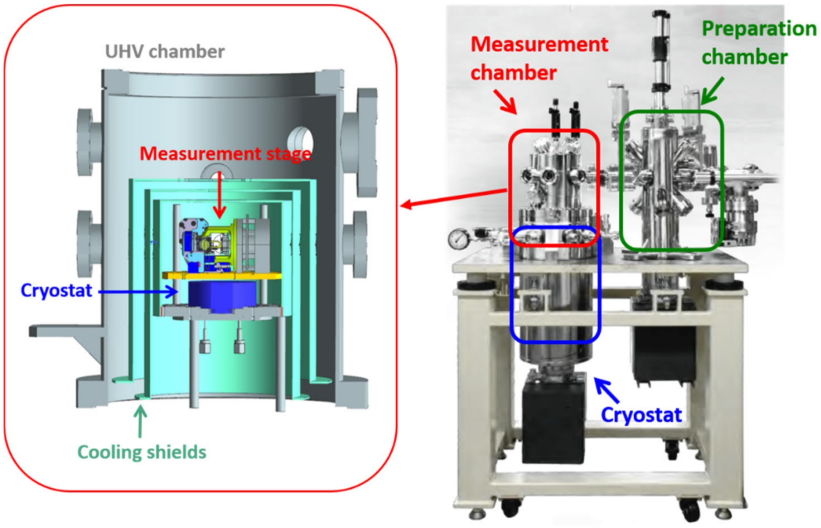

Figure 3.1: USM-1400 UNISOKU LT-STM system with preparation chamber, measurement chamber and cryostat (right). In order to maintain UHV conditions, ion pumps are connected to the preparation and measurement chamber (black boxes). The left figure exhibits a cross section of the measurement chamber with the measurement stage, cryostat and cooling shields. Figure taken from reference [88].

The location of the measurement stage is shown in the left of Fig. 3.1. It is located above a small reservoir of the cryostat in which the cryogenic liquid is pumped up. The cryostat can be filled with liquid nitrogen (or liquid helium) and keeps the temperature of the stage at around 78 K (or 5 K) for about 5 days. In this thesis, all the measurements were conducted at liquid nitrogen temperature. Furthermore, three cooling shields protect the stage. For good thermal conductance on the stage, copper wires are added.
The STM stage is operated with a Nanonis SPM controller. Fig. 3.2 shows the top view of the STM stage. The tip and tip holder (5) are fixed in the given setup while the sample (2) is moving with the coarse motions for approaching and a scan piezo tube (1). The tip is mounted by a clamping mechanism on the tip holder which comprises a hole such that the collimated beam pass through it. This collimated beam is focused on the junction by a Ag-coated parabolic mirror (4) with a numerical aperture of around 0.6 and a focus length of 8.5 mm (indicated as red dashed line in Fig. 3.2). This is required for in- and out-coupling of light into or out of the STM junction. The parabolic mirror is positioned via a piezo motor (3) with two rotational and three linear motions. For collecting the reflection beam, there is an additional lens (6) which is also positioned by a piezo motor (7). Suspension

springs (8) decouple the stage from the chamber vibrationally.

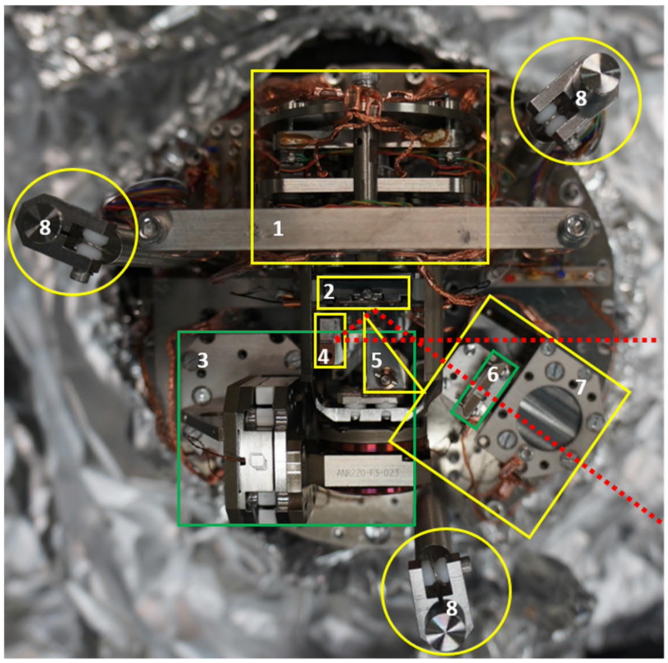

Figure 3.2: Labeled image of the STM stage. The beam path for focusing or collecting light is represented by the red dashed line. 1: piezo motor for scanning, 2: sample, 3: piezo motor for parabolic mirror (4), 5: tip holder, 6: lens, 7: lens motor, 8: three suspensions springs. Figure taken from reference [88].

Fig. 3.3 shows the optical setup schematically which enables in- and out-coupling of light into and out of the STM junction. The optical beam path inside the UHV chamber (with sample, tip and parabolic mirror) was already seen in the photo (Fig. 3.2). In order to have optical access, the UHV chamber possesses fused silica windows. For optical measurements, the beam has to be aligned parallel to the axis of the parabolic mirror. This alignment is done with a cw-laser (532 nm) being reflected on the plane area of the parabolic mirror. There are two more cw-laser available with a wavelength of 633 nm and 780 nm. For tilt correction, the beam and the reflected beam have to coincide. The translation of the beam is achieved by a stage outside the chamber. The outgoing light of the STM junction is guided through a beam splitter either to an optical fiber and the spectrometer or a CCD camera. STML measurements were conducted with the spectrometer (HRS-300-MS and PyLoN 400 BR eXcelon camera, from Teledyne Princeton Instruments) outside the chamber. The CCD chip of mentioned spectrometer was destroyed by icing such that a new grating (800 nm and 180 l/mm) had to be installed to a different spectrometer (SR-303i-B and Newton DU970N-BV camera, from Andor). The Andor spectrometer had merely gratings which resolved

smaller spectral ranges with higher resolutions for TERS measurements. Unfortunately, no STML measurements were performed with the new grating due to other experimental difficulties. By observing the scattered light from the cw-laser upon illumination of the tip via the CCD camera outside the chamber, the parabolic mirror was further aligned. High photon count rates in STML spectra on the bare Ag surface and the shift of the FER peaks in STS spectra measured at constant current caused by resonant electron tunneling appear only if the parabolic mirror is well aligned.[31, 88]

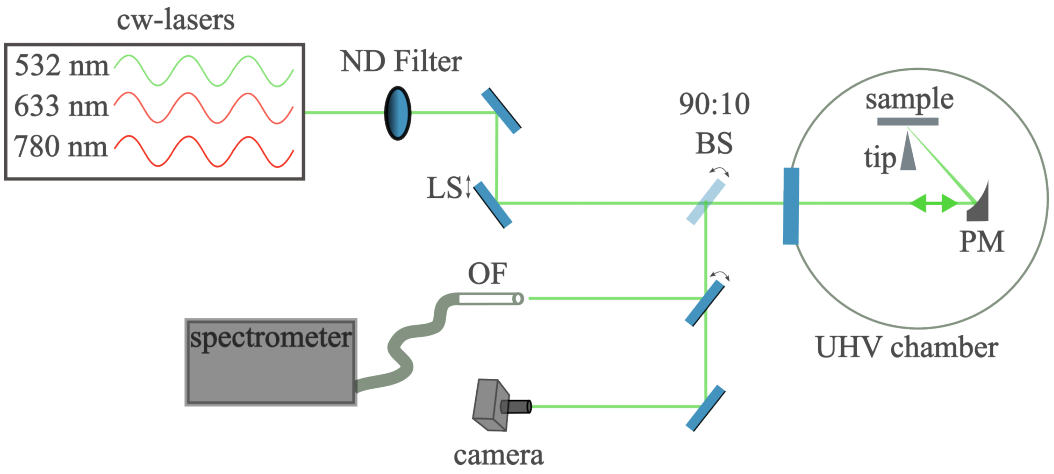

Figure 3.3: Schematic drawing of the optical setup for in- and out-coupling of light into and out of the STM junction. Three cw-lasers are available (532 nm, 633 nm and 780 nm). The light emitted from the STM junction can be either captured by a CCD camera or a spectrometer outside the UHV chamber. ND Filter: neutral density filter, LS: linear stage, BS: beam splitter, PM: parabolic mirror, OF: optical fiber.

3.2 Cleaning of Ag(111) and Au(111) Surface and Preparation of Ultra-thin ZnO Films on Ag(111)

A Au(111) sample after being stored two years under ambient conditions was degassed over night at about 670 K. Both sample surfaces (Ag(111) and Au(111)) were cleaned by multiple cycles (usually two or three cycles) of Ar ion sputtering and annealing. A sputtering time of 20 min per cycle at an Ar pressure of approx. 5×10^{-6} mbar ($E = 1$ keV to 1.5 keV) was chosen. Afterwards both samples were annealed to 770 K for 3 min with electron emission and a pyrometer outside the UHV chamber measuring the temperature. The purity of the samples was checked by taking STM images and STS spectra.

Ultra-thin ZnO layers were grown on the Ag(111) surface with the reactive deposition

method.[39] As depicted in Fig. 3.4, the preparation was done in a separated chamber with a base pressure below 5×10^{-10} mbar. Multiple Zn rods (99.9997 %, Alfa Aesar) are the Zn source in a Knudsen cell and a thermocouple is attached to the bottom of the Knudsen cell in order to monitor the deposition rate. The Zn rods are heated by direct current. The orifice of the Knudsen cell is pointing towards the Ag(111) sample surface (with a distance of around 15 cm) which is placed in position by a transfer rod. Between Knudsen cell and sample is a movable shutter with a quartz crystal microbalance attached and a mask to avoid ZnO deposition on the sample holder. The quartz crystal microbalance is unfortunately not properly working and has to be replaced in the near future. Oxygen is dosed via a needle valve and the pressure is monitored with a cold cathode gauge inside the ZnO preparation chamber.

Following preparation procedure of ultra-thin ZnO films on Ag(111) yields 2 ML islands and rather small 3 ML islands. The deposition of Zn upon the Ag(111) surface was conducted at room temperature for one hour and with an O_2 background pressure of 1×10^{-5} mbar. The rod is annealed to 470 K. After deposition the sample is transferred to the preparation stage in the preparation chamber and post-annealed multiple times (two or three cycles) to approx. 700 K for 3 min in UHV. The sample was cooled down slowly (10 K/min) until 620 K. By applying STM and STS the ultra-thin ZnO films were characterized (see section 3.3).[12]

However, the mentioned sample preparation was hardly reproducible because either the overall coverage was too low or the ZnO islands showed no defined structure. Thus, different parameters during sample preparation such as the deposition time (up to three hours), the Zn rod temperature (up to 490 K) and the O_2 background pressure (up to 5×10^{-5} mbar) have been tried. Additionally, the post-annealing temperature (from 620 K to 720 K) and duration (2 min to 30 min) have been varied. Merely a larger deposition duration showed positive results but only with 2 ML ZnO islands. There are several possible explanations for these experimental difficulties. The first possible error source is the ZnO rods inside the Knudsen cell and a change of their condition. This assumption is supported by the large deposition duration. It was observed that at least one of the Zn rods detached from the crucible inside the Knudsen cell and hence lost electric contact. This was most probably caused by mechanical force on the transfer rod of the ZnO preparation chamber. Other factors which might alter the condition of the Zn rods are oxidation of Zn on its surface or melting of the Zn rods due to higher local temperatures. Independent on the cause, it is recommended to open the chamber and exchange the Zn rods for future sample preparations. By doing so, the quartz crystal microbalance is to be replaced and the mask to shield

the sample holder re-aligned in order to obtain a qualitative reference for good deposition conditions and to ensure maximum Zn deposition on the Ag(111) surface, respectively. Additionally, it is recommended to exchange one blind flange with a fused silica window in order to have better visual confirmation and to simplify the height estimation of the sample surface with respect to the mask and the Zn rods. Another cause for difficulties regarding the preparation might originate from the single crystal itself via alloying between Zn and Ag. A high background O_2 pressure was chosen in order to prevent it as Zn and Ag readily form surface alloys.[39] It is recommended for further studies to clean the Ag(111) surface additionally by annealing in O_2 atmosphere as done by Pan et al.[39] The last critical parameter is the post-annealing process. As reported by Shiotari et al., there is only a small temperature range above 600 K where the islands become well-ordered before the desorption rate increases rapidly such that ZnO films decompose/desorb and the overall coverage decreases.[40, 12] In our setup the temperature for well-defined ZnO films corresponds to temperatures above 670 K.[12] According to a calibration measurement with a thermocouple in a different UHV system, this difference originates from the pyrometer. The post-annealing procedure is hardly reproducible because the temperature is controlled manually and the temperature displayed on the pyrometer depends on the alignment.

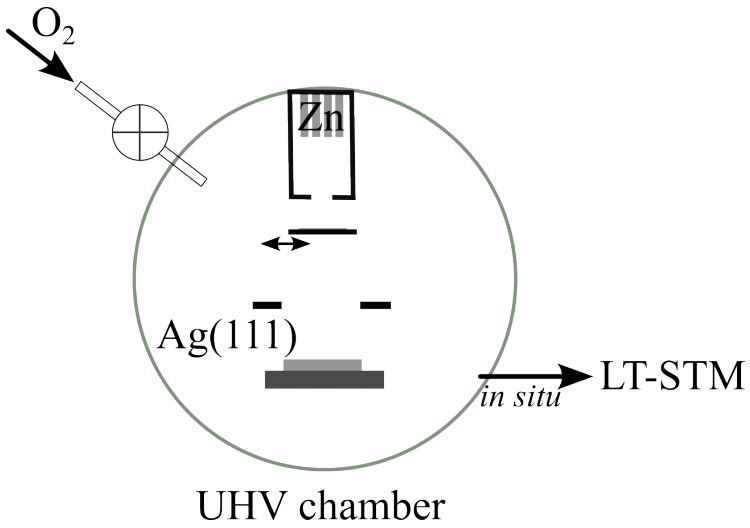

Figure 3.4: Scheme showing the separated UHV chamber for preparation of ultra-thin ZnO films with the reactive deposition method. The Zn rods are inside a Knudsen cell which can be heated. O_2 background pressure can be adjusted accordingly via a needle valve. The shutter to which a quartz crystal microbalance is attached prevents Zn deposition on the Ag(111) surface during the heating up of the Zn rods. The mask protects the sample holder from Zn deposition.

3.3 Characterisation of the Ultra-thin ZnO Films by STM and STS

According to the preparation procedure of ultra-thin ZnO films described in section 3.2, 2 ML and 3 ML ZnO islands have been observed on the Ag(111) surface. They are distinguishable by several criteria. The moiré pattern of 2 ML (see Fig. 3.5 (A)) is more uniform and distinctive than of 3 ML (see Fig. 3.5 (B)). In most of the cases, the moiré pattern of the 3 ML is not even observable. Commonly, 2 ML forms larger ZnO islands than 3 ML. Fig. 3.5 (C) exhibits the height profiles of the depicted 2 (red line) and 3 ML (blue line) ZnO islands. In accordance with Shiotari et al., the apparent height of the 2 ML and 3 ML ZnO island is about 4 Å and 6 Å, respectively.[40] It is important to measure the apparent height with a bias voltage below the CBE as the apparent height depends on the bias voltage.[40] The height profiles indicate a periodicity of the moiré pattern of about 17 Å for 3 ML and about 19 Å for 2 ML. A periodicity of about 23 Å would give evidence to a ZnO(0001)-(7x7)/Ag(111)-(8x8) coincidence structure and a periodicity of about 15 Å to a ZnO(0001)-(5x5)/Ag(111)-($3\sqrt{3}$x$3\sqrt{3}$) R30° coincidence structure.[40, 39, 41]

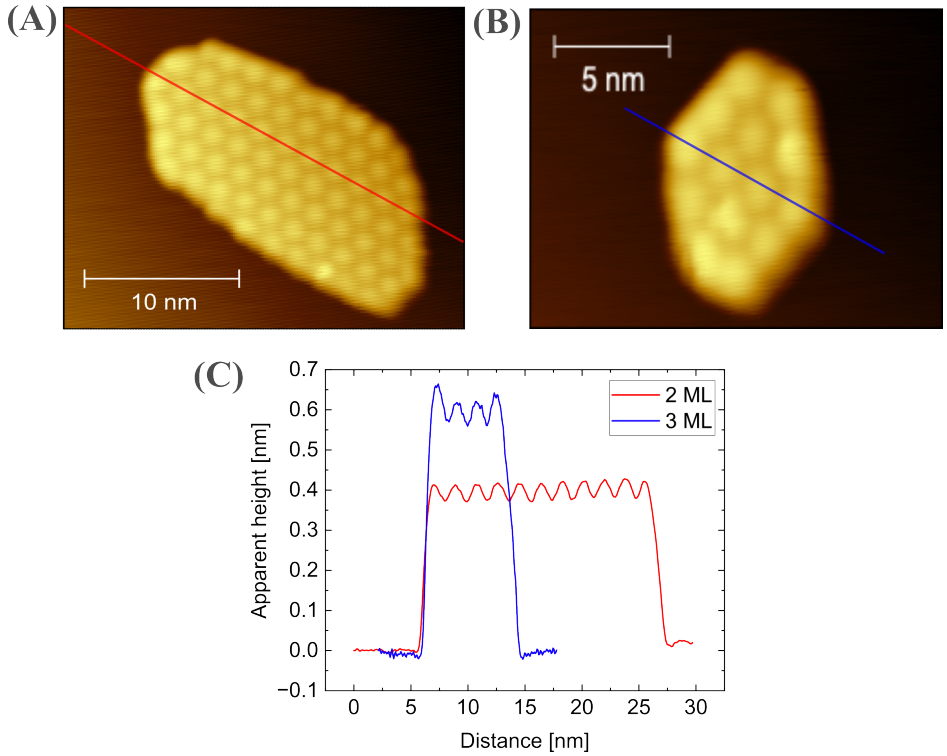

Figure 3.5: STM images of a 2 ML ZnO island (A) and a 3 ML ZnO island (B) ($V_{\text{bias}} = 1\,\text{V}$, $I_{\text{t}} = 100\,\text{pA}$). (C) Height profiles according to the blue (2 ML) and red (3 ML) lines shown in the STM images.

Another convenient way to distinguish 2 and 3 ML ZnO islands is by their CBE. Fig. 3.6 depicts the dI/dV (STS) spectra on 2 (red) and 3 ML (blue) ZnO in constant current mode such that the tip is retracted with increasing bias. Fig. 3.6 also shows the tip retraction in dashed lines. The tip retracts by 3 Å on 2 ML and by 2 Å on 3 ML ZnO. Thus, we observe the CBE as a peak in constant current measurements. In accordance to the literature, the CBE for 2 ML ZnO is observed at 1.9 V and for 3 ML ZnO at 1.45 V.[12, 42, 40]

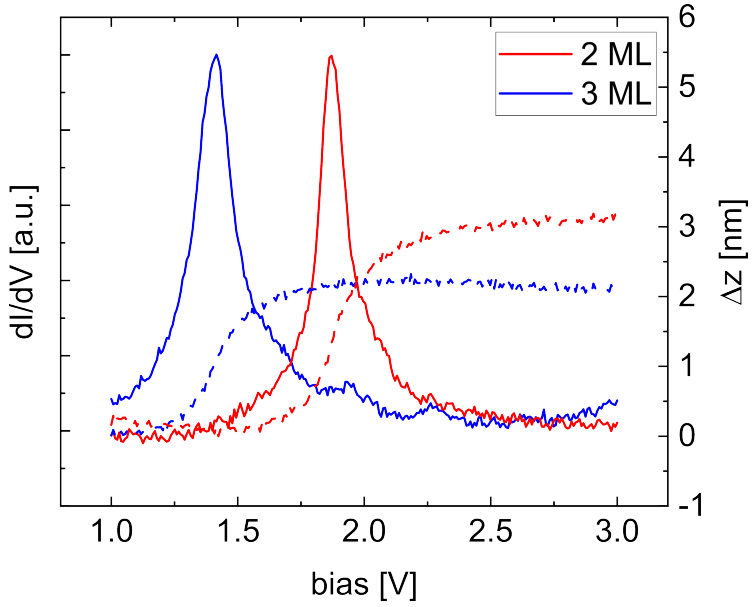

Figure 3.6: STS (dI/dV) spectra (solid lines) in constant current mode ($I_t = 100\,\text{pA}$) on 2 ML (blue) and 3 ML (red) ZnO islands on the left axis. The tip retractions are shown by the dashed lines on the right axis (Δz).

STS (dI/dV) maps can be used to spatially resolve the CBE and distinguish 2 and 3 ML ZnO islands. According to the maxima in the STS spectra (see Fig. 3.6), the STS maps in Fig. 3.7 have been taken at 1.85 V for 2 ML ZnO (A) and at 1.45 V for 3 ML ZnO (B). Fig. 3.7 shows the STS maps of the ZnO islands whose STM images are depicted in 3.5. As expected from the STM images, the moiré pattern is more uniform for 2 ML ZnO. The protrusions of the moiré pattern of 2 ML in the STM images (Fig. 3.5 (A)) are visible as depressions in the STS map (Fig. 3.7 (A)).[40] The weak intensities at the edges of the 2 ML and 3 ML ZnO islands are explained by local electronic states modifications.[40, 89, 90]

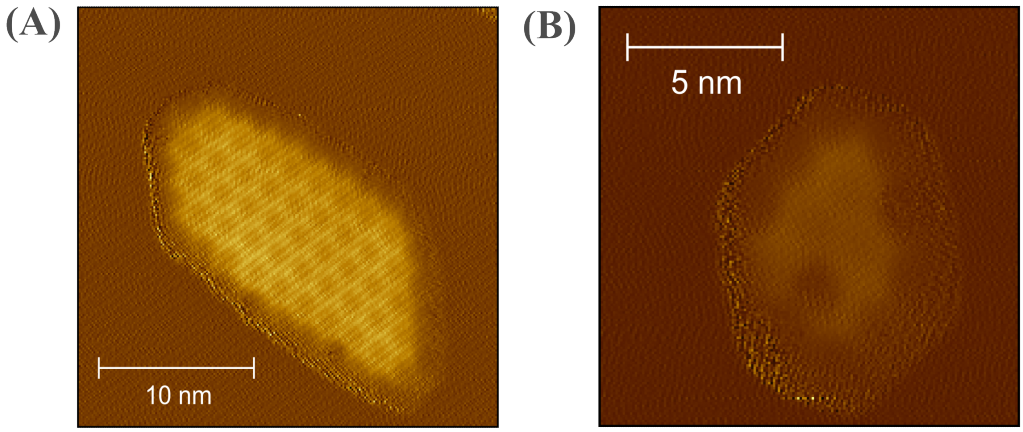

Figure 3.7: STS (dI/dV) maps of 2 ML ZnO with $V_{\text{bias}} = 1.85\,\text{V}$ (A) and 3 ML ZnO with $V_{\text{bias}} = 1.45\,\text{V}$ (B) ($I_{\text{t}} = 100\,\text{pA}$). The corresponding STM images of the 2 and 3 ML ZnO islands are depicted in Fig. 3.5.

3.4 In-situ Preparation and Characterisation of Plasmonic Tips

The FIB fabricated Ag tip was provided and exhibited a strong plasmonic response. In order to improve STM imaging of the Ag tip after slight indentation into the sample surface or picking up impurities, short bias voltage pulses of +/- 3 V and slight indentation of the tip apex ($\Delta z \approx 1\,\text{nm}$) on/into the bare Ag(111) surface were applied. Sometimes this also lead to minor changes of the plasmonic response. For more drastic changes of the tip apex and the plasmonic response of the Ag tip, the tip was sputtered for 20 min at an energy of 1 keV and Ar pressure of 5×10^{-6} mbar.

It was attempted to prepare good apices of two FIB fabricated Au tips which were in stock for years (inside a desiccator). Several approaches have been tried to obtain Au tips with good imaging abilities and a more red-shifted plasmonic response with respect to the Ag tips. Initially after a first Ar sputtering cycle (20 min, 1 keV, 5×10^{-6} mbar), the Au tip-Ag(111) junctions were very unstable with difficulties getting into the tunneling regime. Further Ar sputtering, slight indentation into the Au(111) surface and pulsing up to +/- 10 V did not change the condition of the tip apex. Laser annealing with the 532 nm cw-laser at full laser power ($\approx 5.6\,\text{mW}$) focused on the tip apex did not improve its condition. The most drastic preparation procedure which creates a complete new tip apex on a larger scale (in the order of 100 nm) is explained in the following. First, the feedback loop is turned off in

tunneling regime and the tip indented into the clean Au(111) surface manually by 10 nm such that the current is saturated. The bias voltage is set to 10 V and the tip is retracted very slowly manually. It takes about 20 min until the current drops to zero. The freshly prepared tip apex showed a promising STM imaging ability and plasmonic response judging from the CCD camera showing the junction. However, as the current and bias voltage was increased to measure STML spectra of the plasmonic response, the junction seemed very unstable. Due to time constraints it was not possible to further prepare a suitable Au tip with a red-shifted plasmon and measure a corresponding STML spectra.

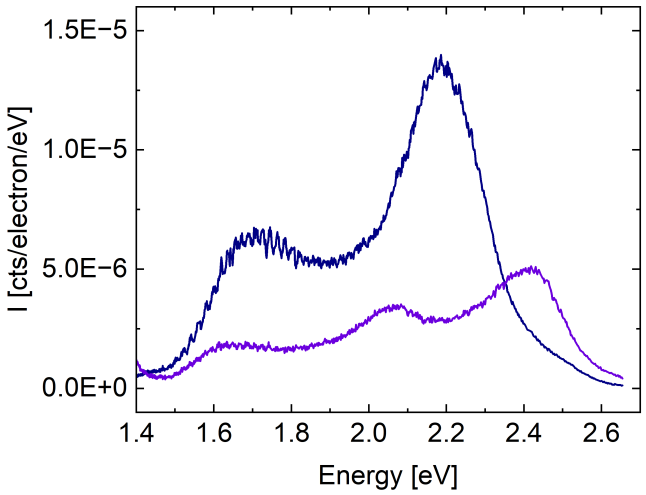

Figure 3.8: Two different plasmonic responses of the same Ag tip with FIB structure but different tip geometries on the bare Ag(111) surface ($V_{\mathrm{bias}} = 3\,\mathrm{V}$, $I_{\mathrm{t}} = 3\,\mathrm{nA}$). The difference illustrates a strong dependence on the tip geometry.

The quality of the plasmonic Ag tip can be judged by the STML spectra (see Fig. 3.8) or the plasmon-assisted resonant electron tunneling in the STM junction (STS spectra, see Fig. 3.9) as described by Liu et al.[31] Fig. 3.8 shows two STML spectra as counts per electron and eV versus the photon energy in eV from the STM junction consisting of a Ag tip and a Ag(111) surface. The light collection efficiency of the experimental setup is not included. The STML spectra exhibits a broad plasmonic response from about 1.4 eV to about 2.6 eV which is originating from the excitation of LSPs in the STM junction by inelastic electron tunneling and their radiative decay. It is important to note that the plasmonic response strongly depends on the tip geometry.[75, 59, 73] Small changes of the tip geometry due to the unmeant and intended indentation into the sample surface or pulsing caused different

plasmonic responses as shown in Fig. 3.8 with two STML spectra from the same tip. The oscillation at lower photon energies might be an indication of the interference of localized and propagating surface plasmon modes as reported for Fabry-Pérot tips by Böckmann et al.[73]

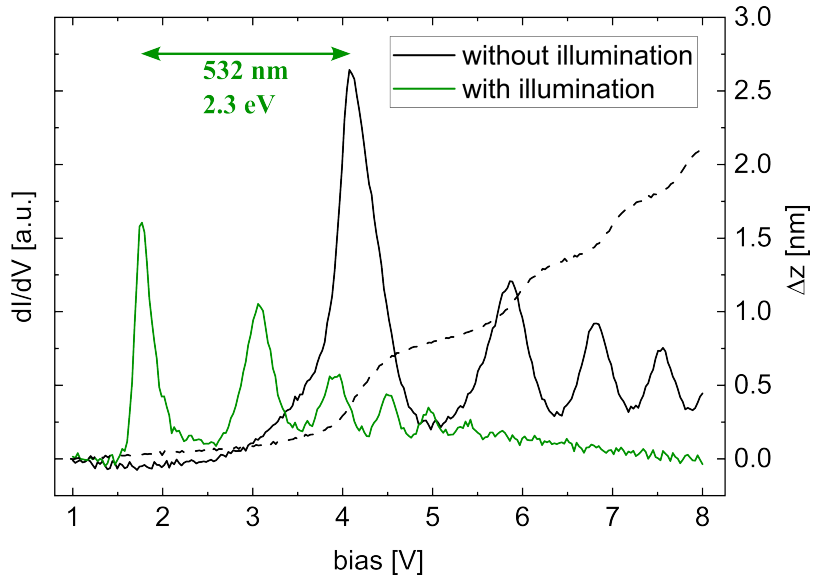

Figure 3.9: STS spectra in constant current mode (left axis, $I_t = 100\,\text{pA}$) of a STM junction consisting of a plasmonic Ag tip and a Ag(111) surface with (green solid line) and without (black solid line) illumination of a 532 nm cw laser at full power ($P \approx 5.6\,\text{mW}$). The tip retraction (without illumination) is shown as dashed black line (right axis).

Fig. 3.9 shows a STS spectra in the range of 1 V to 8 V in constant current mode ($I_t = 100\,\text{pA}$) of a plasmonic Ag tip-Ag(111) surface junction with (green curve) and without (black curve) illumination of a 532 nm cw-laser at full power ($P \approx 5.6\,\text{mW}$). This wavelength corresponds to a photon energy of 2.3 eV. The STS spectrum without illumination (black curve) shows the first four peaks of the FER series of a Ag tip-Ag(111) STM junction with the first FER peak around 4 eV which is in accordance to the literature.[59, 12, 31] The STS spectrum with illumination (green curve) exhibits the series of FER peaks up to the sixth peak whereby the subsequent peaks and their intensities are comparable to the noise level. As expected from the publication from Liu et al.[31], the multiple FER peaks are completely shifted according to the incident laser energy 2.3 eV due to the plasmon-assisted resonant electron tunneling (see subsection 2.1.3). The resonant and non-resonant tunneling compete with each other and a complete FER shift is only observed at higher laser power

densities.[31] In order to observe the FER shift with the 532 nm cw-laser, the alignment of the parabolic mirror has to be adequate and the plasmonic response of the STM junction has to exhibit intensity at the corresponding wavelength as shown by Liu et al.[31]

3.5 Normalization of STML spectra

The raw STML spectra obtained from the spectrometer are given as intensity in counts/nm (I [cts/nm]) versus the wavelength in nm. These raw spectra are first normalized to current and exposure (integration) time and thus to the number of electrons (I [cts/nm/electron]). An integration time of 3 s was chosen with an averaging over 10 spectra. For better evaluation, the STML spectra are smoothed and converted from wavelength to photon energy ($E = \frac{hc}{\lambda}$). In order to properly convert the spectra, the Jacobian conversion is applied[91]:

$$f(E) = f(\lambda)\frac{\mathrm{d}\lambda}{\mathrm{d}E} = -f(\lambda)\frac{hc}{E^2} \tag{3.1}$$

This minus sign is ignored in the conversion because it just reflects a different direction of integration in energy and wavelength[91]. After the Jacobian conversion, the STML spectra show the intensity as a function of the photon energy ($I(h\nu)$ [cts/eV/electron]).
The measured STML data exhibit a strong tip geometry dependence and the enhancement by the confined plasmonic field depends on the energy. The plasmonic response $I_{\mathrm{ref}}(h\nu)$ on the bare Ag(111) surface (taken at a bias voltage V_{ref}) measured before each data set contains spectral features arising from the tip geometry. However, the reference spectrum $I_{\mathrm{ref}}(h\nu)$ does not properly account for the energy-dependent enhancement due to the finite energy window.[92] Lower photon energies are overrepresented because with decreasing photon energies an increasing number of transitions are possible in the allowed bias window. In order to account for the possible number of transitions in a given energy window (between bias voltage and Fermi level), $I_{\mathrm{ref}}(h\nu)$ is corrected by an additional, dimensionless factor $(eV_{\mathrm{ref}} - h\nu)^{-1}$ inserting the values of eV_{ref} and $h\nu$ in units of eV.[30, 92] This yields the surface plasmon enhancement function $S_{\mathrm{PL}}(h\nu)$.[30, 92] In order to remove the tip-dependent features and the energy-dependent enhancement, the STML spectrum $I(h\nu)$ is normalized to the surface plasmon enhancement function $S_{\mathrm{PL}}(h\nu)$ which yields the dimensionless relative photon yield $Y(h\nu) = I(h\nu)/S_{\mathrm{PL}}(h\nu)$.[30]
For a pure plasmonic response of the junction, one expects $Y(h\nu)$ to decrease proportional to $(eV_{\mathrm{bias}} - h\nu)$ after the maximum.[92] According to Stróżecka et al., this normalization is only valid if the plasmonic field of the junction is strong enough in the inspected energy regime.[92] Thus, at low photon energies (below 1.4 eV) at which the photonic DOS of the

Ag tip-Ag(111) junction is low, this normalization is not reliable. Additionally, this photon energy regime is prone to artefacts from second order diffraction rendering the normalization useless at photon energies with overlap of the first and second order. Another drawback of this normalization is the dependence of the optical response of the junction on the gap distance between surface and tip.[93]

4 Results and Discussion

In the first section of the results and discussion part 4.1, bias-dependent STML measurements on the bare Ag(111) surface are discussed. The second section 4.2 covers STML measurements on ultra-thin ZnO films on Ag(111), which is subdivided in five parts. The first (4.2.1) and second (4.2.2) part present the results of the bias-dependent STML measurements at positive bias voltage and the spatial STML mapping, respectively. Subsequently, these results are discussed (4.2.3). The fourth part (4.2.4) discusses the results of the bias-dependent STML measurements at negative bias voltage, and current-dependent STML measurements are discussed in the last part (4.2.5).

4.1 STML on Ag(111)

To characterize the LSP of the tip and for normalization of the STML spectra on ZnO, first the bias dependence of the STML spectra on the bare Ag(111) surface has been measured at a constant current of 3 nA. Fig. 4.1 (A) shows the STML spectra (only normalized to electrons) on the bare Ag(111) surface plotted as contour plot. The STML response evolves to higher energies with increasing bias due to energy conservation. The quantum cutoff (eV_{bias}) is readily seen in the contour plot and marked with a red solid line. As the quantum cutoff is exceeding the spectral range of the spectrometer, the STML response is broad and covers the whole spectral range from about 1.4 eV to 2.6 eV. It exhibits a smaller maximum at around 1.65 eV and a larger maximum at around 2.35 eV with a plateau in-between (see line spectra in Fig. 7.1). The integrated intensity increases with increasing bias (see Fig. 4.1 (B)). Above a bias voltage of 2.5 V, the STML spectra starts to show intensity at photon energies of 1.25 eV which shifts to 1.45 eV photon energy with an increase of the bias voltage up to 3 V (light grey part in Fig. 4.1 (A)). The 1.25 eV peak (corresponds to about 1000 nm) is only observed in several STML spectra at 3 V on the bare Ag(111) surface when there is significant intensity at the 2.5 eV peak (corresponds to about 500 nm). Thus, this intensity increase below photon energies of 1.45 eV is an artefact explained by the second order diffraction of the grating in the spectrometer. Installing a longpass filter with a cut-on wavelength of around 500 nm (corresponds to 2.5 eV) would avoid a spectral overlap of first and second order. The observed intensity in the STML spectra

stems from the radiative decay of the LSP of the STM junction, which is excited by inelastic electron tunneling from Ag tip to Ag(111) surface as schematically depicted in Fig. 4.2.[59]

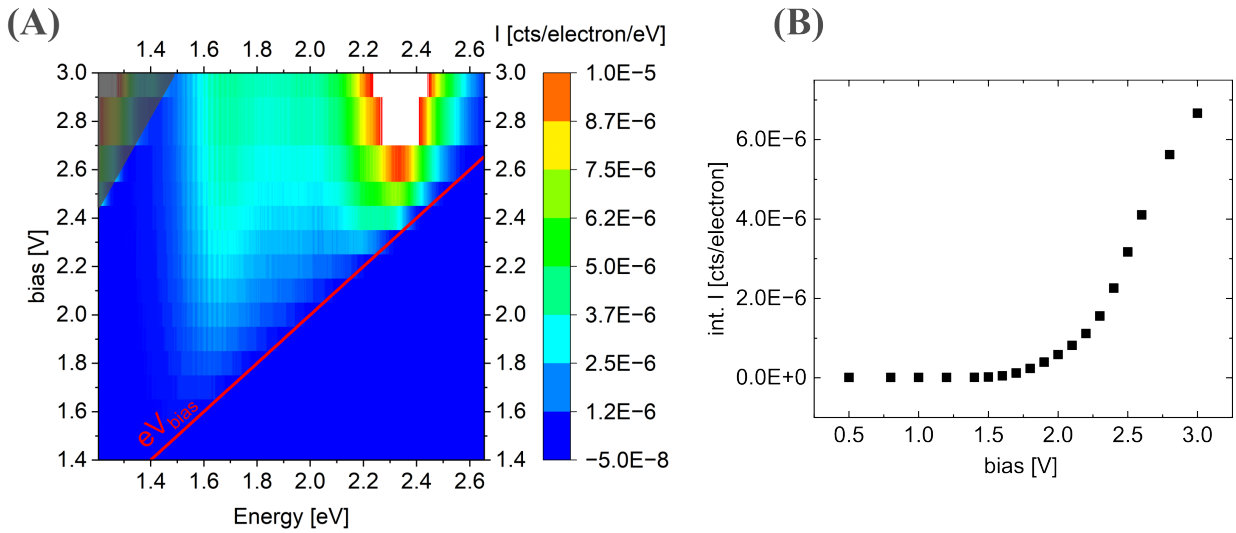

Figure 4.1: Contour plot (A) of the bias-dependent STML spectra (I [cts/electron/eV]) of the plasmonic response from a Ag(111)-Ag tip junction in constant current mode $I_t = 3\,\text{nA}$. The red solid line in the contour plot marks the quantum cutoff (eV_{bias}). The grey area at low photon energies (below 1.45 eV) is an artefact from second order diffraction. (B) shows the integrated intensity as a function of the bias voltage. The corresponding line spectra are shown in Fig. 7.1 (see Appendix).

With increasing bias voltage in constant current mode, the tip retracts from the surface, which means the gap distance increases. STS measurements at 100 pA on the bare Ag(111) surface showed a tip retraction of 0.9 Å from 1.4 V to 3 V (see Fig. 3.9). According to Martínez-Blanco et al., the tip retracts at a constant current of 200 nA from 2 V to 3 V by about 0.5 Å.[59] At larger gap distances (> about 0.5 nm), the plasmonic field strength is increasing with decreasing distance.[43, 94] At small gap distances of the Ag tip-Ag(111) junction (< around 0.5 nm)[43, 95], one expects a decrease in the plasmonic field strength with decreasing gap distance due to damping of the LSP.[43, 96] In-between both distance regimes the plasmonic field strength experiences a maximum.[94] The gap distance dependence on the plasmonic field strength influences the STML intensity, which can be estimated by a current-dependent STML measurement (as conducted on 2 and 3 ML ZnO in subsection 4.2.5). The largest plasmonic mode at 2.35 eV indicates a larger photonic DOS at higher energies and the number of possible transitions increases in the

given energy window with increasing bias voltage.[92] Both effects lead to an increase of the integrated intensity with increasing bias voltage.

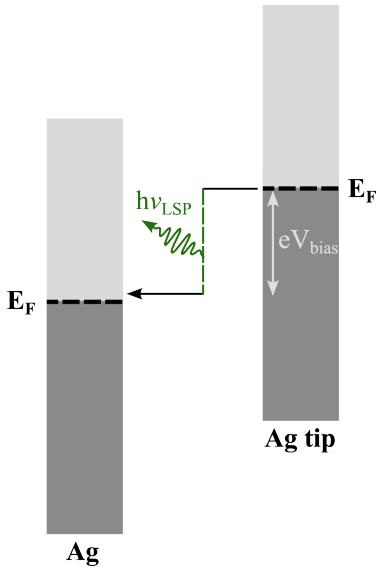

Figure 4.2: Schematic energy diagram of the Ag tip-Ag(111) surface junction. Inelastic electron tunneling excites the localized surface plasmon (LSP) of the junction which radiatively decays.

4.2 STML on Ultra-thin ZnO/Ag(111)

Fig. 4.3 shows STML spectra (only normalized to electrons) on 2 ML ZnO (A) and 3 ML ZnO (B). The STML spectra on 2 ML (red spectrum, $I_t = 8\,\text{nA}$, $V_{\text{bias}} = 3\,\text{V}$) and on 3 ML (blue spectrum, $I_t = 50\,\text{nA}$, $V_{\text{bias}} = 2.5\,\text{V}$) are scaled in order to better compare with the plasmonic response on the bare Ag(111) surface (grey spectra, $I_t = 50\,\text{nA}$, $V_{\text{bias}} = 2.5\,\text{V}$). The green dashed line and the red dashed line mark the energy of the CB with respect to the Fermi level and the IS-CB transition energy as expected from STS data, respectively. The STML spectrum on 2 ML (A) matches the plasmonic response on bare Ag(111) to a photon energy of 2 eV. Above photon energies of 2 eV the intensity on 2 ML ZnO is strongly suppressed in comparison to the plasmonic response on bare Ag(111). Similar on 3 ML ZnO (B), the STML spectrum matches only to a photon energy of about 1.55 eV. The STML intensity on 3 ML ZnO decreases above 1.6 eV. Hence, the relative STML intensity on 2 and 3 ML ZnO is reduced starting at photon energies around the respective CB energy and IS-CB transition energy.

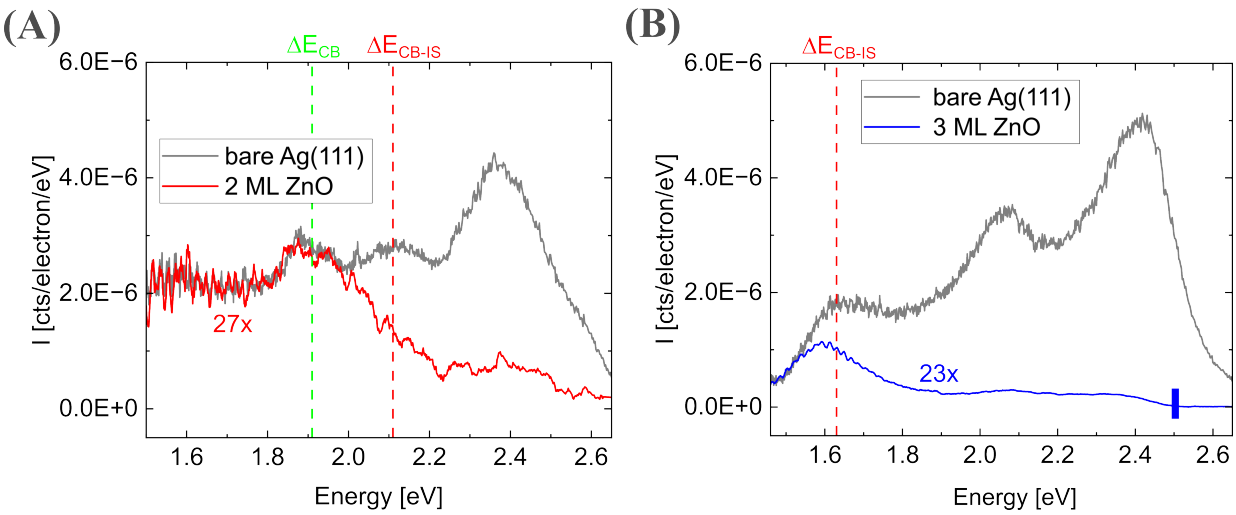

Figure 4.3: STML responses on 2 ML (A) and 3 ML (B) ZnO. The grey STML spectra represent the corresponding plasmonic responses on the bare Ag(111) surface ($I_t = 3\,\text{nA}$, $V_{bias} = 3\,\text{V}$). The green dashed line marks the CB energy with respect to the Fermi level and the red dashed line the IS-CB transition energy. (A): $I_t = 8\,\text{nA}$, $V_{bias} = 3\,\text{V}$, (B): $I_t = 50\,\text{nA}$, $V_{bias} = 2.5\,\text{V}$ (quantum cutoff marked by blue bar).

Energy Transfer versus Charge Injection

There are several possible processes which might be responsible for the observed spectral shape of the luminescence and which could explain the reduction of intensity at high photon energies with respect to the plasmonic response on the bare Ag(111) at positive bias voltage. Because the integrated intensity of the STML spectra increases linear with the current, only one-electron-photon processes are considered (see subsection 4.2.5). Since we do not observe sharp features in the STML spectra, we conclude that excitonic luminescence, e.g. due to defect states inside the ZnO[29], does not contribute to the luminescence of ultra-thin ZnO. Moreover, as we do not observe a well-defined valence band in STS[12] and because the films are not well decoupled from the Ag substrate, we do not expect to see intrinsic excitonic luminescence, e.g. from recombination of CB-electrons and VB-holes. Such luminescence would further be expected at higher photon energies $> 2\,\text{eV}$ ($1.6\,\text{eV}$). The STML response in Fig. 4.3 is broad which strongly indicates plasmonic luminescence from the radiative decay of the LSP of the junction which, however, is modified by the electronic structure of the ZnO films, in contrast to similar measurements on 2D-semiconductors where no such effect was observed.[30] At positive bias voltage, the plasmonic luminescence can be divided into two processes: plasmonic luminescence due to inelastic tunneling, which does not involve

the CB of ZnO (see Fig. 7.2 in Appendix), and plasmonic luminescence which is modified by the presence of the CB of ZnO (see Fig. 4.4). The former includes inelastic tunneling inside the band gap (at bias voltages below the CBE of ZnO) which excites the LSP of the junction (see Fig. 7.2 in Appendix). The latter originates either from energy transfer (Fig. 4.4 (A)) or from charge injection (Fig. 4.4 (B)) at bias voltages close to or higher than the CB energy/IS-CB transition energy.[97] Both mechanism have been observed on molecules[37, 98] while only charge injection was observed on 2D-semiconductors[21].

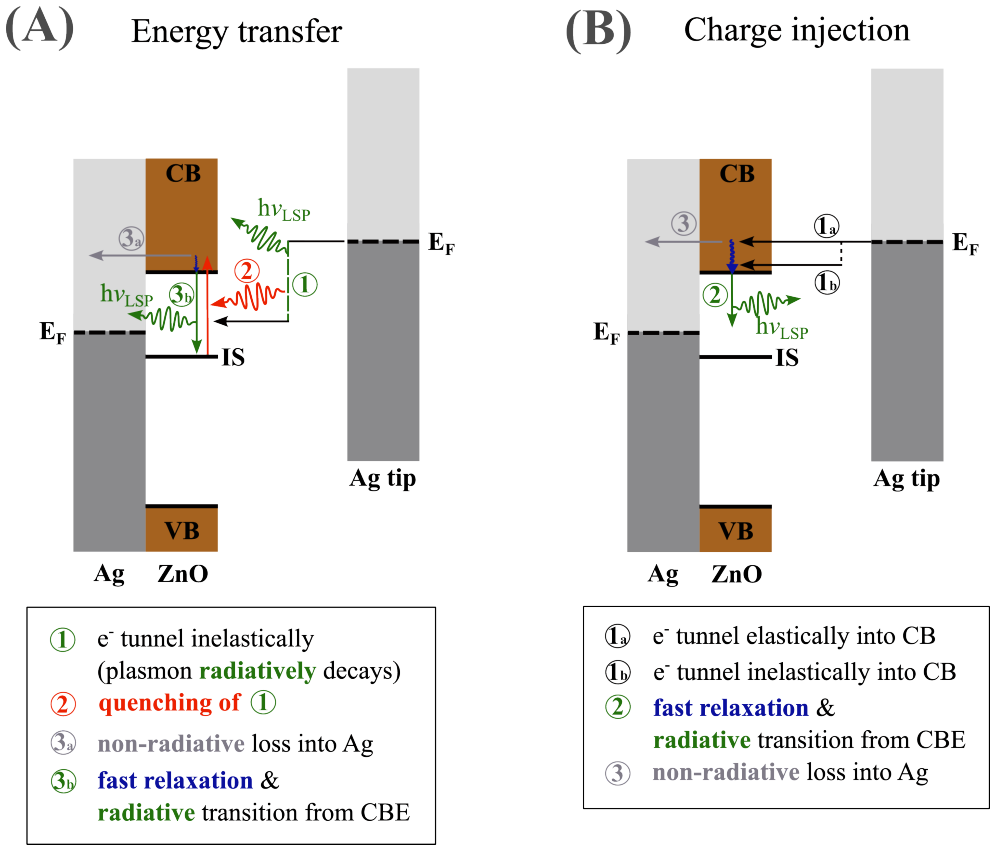

Figure 4.4: Schematic energy diagram of the ZnO/Ag(111)-Ag tip junction at positive bias voltages larger than the CB energy/IS-CB transition energy. It shows possible processes contributing to the STML response subdivided in (A) energy transfer and (B) charge injection.

In the energy transfer process (A), the electron first excites the LSP of the junction via inelastic tunneling (1). The LSP can then either radiatively decay (1, outcoupling into far-field) or excite the IS-CB transition (2). The excited electron in the CB is then either lost non-radiatively into the Ag bulk (3a) or undergoes fast relaxation due to electron-electron or electron-phonon coupling[44, 43] and radiatively decays at the CBE (3b). The final states

can either be holes at the Γ-point created by step 2 or unoccupied states of the Ag or the IS above the Fermi level away from the Γ-point[42, 99]. The first step of the charge injection mechanism (B) is tunneling of electrons elastically (1a) and inelastically (1b) into the CB of ZnO. After an electron is injected into the CB, either fast relaxation and a radiative transition with the initial state around the CBE (2) or non-radiative loss into the Ag bulk (3) occurs. In step 2, the final states are unoccupied states of the Ag or the IS above the Fermi level away from the Γ-point[42, 99]. At frequencies of the resonant modes of the LSP, the transition probability of radiative transitions at the CBE is strongly enhanced. That means, the radiative decay is weighted with the photonic DOS of the LSP. Thus, the observed luminescence is a convolution of the electronic and plasmonic structure because it depends on the initial and final states as well as on the photonic DOS.[93] In addition to the two processes (A) and (B), inelastic tunneling of an electron from the tip into final states inside the ZnO CB at higher bias voltages becomes a possible emission channel, which leads to a shifted cutoff in the STML spectra (cf. Fig. 2.6 in Theoretical Background) as observed by Krane et al.[30] Both mechanisms (energy transfer and charge injection) lead to a reduction of the intensity of higher photon energies above the CB energy. From the spectra shown in Fig. 4.3, we cannot infer which of the two processes dominates or alone is responsible for the observed STML spectra. In order to gain more insight into the prevailing mechanism (energy transfer versus charge injection), bias-dependent measurements at positive bias voltage (see subsection 4.2.1) and spatially resolved measurements (see subsection 4.2.2) are required and have been conducted.

4.2.1 Results of Positive Bias Dependence of STML on ZnO

The bias-dependent STML measurements at positive bias voltage have been conducted on 2 ML and 3 ML ZnO.

2 ML ZnO

Fig. 4.5 (A) shows the contour plot of the bias-dependent STML spectra where the relative photon yield $Y(h\nu)$ (cf. section 3.5) is plotted ($I_\mathrm{t} = 8\,\mathrm{nA}$). The corresponding STS spectrum (right panel) and plasmonic response on bare Ag(111), $I_\mathrm{ref}(h\nu)$, recorded at V_ref of 3 V (upper panel) are also shown. The energies of the CBE with respect to the Fermi level (1.91 eV) and CBE-IS transition (2.11 eV) are marked as light green and red dashed lines, respectively. Line spectra of $Y(h\nu)$ are given in the Appendix (see Fig. 7.3 (A)). The light grey part of the plasmonic response (upper panel) at lower photon energies is a rough estimate of the

contribution originating from second order diffraction. The grey area is very difficult to deconvolute and hence, $Y(h\nu)$ is not considered below photon energies of about 1.45 eV.

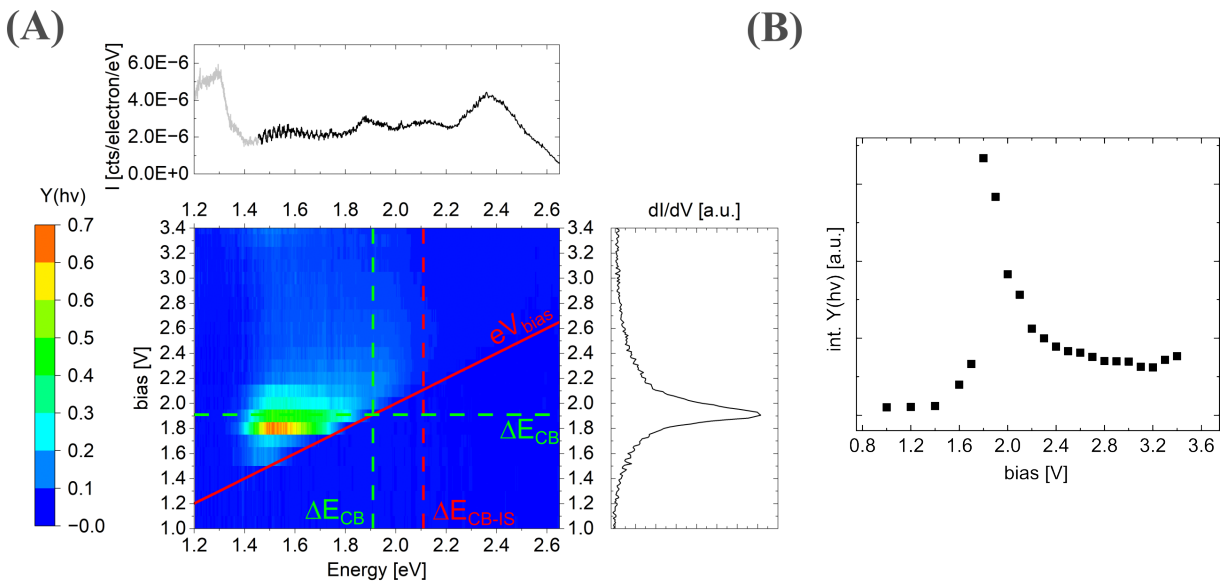

Figure 4.5: Contour plot (A) of the bias-dependent STML spectra (relative photon yields $Y(h\nu)$) on 2 ML ZnO in constant current mode at 8 nA. The upper panel in (A) exhibits the plasmonic response on the bare Ag(111) at 3 V and 3 nA and the right panel in (A) the STS spectrum on the ZnO island in constant current mode at 100 pA. The light grey part of the plasmonic response on the bare Ag(111) originates from second order diffraction. The CBE-IS transition energy (light green dashed line), the CBE energy relative to Fermi level (red dashed line) and the quantum cutoff (red solid line) are marked. (B) shows the integrated $Y(h\nu)$ as a function of the bias voltage. Line spectra of $Y(h\nu)$ and the STML data only normalized to the electrons are shown in Fig. 7.3 (see Appendix).

All spectra exhibit a broad response regarding the photon energy which evolves to higher photon energies due to the quantum cutoff (red solid line). Above a bias voltage of 2.2 V, the intensity is limited by a bias-independent emission cutoff around the energy of the IS-CBE transition (red dashed line). That means that the intensity above the photon energy of the CBE decreases even though the plasmon of the STM junction shows its absolute maximum at around 2.4 eV. As seen in the plot of the integrated $Y(h\nu)$ as a function of the bias voltage (Fig. 4.5 (B)), the largest integrated $Y(h\nu)$ is observed at a bias voltage of 1.8 V corresponding to the onset of the CBE. The integrated $Y(h\nu)$ continuously decreases above a bias voltage of 1.8 V. The photonic DOS strongly decreases below 1.45 eV (red-tail of the plasmon), which explains that the first integrated $Y(h\nu)$ starts to appear above a

bias voltage of 1.6 V and the decrease of intensity below photon energies of 1.5 eV.
While the data set in Fig. 4.5 presents only STML spectra to a bias voltage of 3.4 V, Fig. 4.6 exhibits STML spectra to a bias voltage of 4 V and shows some interesting behaviour at higher bias voltages. At lower bias voltages, the contour plots are similar. Above a bias voltage of 3.4 V, the integrated $Y(h\nu)$ starts to increase again (see Fig. 7.4 in Appendix). The broad response in $Y(h\nu)$ shifts to higher photon energies and decreases according to a quantum cutoff shifted by the energy of the CBE described by the yellow solid line ($eV_{\mathrm{bias}} - \Delta E_{\mathrm{CB}}$, cf. Fig. 2.6 in subsection 2.1.2).

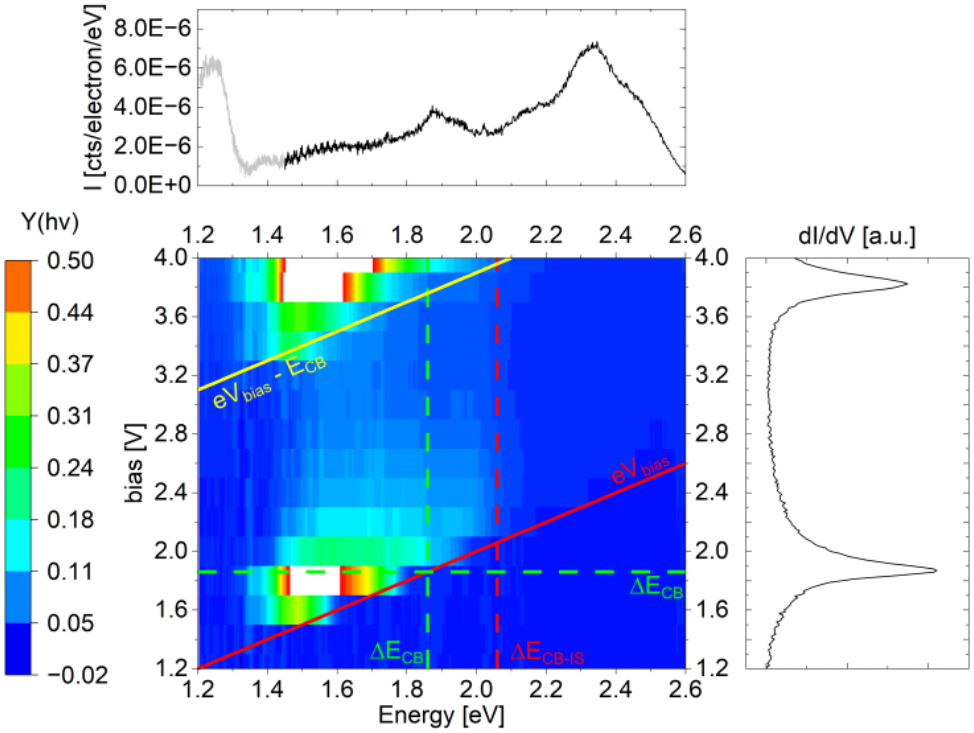

Figure 4.6: Contour plot of the bias-dependent STML spectra (relative photon yields $Y(h\nu)$) on 2 ML ZnO in constant current mode at 8 nA. The upper panel exhibits the plasmonic response on the bare Ag(111) at 3 V and 3 nA and right panel the STS spectrum on the ZnO island in constant current mode at 100 pA. The light grey part of the plasmonic response on the bare Ag(111) originates from second order diffraction. The STS peak at 3.8 V corresponds to the first FER state. The CBE-IS transition energy (light green dashed line), the CBE energy relative to Fermi level ΔE_{CB} (red dashed line) and the quantum cutoff (red solid line) are marked. Additionally, a shifted cutoff ($eV_{\mathrm{bias}} - \Delta E_{\mathrm{CB}}$) is marked as yellow solid line.

3 ML ZnO

Fig. 4.7 (A) shows the bias-dependent STML measurement as the relative photon yield $Y(h\nu)$ on 3 ML ZnO as contour plot in the range from 1 V to 2.5 V. The corresponding line spectra are given in Fig. 7.5 (A). The STML spectra have been measured in constant current mode at a tunneling of current of 50 nA. The light green dashed line and the red dashed line mark the energy of the CBE of 3 ML ZnO with respect to the Fermi level (1.43 eV) and the IS-CBE transition energy (1.63 eV), respectively.

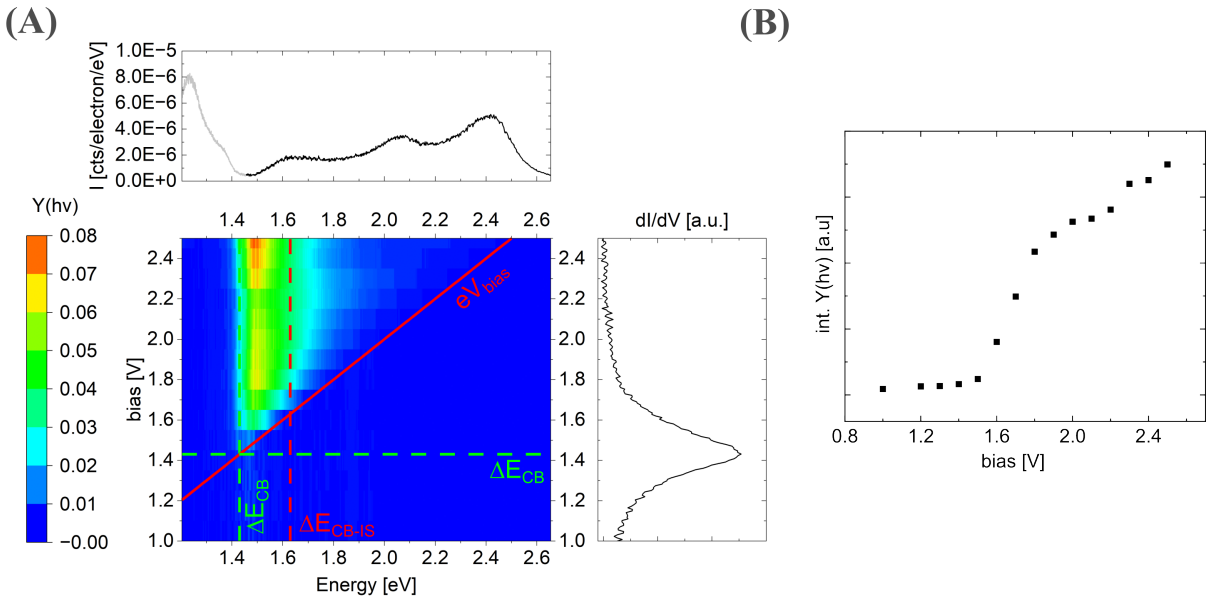

Figure 4.7: Contour plot (A) of the bias-dependent STML spectra (relative photon yields $Y(h\nu)$) on 3 ML ZnO in constant current mode at 50 nA. The upper panel in (A) exhibits the plasmonic response on the bare Ag(111) at 3 V and 3 nA and the right panel in (A) the STS spectrum on the ZnO island in constant current mode at 100 pA. The light grey part of the plasmonic response on the bare Ag(111) originates from second order diffraction. The CBE-IS transition energy (light green dashed line), the CBE energy relative to Fermi level (red dashed line) and the quantum cutoff (red solid line) are marked. (B) shows the integrated $Y(h\nu)$ as a function of the bias voltage. Line spectra of $Y(h\nu)$ and the STML data only normalized to the electrons are shown in Fig. 7.5 (see Appendix).

As on 2 ML ZnO, $Y(h\nu)$ is limited by the decrease of photonic DOS at lower photon energies (below 1.45 eV) and limited by the quantum cutoff (red solid line, eV_{bias}) to higher photon energies. Independent on the bias voltage, $Y(h\nu)$ exhibits an emission cutoff at about

1.5 eV (in-between the CB energy and the IS-CBE transition energy) with a significant decrease of $Y(h\nu)$ at larger photon energies. The integrated intensity shown in Fig. 4.7 (B) is monotonously increasing, in contrast to 2 ML ZnO, and thus the observed behaviour on 2 ML and 3 ML is quiet different. $Y(h\nu)$ is one order of magnitude smaller on 3 ML than on 2 ML likely due to a larger Ag tip to Ag(111) surface gap distance resulting in a weaker plasmonic field. Before starting the detailed discussion and interpretation of these data, spatially resolved measurements and the correlation of the STML spectra with the local electronic structure are shown in the next subsection 4.2.2.

4.2.2 Results of Spatial Mapping of STML on ZnO

The alternation of the electronic structure on purpose and the local dependence of the electronic structure on the STML response can give more insight into the mechanism at hand (energy transfer versus charge injection) as the states residing near the CBE of ZnO are directly involved in the light-emitting step in the charge injection mechanism (see Fig. 4.4 (B)). A detailed discussion on the destruction of the ZnO islands can be found on page 78 in the Appendix.

Local Dependence on Electronic Structure

The electronic structure was locally altered on 2 ML ZnO and Fig. 4.8 shows the STML results of the local dependence on the electronic structure. Subplot (A) and (B) show the STM image ($V_{\mathrm{bias}} = 1\,\mathrm{V}$, $I_{\mathrm{t}} = 100\,\mathrm{pA}$) and STS map ($V_{\mathrm{bias}} = 1.87\,\mathrm{V}$, $I_{\mathrm{t}} = 100\,\mathrm{pA}$, $V_{\mathrm{mod}} = 20\,\mathrm{mV}$) of a 2 ML ZnO island before destruction, respectively. The STM image shows a defect-free moiré pattern, which is also visible in the STS map. The positions of STS and STML spectra are marked as red numbers in (A) and (B). (C) shows the STS spectra ($I_{\mathrm{t}} = 100\,\mathrm{pA}$, $V_{\mathrm{mod}} = 30\,\mathrm{mV}$) before destruction which exhibit a sharp peak at 1.85 V independent on the tip position. Subplot (D) depicts the corresponding STML spectra ($V_{\mathrm{bias}} = 2\,\mathrm{V}$, $I_{\mathrm{t}} = 8\,\mathrm{nA}$) with no deviation between the spectra. STML intensity is measured at photon energies within the quantum cutoff of 2 eV and the plasmonic enhancement function with its red-tail at about 1.4 eV.

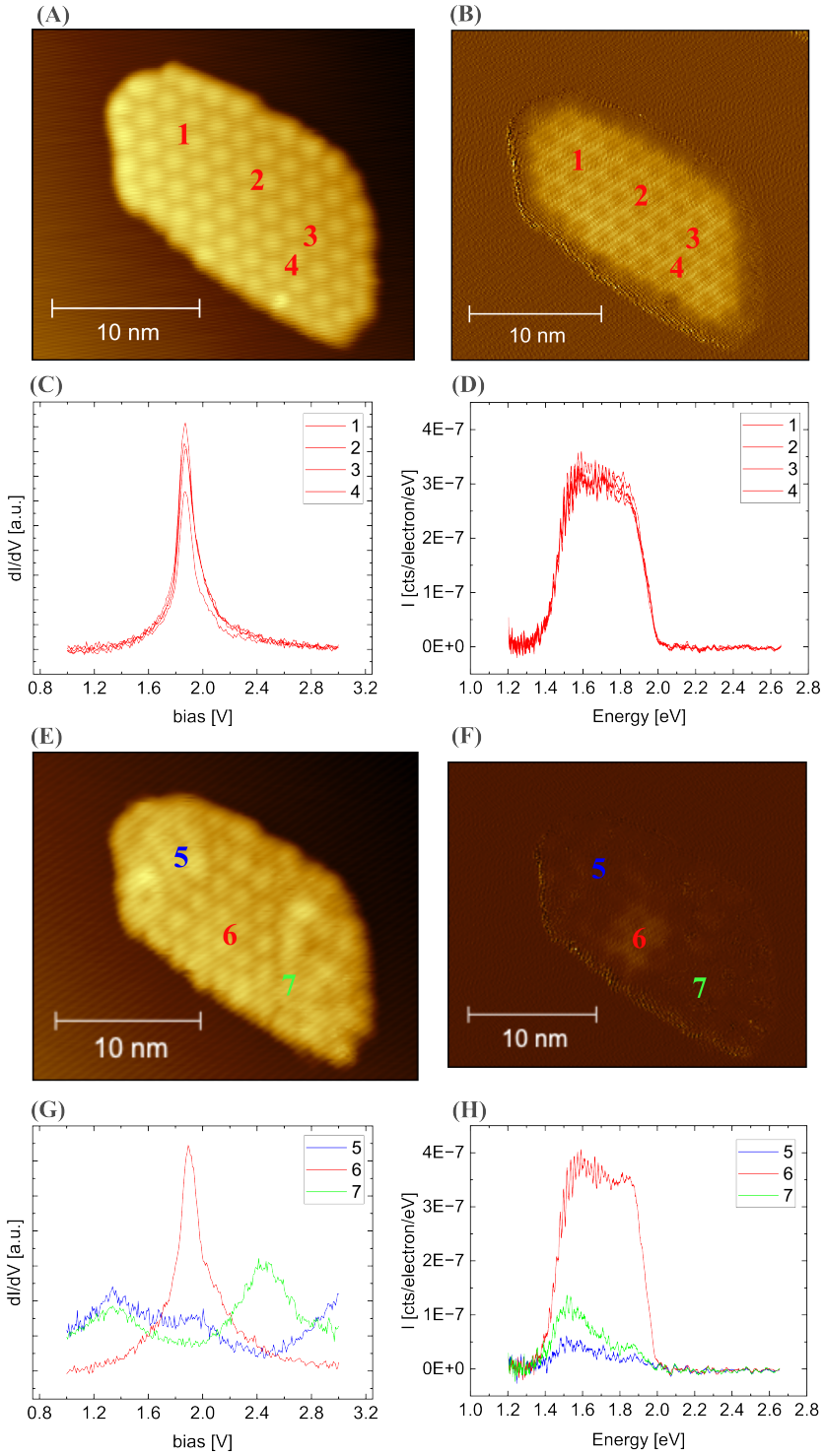

Figure 4.8: STM images ($V_{\text{bias}} = 1\,\text{V}$, $I_t = 100\,\text{pA}$) of a 2 ML ZnO island before (A) and after destruction (E). The island was destroyed at $V_{\text{bias}} = 3.7\,\text{V}$ and $I_t = 8\,\text{nA}$. The corresponding STS maps ($V_{\text{bias}} = 1.85\,\text{V}$, $I_t = 100\,\text{pA}$) are given in (B) before and in (F) after destruction. The positions of the STS and STML spectra are marked in the STM images and STS maps (1-7, colour-coded). The STS spectra before (C) and after destruction (G) are measured at $I_t = 100\,\text{pA}$ and the STML spectra before (D) and after destruction (H) are measured at $V_{\text{bias}} = 2\,\text{V}$, $I_t = 8\,\text{nA}$.

The moiré pattern of the 2 ML ZnO island was partially destroyed (vanished) at a bias voltage of $V_{\text{bias}} = 3.7\,\text{V}$ and tunneling current of $I_{\text{t}} = 8\,\text{nA}$. The STM image and STS map of the same 2 ML ZnO island after destruction is given in (E) and (F), respectively. The colour-coded numbers from 5 to 7 mark the positions of the STS spectra given in (G) and STML spectra given in (H). According to the STM image and STS map, position 5 and 7 mark areas with a destroyed moiré pattern with low intensity in the STS map and position 6 marks an area with an intact moiré pattern and intensity in the STS map. Only position 6 exhibits a well-defined sharp peak at 1.89 V in the STS spectra and the corresponding STML spectra 6 displays the same broad response as before the destruction. The electronic structure is strongly altered at the positions 5 and 7 and one does not observe a well-defined CB anymore but ill-defined electronic structure, as the STS response is very broad. Compared to position 7, the electronic DOS is larger at position 5 below 2 V. The integrated intensities of the STML spectra at position 5 and 7 are much lower compared to the intact area with a maximum at a photon energy of 1.55 eV. The lowest integrated intensity is found at position 5. We can thus conclude that in order to observe strong luminescence, it is necessary to have a sharp STS peak and well-defined electronic structure. This spatially resolved STML measurement with a resolution of a few nm supports that STML is a tool to locally probe optical transitions in the sample and the influence of the local electronic structure on these optical transitions.

Lateral Distance Dependence

Charge injection is localized by the tunneling current, whereas energy transfer can happen on the length scale of a few nm. Hence, an approach to distinguish an energy transfer process from STML induced by charge injection is a lateral distance dependence measurement near a 3 ML ZnO island as schematically depicted in Fig. 7.8 (see Appendix). Imada et al. reported a lateral distance dependence of the interaction of the LSP of the junction with an electronic transition of an adsorbed molecule via energy transfer.[37] If the plasmon is interacting with the IS-CBE transition according to (2) in Fig. 4.4 (A), one expects a lateral distance dependence of the plasmonic response on the bare Ag(111) surface near a 3 ML ZnO island.

Fig. 4.9 depicts the results of the lateral distance measurement with the corresponding STM image of the 3 ML ZnO island (A). At each position (number- and colour-coded) a STML spectrum (2 V and 8 nA) has been taken as shown in (B). Fig. 4.9 (E, left axis) shows the z position of the Ag tip (1-20) plotted versus the lateral distance with its origin at the first measurement position (1). As seen in the height profile, the points 1 to 7 are still on the bare

Ag(111) surface. The STML spectra from 1 to 7 show the same intensity and broad peak form. The broad response in the STML spectra on the bare Ag(111) (1 to 7) is ascribed to the plasmonic response of the Ag tip-Ag(111) junction restricted by the quantum cutoff of 2 eV (black dashed line). No change of the STML spectrum is observed from point 1 to 7. As soon as the Ag tip reaches the edge of the ZnO island, which can be judged from the tip retraction in the height profile, the STML intensity starts to decrease (spectrum 8). Please note that the numbers in the STM image are slightly displaced from the actual measurement positions due to a thermal drift of the sample. This is evident from the comparison of the positions in the STM image and the height profile. All further measurement points (9 to 20) show a similar and much weaker intensity (B) as soon as the electrons can tunnel into the ZnO island (see height profile in E). From 9 to 20, the tip retracts by about 6 Å until the height saturates at 18. Hence, the edge of the 3 ML ZnO island is smeared out. In order to better compare the peak form of the broad response, all STML spectra have been normalized to a photon energy of 1.4 eV (C). The STML spectrum 8 exhibits the same peak form as the previous measurement points. (C) shows that the peak form changes from point 8 to 9 on a length scale below 0.5 nm, which is even more localized than the tip retraction. Photon energies above 1.6 eV are reduced with respect to the first measurement points. The right axis of (E) shows the ratio I/I_0 of the normalized spectra in (C) at different photon energies (1.65 eV, 1.7 eV and 1.8 eV) with respect to the first measurement point (I_0). At all three photon energies, I/I_0 is nearly constant on the bare Ag(111) surface and drops very steep from 8 to 9. (D) exhibits all STML spectra normalized to its maximum and horizontally shifted. It can be readily seen that the maximum on bare Ag(111), which is determined by the quantum cutoff, shifts very steeply (marked by a black solid line) by 0.05 eV to lower photon energies as soon as the electrons can tunnel into 3 ML ZnO.

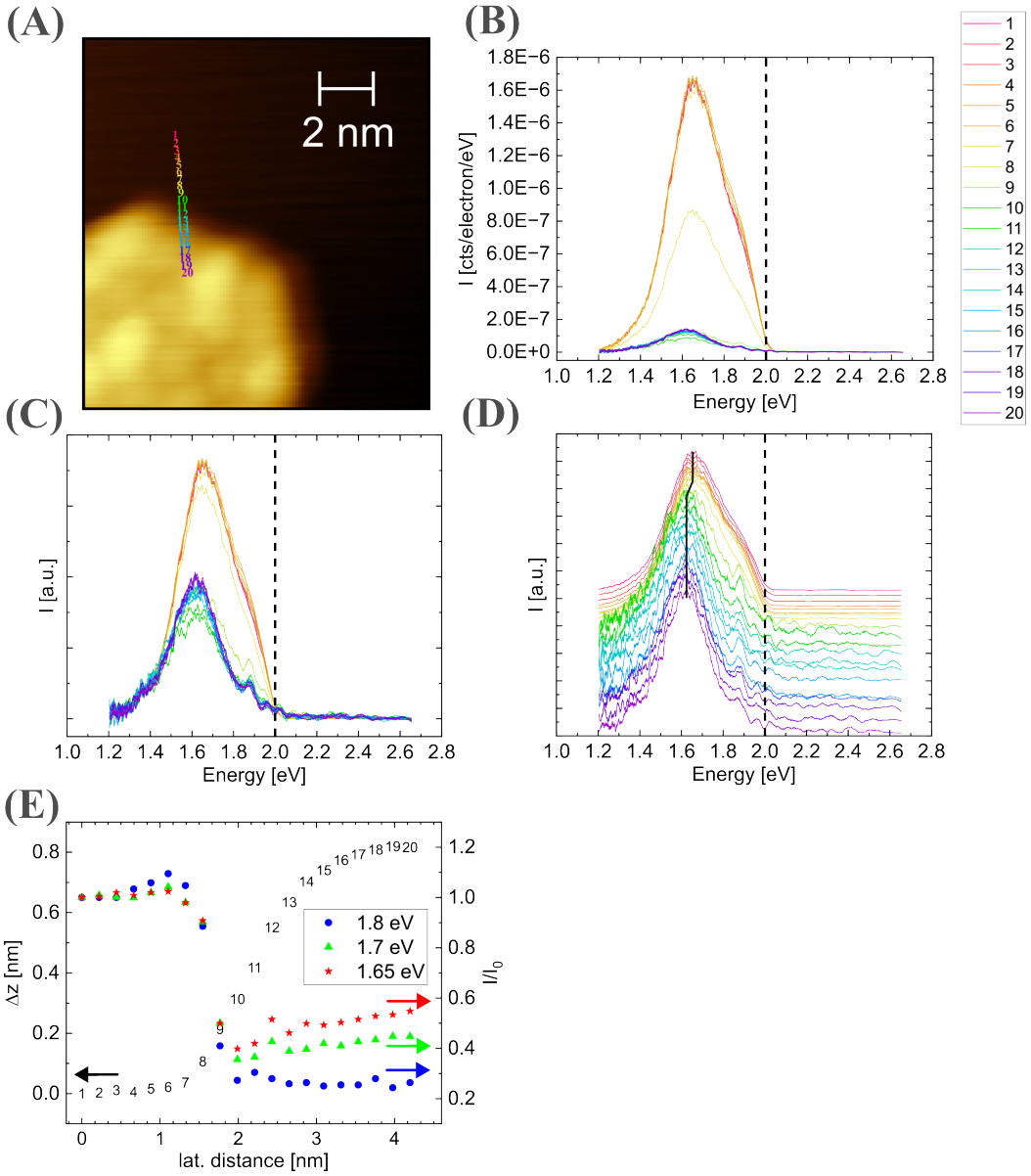

Figure 4.9: (A) STM image of a 3 ML ZnO island (1 V and 100 pA) with the positions (number and colour-coded) of the corresponding STML spectra which are shown in (B). The STML spectra have been taken at 2 V and 8 nA. The black dashed line marks the quantum cutoff. (C) shows the STML spectra normalized to a photon energy of 1.4 eV and (D) the spectra horizontally shifted and normalized to its maxima with a black solid line connecting them. The z positions of the STML spectra (height profile) are given as the position numbers in (E) on the left axis. Please note the mismatch between the positions in (A) and the height profile due to thermal lateral drift. The right axis of (E) shows the ratio (I/I_0) of the normalized spectra in (C) at three photon energies where I_0 corresponds to the first measurement point (1).

4.2.3 Discussion of Positive Bias Dependence and Spatial STML Mapping

This subsection will discuss the results of both previous subsections in the framework of Fig. 4.4 (energy transfer versus charge injection). The bias-dependent measurements on 2 and 3 ML ZnO clearly show STML spectra on ZnO do not originate from a pure plasmonic response of the junction at larger gap size, but are altered by the electronic structure of the ZnO. If it would be solely plasmonic luminescence from the radiative decay of the plasmon (step 1 in Fig. 4.4 (A)), $Y(h\nu)$ is expected to decrease proportional to $(eV_{\mathrm{bias}} - h\nu)$[92] and no bias-independent cutoff should be present[30]. $Y(h\nu)$ is plotted for the bare Ag(111) surface in Fig. 7.9 (see Appendix) with $V_{\mathrm{ref}} = 2.4\,\mathrm{V}$ and as expected decreases proportional to $(eV_{\mathrm{bias}} - h\nu)$. Thus, the absence of the linear decrease of $Y(h\nu)$ even below the CB and IS-CB transition energy is an argument against the energy transfer mechanism.
The intensity between the CBE and IS-CBE transition energy is not directly excluding the charge injection mechanism. According to the simplified picture in Fig. 4.4, the maximum photon energy achievable via charge injection is ΔE_{CB}. However, this schematic energy diagram is just showing the situation at the Γ-point. In fact, all states, IS and Ag bulk states, are occupied at the Γ-point.[42, 100] According to DFT calculations, the curvature of the ZnO-CB bands and the IS band is similar around the Γ-point.[42] Thus, radiative transitions with energies up to the IS-CBE transition energy at k-points deviating from the Γ-point are possible. Hence, it is difficult to distinguish energy transfer and charge injection only by analysing the cutoff photon energy.
Interestingly, the bias dependence behaves differently on 2 and 3 ML ZnO as seen in Fig. 4.5 and 4.7. However, the luminescence below the CBE of 3 ML ZnO could not be probed in the experiments shown here due to the decrease of photonic DOS, which also influences the position of the maximum in the STML spectra on 3 ML ZnO. The largest integrated intensity at the CBE of 2 ML ZnO is an indication of charge injection being the prevailing mechanism. The decrease of the integrated intensity above a bias voltage of 1.9 V might be caused by charge injection (step 1 in Fig. 4.4 (B)) and non-radiative quenching due to the transport of electrons to the ZnO/Ag(111) interface and into the Ag bulk without radiative transition (step 3 in Fig. 4.4 (B)). A similar quenching behaviour of the integrated intensity above a certain bias voltage threshold was observed on 3.5 nm thick Cu_2O films on Au(111) by Nilius et al.[21] Nilius et al. ascribed the observation to more localized and effective light-emitting states at the CBE due the higher probability of recombination.[21] They assigned the non-radiative loss of electrons at higher bias voltage to the injection of electrons into delocalized states such that the electrons reach the Au interface without a radiative transition.[21] As in the case of Cu_2O/Au(111)[21], it seems that the states at the

CBE of 2 ML ZnO are more effective light-emitting.
If the observed luminescence would stem from the radiative decay of the plasmon (step 1 in Fig. 4.4 (A)), one would not expect such a large increase of integrated intensity from 1.7 V to 1.8 V when the tip retracts by about 0.5 Å (see Fig. 3.6) and the plasmonic field strength is weakened. Additionally, step 1 in Fig. 4.4 (A) and the tip retraction by 3 Å are likely not responsible for the decrease of integrated intensity above a bias voltage of 1.8 V as estimated by a current-dependent measurement (see subsection 4.2.5). Fig. 4.13 shows the current-dependent STML spectra on 2 ML. The change in STML intensity in Fig. 4.13 originates from the different gap distances and weakened plasmonic field strength. From 90 nA to 15 nA, the integrated intensity decreases by 16 percent. This change in tunneling current corresponds to a tip retraction of roughly 1 Å. Hence, the tip retraction alone likely does not explain the decrease of integrated intensity above a bias voltage of 1.8 V. Despite the tip retraction on 3 ML ZnO at the CBE, the integrated intensity increases, which also excludes the energy transfer mechanism.
Because the integrated intensity is increasing on 3 ML ZnO, the non-radiative loss into the Ag bulk seems to not play such a large role as on 2 ML ZnO. The increase of the integrated intensity is not expected in constant current mode and in the framework of charge injection (Fig. 4.4 (B)) and correlates with an increase of remaining intensity at photon energies above the IS-CB transition energy. This might be explained with radiative transitions above the CBE (hot luminescence) or a superposition of radiative decay of the plasmon (step 1 in Fig. 4.4 (A)) and radiative transition at the CBE (step 2 in Fig. 4.4 (B)). The different coupling of CB states (above the CBE) to the Ag bulk (localization of CB states) regarding 2 and 3 ML ZnO could originate from their differences in geometry, electronic structure and/or thickness. Due to the thickness of 4 ML ZnO and a similar structure to 3 ML ZnO, we expect a bias-dependent behaviour on 4 ML similar to 3 ML.
The results of the local dependence on the electronic structure on the damaged ZnO island (Fig. 4.8) are ambivalent. As the initial states of the radiative transition (step 2 in Fig. 4.4 (B)) in the charge injection framework reside at the CBE of ZnO and are seemingly effective light-emitting, a degradation of these electronic states and their density results in a weaker STML intensity. The remaining intensity at the damaged areas might originate from radiative transitions from the altered CB states which is in accordance with a pronounced maximum at 1.55 eV. However, intensities in STS and STML are interchanged on the damaged areas which seem to contradict the radiative transition from the CBE. This contraction might be explained by the different spatial extents of the tunneling current (STS) and the plasmonic field (STML) such that areas close to the tip contribute to the

STML response. The shifted CBE could also result in quenching (via energy transfer) of photon energies below the quantum cutoff due to a shifted IS-CBE transition.
The observation of no lateral distance dependence on the bare Ag(111) surface in close proximity to the ZnO edge (see Fig. 4.9) excludes that energy transfer is responsible for the reduction of higher photon energies. The steep shift of the broad STML response to lower photon energies as soon as electrons can tunnel into the 3 ML ZnO might be an indication for charge injection with subsequent relaxation. However, a higher quantum cutoff and more red-shifted plasmonic structure (e.g. with Au tips on Ag(111)[31]) would allow us to characterize the observed spectral changes in more detail.
So far, we have only discussed results below bias voltages below 3.4 V. In contrast, the next paragraph will cover the observation above a bias voltage of 3.4 V in the bias-dependent STML measurement. The continuous increase of integrated intensity on 2 ML ZnO above 3.4 V with its shifted cutoff by the energy of the CBE is an indication that both processes, radiative decay of the plasmon (step 1 in Fig. 4.4 (A)) and radiative transition at the CBE (step 2 in Fig. 4.4 (B)), can occur in different bias voltage regimes. This luminescence originating from step 1 (Fig. 4.4 (A)) with final states near the CBE was observed by Krane et al. on quasi-freestanding MoS_2 nanopatches on Au(111).[30] The presence of the shifted cutoff indicates that the radiative decay of the plasmon according to step 1 (Fig. 4.4 (A)) is not efficient when final states are located inside the band gap. It is surprising to observe a sharp shifted cutoff with increasing integrated intensity for several reasons. First, the first FER state (at 3.8 V) should have an indirect effect on the STML intensity due to tip retraction (larger than 2.5 Å) and the availability of a new channel (tunneling into the first FER state) can lead to quenching as observed by Martínez-Blanco et al.[59]. Second, the CB states of ZnO undergo a significant alternation at higher bias voltages.

The data at positive bias voltage supports the charge injection mechanism (Fig. 4.4 (B)), where fast relaxation leads to a reduction of high photon energies. The most reliable way to deconvolute possible contributions from electronic and plasmonic structure and to distinguish the energy transfer and charge injection mechanism is to measure the bias dependence at negative bias voltages (see next subsection 4.2.4).

4.2.4 Negative Bias Dependence of STML on ZnO

The bias-dependent STML measurements have been conducted at negative bias voltage on 2 and 3 ML ZnO. Possible processes are depicted in Fig. 4.10. At negative bias voltage, the electrons tunnel elastically (1) and inelastically (2) from the ZnO/Ag(111) surface into the

Ag tip. The inelastic tunneling process excites the LSP of the junction which radiatively decays (2). As seen in the previous sections, luminescence at positive bias voltages is strongly influenced by the electronic structure (CB) of ZnO, which made it difficult to distinguish energy transfer and charge injection as mechanism responsible for the reduction of intensity at high photon energies. However, at negative bias voltage only contributions from the radiative decay of the LSP of the junction (2) to the STML response are expected. Thus, quenching of higher photon energies via energy transfer (3) is much easier to confirm or disprove at negative bias voltages. According to Stróżecka et al., the relative photon yield $Y(h\nu)$ is expected to decrease proportional to $(eV_{\text{bias}} - h\nu)$ due to the shrinking energy window and possibility to create a photon with the energy $h\nu$.[92] $Y(h\nu)$ is plotted for the bare Ag(111) surface (compare to Fig. 4.1) in Fig. 7.9 (see Appendix) with $V_{\text{ref}} = 2.4\,\text{V}$. As expected, the decrease is proportional to $(eV_{\text{bias}} - h\nu)$ with small deviations near the quantum cutoff. If the plasmonic response is quenched by the IS-CB transition, one would expect deviations from a linear decrease above the photon energy of the IS-CB transition energy.

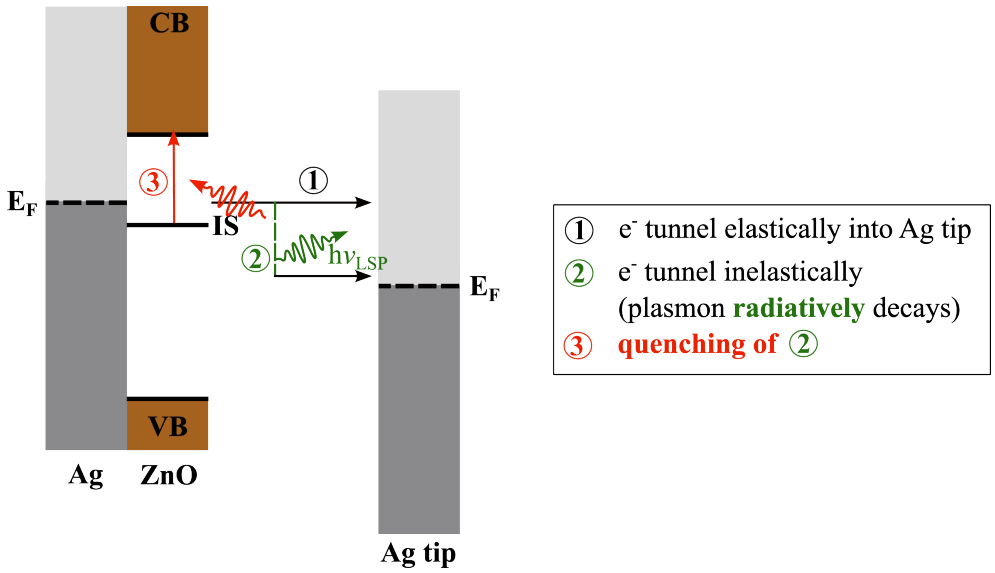

Figure 4.10: Schematic energy diagram of the ZnO/Ag(111)-Ag tip junction at negative bias voltage with possible processes.

The results of the bias-dependent STML measurements on 2 and 3 ML ZnO at negative bias voltage in constant current mode at 40 nA are given in 4.11 and 4.12, respectively. (A) shows the contour plot of the relative photon yield $Y(h\nu)$ and exhibits the spectra as a function of the magnitude of the bias voltage. Please note that the data set in Fig. 4.11 of

2 ML is not sensitive to the examination of possible quenching because the bias voltage in this measurement is limited to −2 V. This limitation is caused by instabilities of the ZnO/Ag(111)-Ag tip junction at lower bias voltages. At low bias voltages below −2 V, it was observed multiple times that the Ag tip left material (most likely Ag atoms from the apex) on the ZnO islands (see Fig. 7.10 in Appendix).

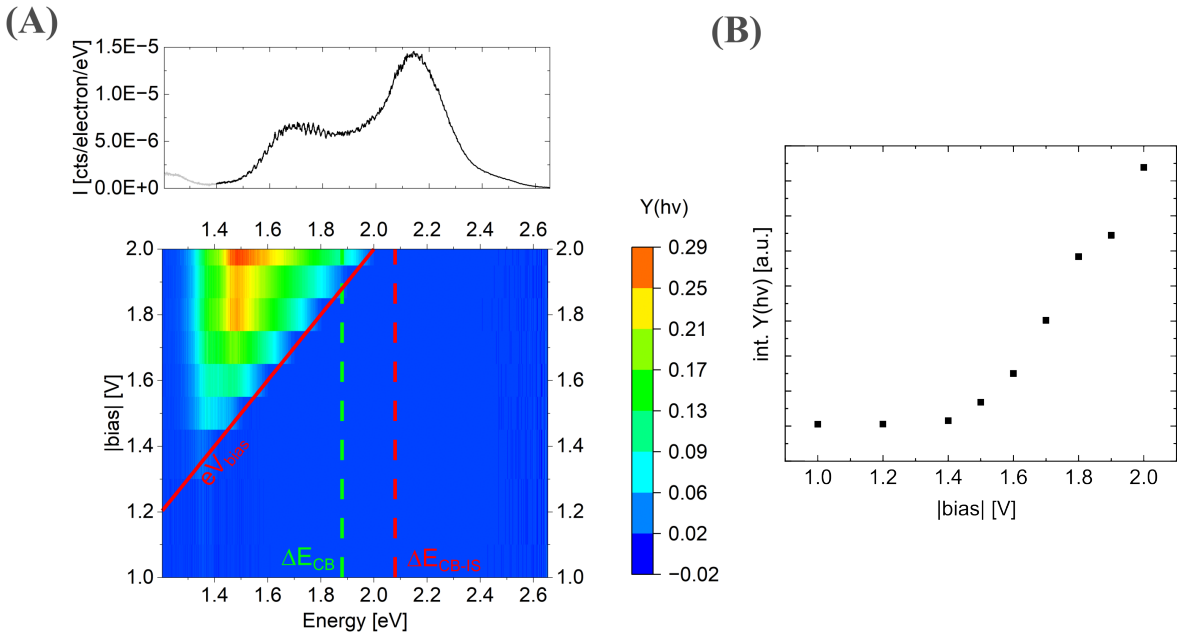

Figure 4.11: (A) Contour plot of the bias-dependent STML spectra (relative photon yields $Y(h\nu)$) on 2 ML ZnO at negative bias voltage in constant current mode at 40 nA. The upper panel in (A) exhibits the plasmonic response on bare Ag(111) at 3 V and 3 nA. The light grey part of the plasmonic response on bare Ag(111) originates from second order diffraction. The CBE-IS transition energy (light green dashed line), the CBE energy relative to Fermi level (red dashed line) and the quantum cutoff (red solid line) are marked. (B) shows the integrated $Y(h\nu)$ as a function of the bias voltage. Line spectra of $Y(h\nu)$ and the STML data only normalized to the electrons are shown in Fig. 7.11 (see Appendix).

For 2 ML and 3 ML, $Y(h\nu)$ shifts to higher photon energies with decreasing bias voltage due to the quantum cutoff (see red solid line) and increasing energy window. As expected for photon energies below the energy of the IS-CBE transition, $Y(h\nu)$ decreases proportional to $(eV_{\text{bias}} - h\nu)$ (see Fig. 7.11 (A) and 7.12 (A)) which means the radiative decay of the plasmon is observed (step 2). Interestingly, $Y(h\nu)$ is larger than 1 between 1.4 eV and 1.6 eV which means the luminescence is stronger on the 3 ML ZnO than on 2 ML and on bare

Ag(111). This is not expected because the Ag(111)-Ag tip distance is much larger and hence the plasmonic field weaker. It is also very peculiar that −1.7 V yields the largest maximum in $Y(h\nu)$ compared to −1.8 V and −1.9 V. Despite this unexpected behaviour and change, there is no indication of reduction of higher photon energies via energy transfer (step 3) on 3 ML ZnO because there is no deviation from the smooth decay proportional to $(eV_{\mathrm{bias}} - h\nu)$ (see Fig. 7.12 (A)).

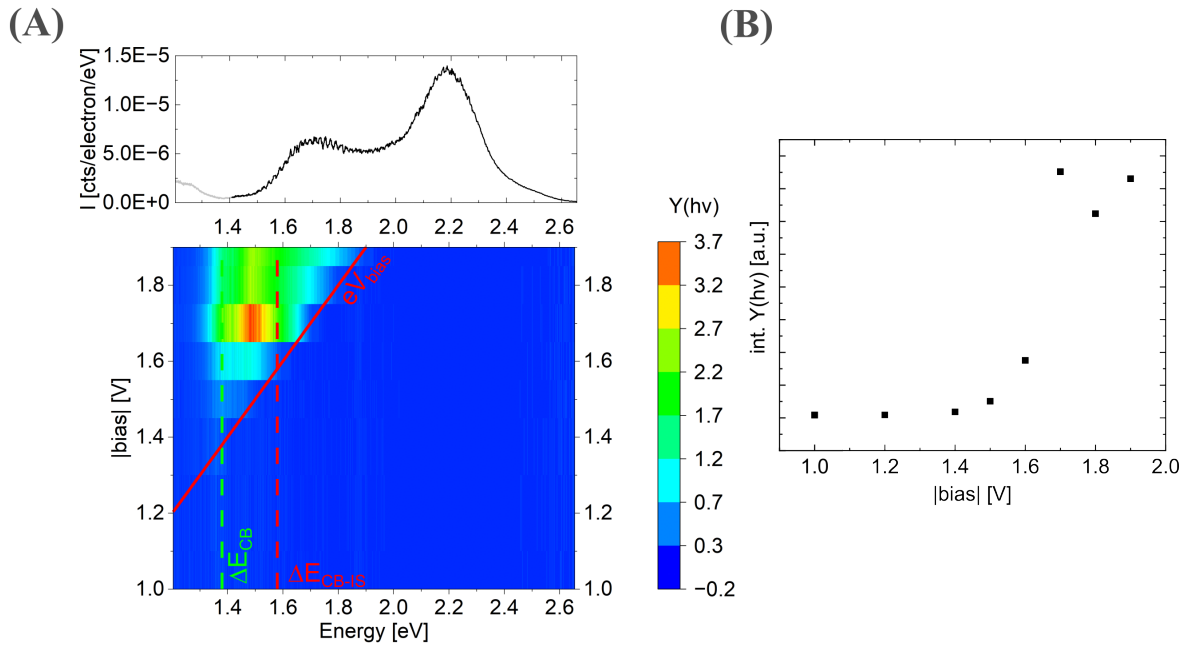

Figure 4.12: (A) Contour plot of the bias-dependent STML spectra (relative photon yields $Y(h\nu)$) on 3 ML ZnO at negative bias voltage in constant current mode at 40 nA. The upper panel in (A) exhibits the plasmonic response on bare Ag(111) at 3 V and 3 nA. The light grey part of the plasmonic response on bare Ag(111) originates from second order diffraction. The CBE-IS transition energy (light green dashed line), the CBE energy relative to Fermi level (red dashed line) and the quantum cutoff (red solid line) are marked. (B) shows the integrated $Y(h\nu)$ as a function of the bias voltage. Line spectra of $Y(h\nu)$ and the STML data only normalized to the electrons are shown in Fig. 7.12 (see Appendix).

However, a different data set on 2 ML ZnO to lower bias voltages (−2.7 V) where the Ag tip left material on the surface indicates a reduction of higher photon energies (see Fig. 7.13 in Appendix). The integrated intensity decreases below −2.2 V which is not expected (see inset of Fig. 7.13). This decrease originates from an increase of the Ag(111)-Ag tip distance and change of the tip condition which affects the plasmon structure. Independent

on the tip condition and geometry, the absolute maximum is expected above 2 eV due to the intrinsic properties of the Ag(111)-Ag tip junction.[31, 59] Further studies are required to investigate this seemingly reduction of higher photon energies at negative bias voltages.

4.2.5 Current Dependence of STML on ZnO

The dependence of the STML spectra on the tunneling current has been probed in order to estimate the influence of the gap size on the STML response. Additionally, the order of the light-emitting process can be determined to give an insight into the mechanism. Fig. 4.13 shows the STML intensity on 2 ML ZnO as a function of the tunneling current from 10 nA to 90 nA. As depicted in (B), the integrated intensity decreases by about 16 percent from 90 nA to 15 nA which corresponds to an estimated tip retraction of about 1 Å. This decrease in integrated intensity is ascribed to a decrease of the plasmonic field strength due to the larger gap distance.

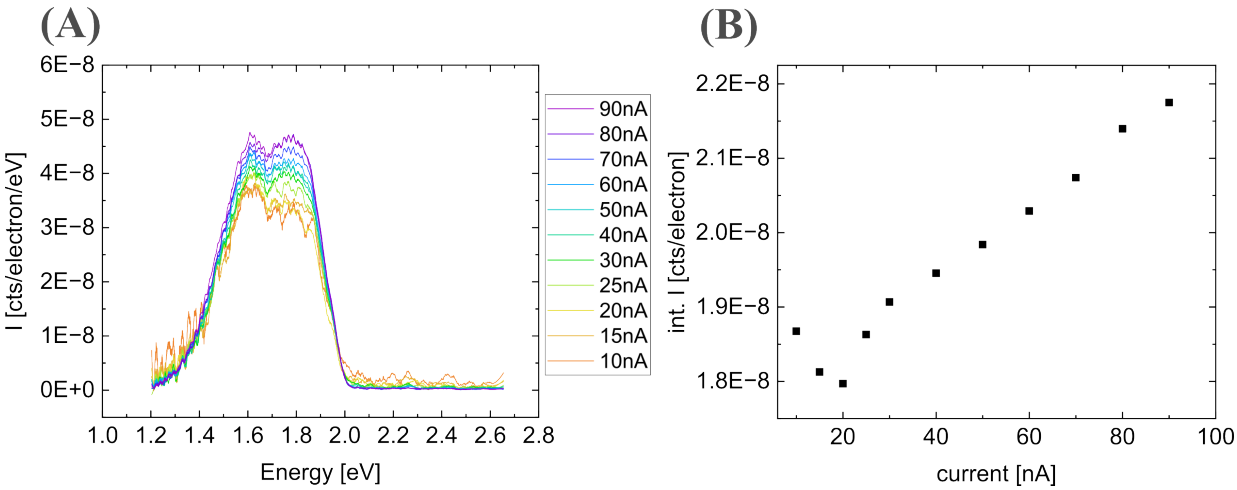

Figure 4.13: (A) The STML response on 2 ML ZnO dependent on the tunneling current (10 nA to 90 nA) at a constant bias voltage of 2 V. (B) shows the integrated intensity as a function of the tunneling current.

Under the assumption that the dependence of the tunneling current J on the integrated spectral intensity I follows a simple power law:

$$I = \alpha J^{\beta} \tag{4.1}$$

with a proportional factor α, we can extract β by logarithmizing the equation which is

obtained by dividing eq. 4.1 by a reference intensity-current pair:

$$\log(I/I_0) = \beta \log(J/J_0). \tag{4.2}$$

Thus, by fitting a linear function to eq. 4.2, the exponent β is obtained from the slope. Its value corresponds to the order of the process. The integrated spectral intensity I is determined from the STML spectra (normalized only to the integration time) in Fig. 7.14 (see Appendix). The data of the integrated spectral intensity is edited according to eq. 4.2 with $J_0 = 5\,\mathrm{nA}$. The linear fit according to eq. 4.2 is given in Fig. 4.14 for 2 ML (A) and 3 ML (B) ZnO. The slope is 1.06 and 1.08 on 2 ML and 3 ML ZnO, respectively. That means, the process which leads to the observed luminescence on the ZnO islands is a one-photon-electron process.

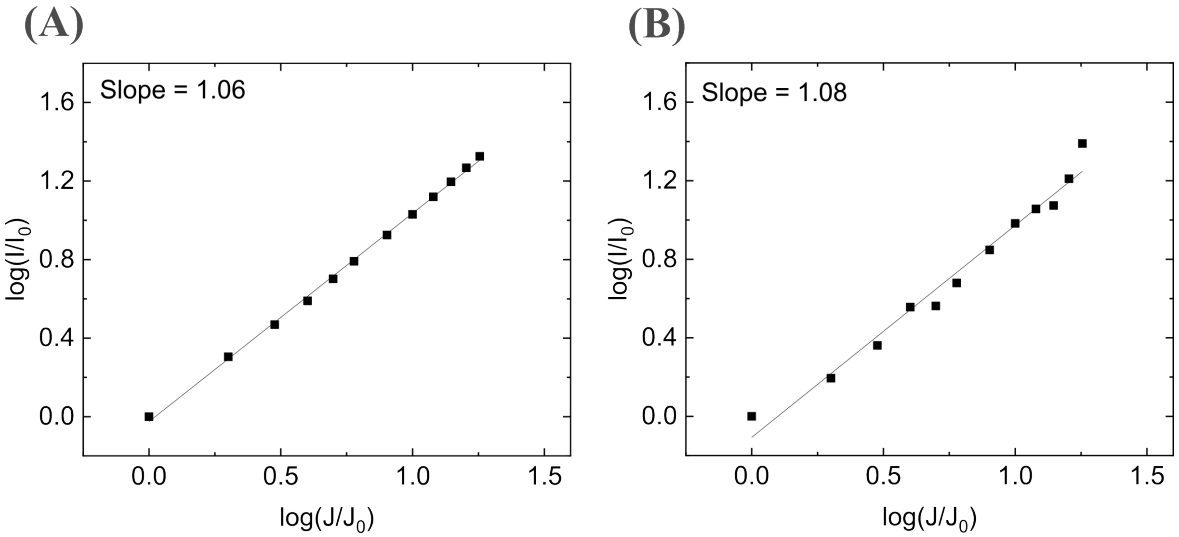

Figure 4.14: Plot of the logarithmized integrated intensity pairs I/I_0 versus logarithmized tunneling current pairs J/J_0 on 2 ML (A) and 3 ML (B) ZnO at a bias voltage of 2 V and with reference $J_0 = 5\,\mathrm{nA}$.

5 Conclusion and Outlook

In this master thesis STM-induced luminescence (STML) from ultra-thin ZnO films on Ag(111) was investigated. The goal of the measurements was to understand the influence of the electronic structure of the ZnO/Ag(111) sample on the luminescence spectra emitted from the plasmonic STM junction. Previous preliminary measurements of the group showed that the plasmonic STML spectra on bare Ag(111) are strongly altered by the presence of the ZnO. In particular, it was found that the STML spectra from ZnO/Ag(111) seem to exhibit characteristic shapes that indicate a strong contribution from the electronic IS-CBE resonance inside the ZnO/Ag(111) sample. The purpose of this thesis was to investigate the influence of the electronic structure and its interaction with the junction plasmon on the luminescence spectra.

In more detail, on 2 ML and 3 ML ZnO photon energies above the IS-CBE transition energy are strongly reduced at positive bias voltages, while the luminescence below this energy appears plasmonic in nature. There a two possible mechanism which could cause the reduction of higher photon energies. First, the electrons can inelastically tunnel inside the band gap and excite the junction plasmon which can be quenched by the IS-CB transition via energy transfer. The interaction between junction plasmons and molecular excitons via energy transfer, which leads to fano lineshapes, is known in the literature.[37] Liu et al. reported a strong coupling between the junction plasmon and the IS-CBE transition on ZnO/Ag(111).[43, 44] Second, electrons can tunnel into the CB of ZnO (charge injection) and undergo fast relaxation to CBE states due to electron-phonon coupling[44, 43]. In the last step, a radiative transition emerges from CBE states to final states (IS or Ag states) inside the band gap.[101, 99] This charge injection process showing plasmonic luminescence was observed on Cu_2O films on Au(111).[21] To better understand the origin of the observed luminescence changes and to gain insight into their physical mechanism, bias-dependent STML measurements and STML mapping of ZnO islands are performed.

The results of the positive bias-dependent measurement on 2 ML ZnO indicate that charge injection and fast relaxation to the CBE play an important role. Thus, the CBE states of ZnO are more efficient light-emitting. In contrast, quenching via the IS-CB transition by energy transfer can be ruled out with high probability by the lateral distance measurement

in close proximity to 3 ML ZnO and bias-dependent measurements at negative bias voltage. At positive bias voltages, the bias dependence reveals a bias-independent energy cutoff at around 2.1 eV and 1.5 eV for 2 ML and 3 ML ZnO, respectively, of the luminescence spectra. On 2 ML ZnO, strong luminescence is only observed when directly tunneling into the CBE. The decrease of integrated intensity above the CBE is ascribed to localized and effective light-emitting state residing at the CBE and delocalized states above the CBE leading to transport of the electrons into the Ag bulk.[21] This non-radiative loss into the Ag bulk was not pronounced in 3 ML ZnO. Current-dependent measurements showed that tip retraction at the CBE of 2 ML ZnO is not solely responsible for the decrease of integrated intensity and that the luminescence on 2 and 3 ML ZnO originates from an one-electron-photon process. Spatial STML mapping reveals that strong luminescence is only observed when the CB states around the CBE are not altered and the electronic structure is well-defined. The lateral distance measurement near a 3 ML ZnO island shows no dependence on the lateral distance whereas a distance dependence would be expected in case of energy transfer. Hence, the reduction of higher photon energies is ascribed to fast relaxation in the CB.
Unambiguous identification of the involved mechanism - charge injection versus energy transfer - can be expected from STML measurements at negative bias voltage. At negative bias voltage, tunneling into the ZnO-CBE is not possible, and consequently no luminescence from radiative recombinations of electrons at the CBE with holes in the IS/Ag(111) surface can be expected. In contrast, energy transfer would still be possible. Negative bias-dependent STML measurements indicate solely the radiative decay of the localized surface plasmon of the junction. The linear decrease of $Y(h\nu)$ indicate no deviation or sudden decrease around the energy of the IS-CBE transition energy. Thus, there is no indication of quenching via energy transfer even though further measurements at lower negative bias voltages are required to corroborate this.
A large part of the experimental work included the preparation of the ultra-thin ZnO films on Ag(111) and the optimization of the corresponding parameters. It turned out that the Zn rods in the ZnO preparation chamber are degrading so that they have to be exchanged in the near future for successive measurements. Hopefully, with fresh Zn rods much larger and more stable ZnO islands can be generated such as in previous studies, where no alternation of electronic structure and moiré pattern was observed.[12, 44, 42, 40] Additionally, the measurement temperature will be reduced to liquid helium temperature in the next machine time, which might also prevent the destruction of the ZnO and the instabilities of the junction at negative bias voltages. Moreover, the next measurements will be conducted with a plasmonic Au tip instead of a Ag tip because the localized surface

plasmon is intrinsically more red-shifted for Au tips.[31] Measurements on 3 ML with a Ag tip are more difficult and limited due to a low spectral overlap of the Ag tip plasmon with the CBE. Furthermore, plasmonic tips which exhibit a single broad plasmon peak without many spectral modulations are highly desired to simplify the analysis regarding the normalization. Such tips have been used before but require more time to be prepared.
So far, only electroluminescence has been considered. Another approach investigating the light-matter interaction in ultra-thin ZnO films on Ag(111) is Tip-Enhanced Photoluminescence (TEPL). TEPL has the advantage to even create possible final states in the IS at the Γ-point due to the optical excitation of IS-electrons at the Γ-point and creation of electron-hole pairs. Even though STML in ZnO is also based on the recombination of electrons and holes (away from the Γ-point), there is less control, e.g. due to the gap distance dependence. According to the radiative transitions at the CBE of ZnO observed in STML, one expects even stronger luminescence from the CBE-IS transition due to holes at the Γ-point. It would be interesting to probe how TEPL evolves by exciting electrons with a cw-laser from the IS to the CBE and above the CBE on 2 and 3 ML ZnO. According to the bias-dependent STML measurements at positive bias voltage in this thesis, radiative recombinations in TEPL resulting from excitation above the CBE is expected to be observed only on 3 ML ZnO because 2 ML ZnO indicates strong non-radiative loss into the Ag bulk.
We want to use the ultra-thin ZnO films on Ag(111) as versatile model system with unique optical properties (IS-CBE transition) for time-resolved measurements. Those time-resolved measurements will provide insight into the electron and lattice dynamics. Liu et al. detected coherent phonons (CPs) in 3 ML ZnO with a 2 nm resolution via the interferometric autocorrelation of the photocurrent[43] with the STM machine described in this thesis. However, the mechanism of the CP excitation is still an open question. First, optical spectroscopy via STML and TEPL might help to better under the time-resolved measurements. Second, time-resolved measurements with THz pulses and a tunable fs-laser, where the photon energy of the pump and probe pulse can each be tuned, will provide more insight. Moreover, the investigation is limited to 3 ML ZnO because the fixed wavelength is only resonant with the IS-CBE transition of 3 ML ZnO on Ag(111).[43] With a tunable fs-laser, there would the ability to investigate CPs in 2 ML ZnO on Ag(111) with high spatial resolution. In order to conduct these time-resolved measurements, the ZnO/Ag(111) sample has to be transferred to a different setup (THz-STM), which is equipped with a tunable fs-laser (650 nm-900 nm, OPA) and THz generator. However, the ZnO/Ag(111) sample is not stable under ambient conditions. In the extent of this thesis, an UHV suitcase has been constructed in order to conduct the transfer of the ZnO/Ag(111) sample between two different STM machines. The

UHV suitcase is described in the following part.

5.1 Construction of an UHV Suitcase and ZnO/Ag(111) Sample Transfer

Fig. 5.1 (A) shows a picture of the UHV suitcase attached to the load-lock (0) of the THz-STM and (B) the corresponding technical drawing. The main part of the UHV suitcase is the load-lock vessel (1) which consists of 6 ports. Three ports are rotatable DN40CF flanges (port 1, 3 and 4), two ports are DN40CF flanges (port 2 and 6) and one port is a DN63CF flange (port 5). All the stainless steel parts of the construction were prepared for UHV conditions. The inner and outer walls were glass ball blasted and all seams welded from the inner side. One DN40CF flange (port 4) is covered with a blind flange and another one (port 3) with a silica window in order to see the sample in the UHV suitcase during transfer. Port 1 and 2 are aligned along the main axis for the sample transfer. A Mini UHV-Schieber (from VAT) (2) is connected to port 1, which separates the UHV suitcase from the ambient surrounding during transport, from the load-lock (0) of the THz-STM and from the observation chamber of the STM machine during the sample transfer. In order to connect the UHV-Schieber to the load-lock of the THz-STM, an adapter DN63CF to DN40CF (2a) was required due to the UHV-Schieber only having two DN40CF flanges and the load-lock a DN63CF flange. The port 2 (opposite to port 1) is connected to a spacer with two DN40CF flanges (3), which itself is connected to the transfer rod (MOS 40-600, from VAb) (4). The sample holder tool (5) is connected to the transfer rod via an adapter tool (6). It provides some flexibility during sample transfers in case of slight misalignment. For measuring and monitoring the pressure inside the UHV suitcase, a cold cathode gauge (Pfeiffer) (7) is installed at port 6. Please note that the cold cathode gauge is missing in the technical drawing. Port 5 is connected to a Tee connector with three different sized flanges (rotatable DN63CF, DN40CF and DN16CF) (8). In order to maintain the pressure inside the UHV suitcase, a NEG/Ion Combination Pump (NEXTorr Z 200, from SAES Getters) (9) is attached to the DN40CF flange of the Tee connector. The advantage of the combination of a sputter ion pump and Non Evaporable Getter (NEG) pump is the small size (75 mm x 81 mm x 197.5 mm) and low weight (2.2 kg).[102] After activation of the NEG pump by thermal treatment, it will run at room temperature without any power supply. The getter has a large inner surface of 300 cm^2 composed of an alloy made from Zr, V, Ti and Al, which enables the chemisorption and absorption (retention) of gas

molecules.[102] This makes the NEG pump suitable for the sample transfer between two STM machines. The third flange (DN16CF) is connected to an angle valve (10). Under normal operation, the outlet flange (DN16CF) is closed by a blind flange. Once in a while, the getter has to be reactivated. Additionally, the UHV chamber has to be baked out after venting or in case of contamination. During bake-out and reactivation, pumping can be done either via the turbo pump of the load-lock (THz-STM) or over the angle valve with an external turbo pump. In order to have mechanical stability and avoid that the whole weight of the UHV suitcase lays on the flange to the load-lock, a post (11) on the optical table holds the weight of the UHV suitcase at the transfer rod.
The UHV suitcase was baked out once for 5 days with multiple heating tapes at a maximum temperature of 390 K via the turbo pump of the load-lock. Due to a minor leak in the load-lock, it was decided to close the gate valve to the load-lock and resume the bake-out (for additional 4 days) via pumping with an external turbo pump over the angle valve (DN16CF flange). Furthermore, one of the heating tapes was exchanged such that a higher maximum temperature of 410 K was reached. While the walls of the UHV suitcase were still at elevated temperatures, the NEG pump was activated for one hour (60 W). After closure of the angle valve and cool-down, a pressure of about 7×10^{-11} mbar was reached inside the UHV suitcase without any power supply.
Due to time constraints, it was not possible to attach the UHV suitcase to the STM machine, where the ZnO/Ag(111) sample is prepared, and to test the sample transfer between both STM machines. The UHV suitcase is supposed to be attached to the observation chamber of the STM machine via the gate valve of the observation chamber (DN40CF) and the gate valve of the UHV suitcase (2) connected by a Tee connector (2xDN40CF, DN16CF). The connection is pumped over the DN16CF flange by an external turbo pump in order to prevent contamination inside the observation chamber and UHV suitcase.

(A)

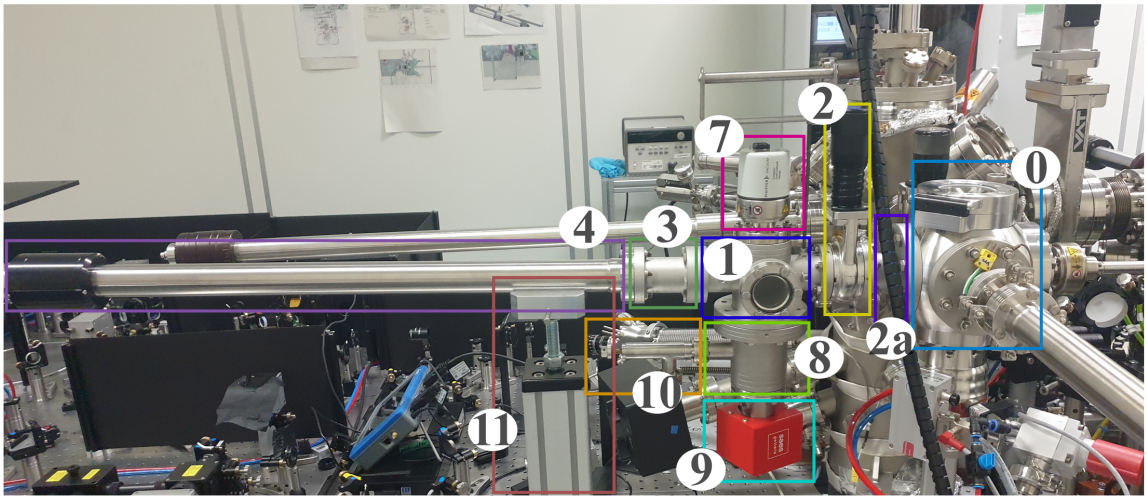

(B)

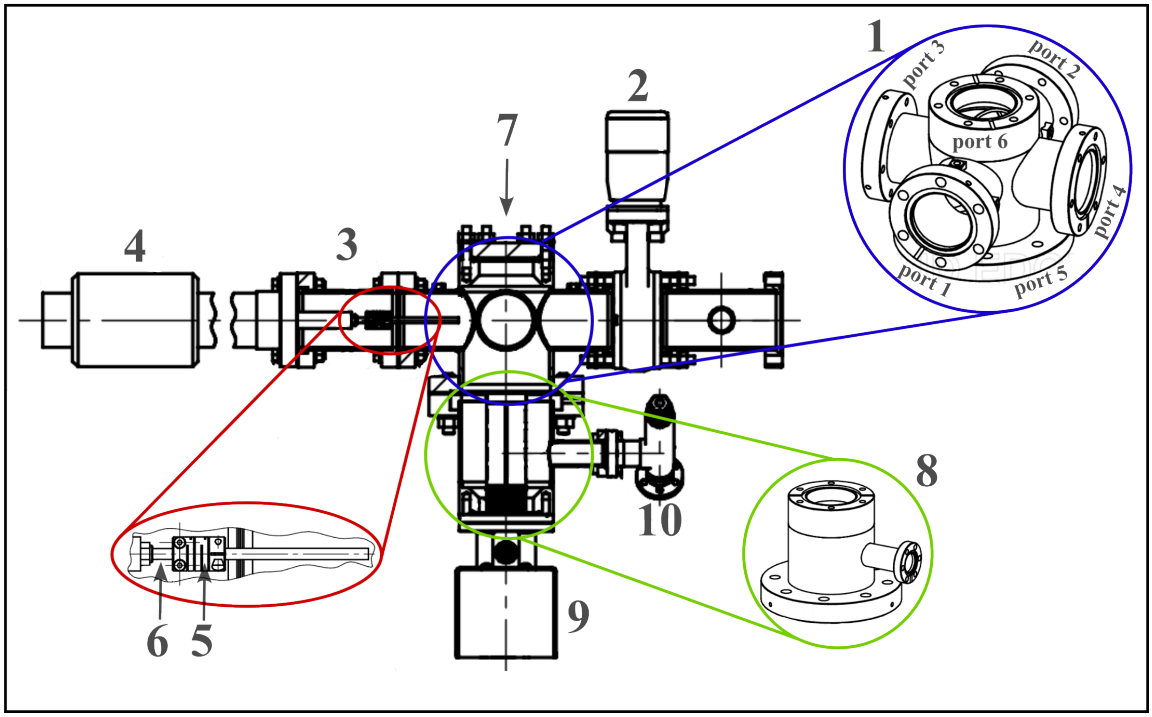

Figure 5.1: A: Picture of the UHV suitcase attached to the load-lock (0) of the THz-STM machine. B: Technical drawing of the UHV suitcase. 1: load-lock vessel with 6 ports (three ports are rotatable DN40CF flanges (port 1, 3 and 4), two ports are DN40CF flanges (port 2 and 6) and one port is a DN63CF flange (port 5)), 2: Mini UHV-Schieber, 3: spacer with two DN40CF flanges, 4: transfer rod, 5: sample holder tool, 6: adapter tool, 7: cold cathode gauge. Please note that the cold cathode gauge is not shown in the technical drawing on port 6. 8: Tee connector with three different sized flanges (rotatable DN63CF, DN40CF and DN16CF), 9: NEG/Ion Combination Pump, 10: angle valve, 11: post on the optical table.

Bibliography

[1] M. Bibes, J. Villegas, and A. Barthélémy. Ultrathin oxide films and interfaces for electronics and spintronics. *Adv. Phys.*, 60(1):5–84, 2011.

[2] T. Damen, S. Porto, and B. Tell. Raman Effect in Zinc Oxide. *Phys. Rev.*, 142(2): 570–574, 1966.

[3] J. Khler. Transition Metal Oxides. An Introduction to their Electronic Structure and Properties. *Angew. Chem.*, 105(3):477–477, 1993.

[4] D. Johnson. *Some thermodynamic aspects of inorganic chemistry*. Cambridge texts in chemistry and biochemistry. Cambridge University Press, Cambridge, 2nd edition, 1982.

[5] O. Sørensen, editor. *Nonstoichiometric Oxides*. Materials science and technology. Academic Press, New York, 1981.

[6] Ü. Özgür, I. Alivov, C. Liu, A. Teke, M. Reshchikov, S. Doğan, V. Avrutin, S.-J. Cho, and H. Morkoç. A comprehensive review of ZnO materials and devices. *J. Appl. Phys.*, 98(4):041301, 2005.

[7] D. Norton. Synthesis and properties of epitaxial electronic oxide thin-film materials. *Mater. Sci. Eng. R Rep.*, 43(5-6):139–247, 2004.

[8] H.-J. Freund. Metal-supported ultrathin oxide film systems as designable catalysts and catalyst supports. *Surf. Sci.*, 601(6):1438–1442, 2007.

[9] S. Schauermann, N. Nilius, S. Shaikhutdinov, and H.-J. Freund. Nanoparticles for Heterogeneous Catalysis: New Mechanistic Insights. *Acc. Chem. Res.*, 46(8):1673–1681, 2013.

[10] H.-J. Freund and G. Pacchioni. Oxide ultra-thin films on metals: new materials for the design of supported metal catalysts. *Chem. Soc. Rev.*, 37(10):2224, 2008.

[11] S. Shaikhutdinov and H.-J. Freund. Ultrathin Oxide Films on Metal Supports: Structure-Reactivity Relations. *Annu. Rev. Phys. Chem.*, 63(1):619–633, 2012.

[12] T. Kumagai, S. Liu, A. Shiotari, D. Baugh, S. Shaikhutdinov, and M. Wolf. Local electronic structure, work function, and line defect dynamics of ultrathin epitaxial ZnO layers on a Ag(111) surface. *J. Condens. Matter Phys.*, 28(49):494003, 2016.

[13] K. Nomura, H. Ohta, K. Ueda, T. Kamiya, M. Hirano, and H. Hosono. Thin-Film Transistor Fabricated in Single-Crystalline Transparent Oxide Semiconductor. *Science*, 300(5623):1269–1272, 2003.

[14] P. Mitra, A. Chatterjee, and H. Maiti. ZnO thin film sensor. *Mater. Lett.*, 35(1-2): 33–38, 1998.

[15] K. Ellmer, A. Klein, B. Rech, R. Hull, R. Osgood, J. Parisi, and H. Warlimont, editors. *Transparent Conductive Zinc Oxide: Basics and Applications in Thin Film Solar Cells*, volume 104 of *Springer Series in Materials Science*. Springer Berlin Heidelberg, Berlin, Heidelberg, 2008.

[16] Michael S. The role of zinc oxide in Cu/ZnO catalysts for methanol synthesis and the water−gas shift reaction. *Top. Catal.*, 8(3):259–266, 1999.

[17] H. Morkoç and Ü. Özgür. *Zinc oxide: fundamentals, materials and device technology*. Wiley-VCH, Weinheim, 2009.

[18] C. Jagadish and S. Pearton, editors. *Zinc oxide bulk, thin films and nanostructures: processing, properties and applications*. Elsevier, Amsterdam; Boston, 2006.

[19] R. Zhang, A. Ludviksson, and C. Campbell. The chemisorption of methanol on Cu films on ZnO$(000\bar{1})$-O. *Catal. Lett.*, 25(3-4):277–292, 1994.

[20] F. Shan, B. Kim, G. Liu, Z. Liu, J. Sohn, W. Lee, B. Shin, and Y. Yu. Blueshift of near band edge emission in Mg doped ZnO thin films and aging. *J. Appl. Phys.*, 95 (9):4772–4776, 2004.

[21] A. Gloystein and N. Nilius. Luminescence from Cuprous Oxide in a Scanning Tunneling Microscope: Competition between Plasmonic and Excitonic Response. *ACS Photonics*, 9(11):3625–3632, 2022.

[22] G. Binnig, K. Frank, H. Fuchs, N. Garcia, B. Reihl, H. Rohrer, F. Salvan, and A. Williams. Tunneling Spectroscopy and Inverse Photoemission: Image and Field States. *Phys. Rev. Lett.*, 55(9):991–994, 1985.

[23] G. Binnig, H. Rohrer, C. Gerber, and E. Weibel. Surface Studies by Scanning Tunneling Microscopy. *Phys. Rev. Lett.*, 49(1):57–61, 1982.

[24] G. Binnig and H. Rohrer. Scanning tunneling microscopy-from birth to adolescence. *Rev. Mod. Phys.*, 59(3):615–625, 1987.

[25] Y. Kuk and P. Silverman. Scanning tunneling microscope instrumentation. *Rev. Sci. Instrum.*, 60(2):165–180, 1989.

[26] J. Stroscio, R. Feenstra, and A. Fein. Electronic Structure of the Si(111)2 x 1 Surface by Scanning-Tunneling Microscopy. *Phys. Rev. Lett.*, 57(20):2579–2582, 1986.

[27] Y. Zhang, Q. Meng, L. Zhang, Y. Luo, Y. Yu, B. Yang, Y. Zhang, R. Esteban, J. Aizpurua, Y. Luo, J. Yang, Z. Dong, and J. Hou. Sub-nanometre control of the coherent interaction between a single molecule and a plasmonic nanocavity. *Nat. Commun.*, 8(1):15225, 2017.

[28] B. Doppagne, M. Chong, H. Bulou, A. Boeglin, F. Scheurer, and G. Schull. Electrofluorochromism at the single-molecule level. *Science*, 361(6399):251–255, 2018.

[29] F. Stavale, N. Nilius, and H.-J. Freund. STM Luminescence Spectroscopy of Intrinsic Defects in ZnO($000\bar{1}$) Thin Films. *J. Phys. Chem. Lett.*, 4(22):3972–3976, 2013.

[30] N. Krane, C. Lotze, J. Läger, G. Reecht, and K. Franke. Electronic Structure and Luminescence of Quasi-Freestanding MoS_2 Nanopatches on Au(111). *Nano Lett.*, 16 (8):5163–5168, 2016.

[31] S. Liu, M. Wolf, and T. Kumagai. Plasmon-assisted resonant electron tunneling in a scanning tunneling microscope junction. *Phys. Rev. Lett.*, 121(22):226802, 2018.

[32] R. Péchou, S. Jia, J. Rigor, O. Guillermet, G. Seine, J. Lou, N. Large, A. Mlayah, and R. Coratger. Plasmonic-Induced Luminescence of $MoSe_2$ Monolayers in a Scanning Tunneling Microscope. *ACS Photonics*, 7(11):3061–3070, 2020.

[33] X. Qiu, G. Nazin, and W. Ho. Vibrationally Resolved Fluorescence Excited with Submolecular Precision. *Science*, 299(5606):542–546, 2003.

[34] B. Doppagne, M. Chong, E. Lorchat, S. Berciaud, M. Romeo, H. Bulou, A. Boeglin, F. Scheurer, and G. Schull. Vibronic Spectroscopy with Submolecular Resolution from STM-Induced Electroluminescence. *Phys. Rev. Lett.*, 118(12):127401, 2017.

[35] Y. Zhang, Y. Luo, Y. Yu, Y. Kuang, L. Zhang, Q. Meng, Y. Luo, J. Yang, Z. Dong, and J. Hou. Visualizing coherent intermolecular dipole−dipole coupling in real space. *Nature*, 531(7596):623–627, 2016.

[36] H. Imada, K. Miwa, M. Imai-Imada, S. Kawahara, K. Kimura, and Y. Kim. Real-space investigation of energy transfer in heterogeneous molecular dimers. *Nature*, 538(7625): 364–367, 2016.

[37] H. Imada, K. Miwa, M. Imai-Imada, S. Kawahara, K. Kimura, and Y. Kim. Single-Molecule Investigation of Energy Dynamics in a Coupled Plasmon-Exciton System. *Phys. Rev. Lett.*, 119(1):013901, 2017.

[38] H. Kourouklis and R. Nix. The growth and structure of ZnO_x overlayers on low index silver surfaces. *Surf. Sci.*, 318(1-2):104–114, 1994.

[39] Q. Pan, B. Liu, M. McBriarty, Y. Martynova, I. Groot, S. Wang, M. Bedzyk, S. Shaikhutdinov, and H.-J. Freund. Reactivity of Ultra-Thin ZnO Films Supported by Ag(111) and Cu(111): A Comparison to ZnO/Pt(111). *Catal. Lett.*, 144(4):648–655, 2014.

[40] A. Shiotari, B. Liu, S. Jaekel, L. Grill, S. Shaikhutdinov, H.-J. Freund, M. Wolf, and T. Kumagai. Local characterization of Ultrathin ZnO Layers on Ag(111) by Scanning Tunneling Microscopy and Atomic Force Microscopy. *J. Phys. Chem. C*, 118(47): 27428–27435, 2014.

[41] C. Tusche, H. Meyerheim, and J. Kirschner. Observation of Depolarized ZnO(0001) Monolayers: Formation of Unreconstructed Planar Sheets. *Phys. Rev. Lett.*, 99(2): 026102, 2007.

[42] S. Liu, M. Müller, Y. Sun, I. Hamada, A. Hammud, M. Wolf, and T. Kumagai. Resolving the Correlation between Tip-Enhanced Resonance Raman Scattering and Local Electronic States with 1 nm Resolution. *Nano Lett.*, 19(8):5725–5731, 2019.

[43] S Liu, A. Hammud, I. Hamada, M. Wolf, M. Müller, and T. Kumagai. Nanoscale coherent phonon spectroscopy. *Sci. Adv.*, 8(42):eabq5682, 2022.

[44] S. Liu, M. Wolf, and T. Kumagai. Nanoscale Heating of an Ultrathin Oxide Film Studied by Tip-Enhanced Raman Spectroscopy. *Phys. Rev. Lett.*, 128(20):206803, 2022.

[45] J. Kröger, B. Doppagne, F. Scheurer, and G. Schull. Fano Description of Single-Hydrocarbon Fluorescence Excited by a Scanning Tunneling Microscope. *Nano Lett.*, 18(6):3407–3413, 2018.

[46] F. Moresco. Local information with scanning tunneling microscopy. In M. Rocca, T. Rahman, and L. Vattuone, editors, *Springer Handbook of Surface Science*, pages 225–241. Springer International Publishing, Cham, 2020.

[47] A. Pia and G. Costantini. Scanning Tunneling Microscopy. In B. Bhushan, editor, *Encyclopedia of Nanotechnology*, pages 2301–2313. Springer Netherlands, Dordrecht, 2012.

[48] N. Lorente, M. Persson, L. Lauhon, and W. Ho. Symmetry Selection Rules for Vibrationally Inelastic Tunneling. *Phys. Rev. Lett.*, 86(12):2593–2596, 2001.

[49] J. Chen. *Introduction to scanning tunneling microscopy.* Number 4 in Oxford series in optical and imaging sciences. Oxford University Press, New York, 1993.

[50] J. Coombs, M. Welland, and J. Pethica. Experimental barrier heights and the image potential in scanning tunneling microscopy. *Surf. Sci.*, 198(3):L353–L358, 1988.

[51] J. Bardeen. Tunnelling from a Many-Particle Point of View. *Phys. Rev. Lett.*, 6(2): 57–59, 1961.

[52] J. Tersoff and D. Hamann. Theory and Application for the Scanning Tunneling Microscope. *Phys. Rev. Lett.*, 50(25):1998–2001, 1983.

[53] J. Tersoff and D. R. Hamann. Theory of the scanning tunneling microscope. 31(2): 805–813, 1985.

[54] A. Vázquez de Parga and R. Miranda. Scanning Tunneling Spectroscopy. In B. Bhushan, editor, *Encyclopedia of Nanotechnology*, pages 2313–2321. Springer Netherlands, Dordrecht, 2012.

[55] B. Stipe, M. Rezaei, and W. Ho. Single-Molecule Vibrational Spectroscopy and Microscopy. *Science*, 280(5370):1732–1735, 1998.

[56] B. Stipe, M. Rezaei, and W. Ho. Localization of Inelastic Tunneling and the Determination of Atomic-Scale Structure with Chemical Specificity. *Phys. Rev. Lett.*, 82(8): 1724–1727, 1999.

[57] J. Lambe and S. McCarthy. Light Emission from Inelastic Electron Tunneling. *Phys. Rev. Lett.*, 37(14):923–925, 1976.

[58] J. Gimzewski, B. Reihl, J. Coombs, and R. Schlittler. Photon emission with the scanning tunneling microscope. *Z. Phys. B: Condens. Matter*, 72(4):497–501, 1988-12.

[59] J. Martínez-Blanco and S. Fölsch. Light emission from Ag(111) driven by inelastic tunneling in the field emission regime. *J. Condens. Matter Phys.*, 27(25):255008, 2015.

[60] F. Rossel, M. Pivetta, and W. Schneider. Luminescence experiments on supported molecules with the scanning tunneling microscope. *Surf. Sci. Rep.*, 65(5):129–144, 2010.

[61] L. Parra Lopez. *Tailoring the luminescence of atomically-thin semiconductors at the sub-nanometer scale.* PhD Thesis, Université de Strabourg, 2021.

[62] B. Schuler, K. Cochrane, C. Kastl, E. Barnard, E. Wong, N. Borys, A. Schwartzberg, D. Ogletree, F. García de Abajo, and A. Weber-Bargioni. Electrically driven photon emission from individual atomic defects in monolayer WS_2. *Sci. Adv.*, 6(38):eabb5988, 2020.

[63] D. Pommier, R. Bretel, L. López, F. Fabre, A. Mayne, E. Boer-Duchemin, G. Dujardin, G. Schull, S. Berciaud, and E. Le Moal. Scanning Tunneling Microscope-Induced Excitonic Luminescence of a Two-Dimensional Semiconductor. *Phys. Rev. Lett.*, 123 (2):027402, 2019.

[64] R. Peña Román, Y. Auad, L. Grasso, F. Alvarez, I. Barcelos, and L. Zagonel. Tunneling-current-induced local excitonic luminescence in p-doped WSe $_2$ monolayers. *Nanoscale*, 12(25):13460–13470, 2020.

[65] B. Pettinger, P. Schambach, C. Villagómez, and N. Scott. Tip-Enhanced Raman Spectroscopy: Near-Fields Acting on a Few Molecules. *Annu. Rev. Phys. Chem.*, 63 (1):379–399, 2012.

[66] E. Purcell. Spontaneous Emission Probabilities at Radio Frequencies. *Phys. Rev.*, 69 (11-12):681, 1946.

[67] W. Davey. Precision Measurements of the Lattice Constants of Twelve Common Metals. *Phys. Rev.*, 25(6):753–761, 1925.

[68] G. Fuster, J. M. Tyler, N. Brener, J. Callaway, and D. Bagayoko. Electronic structure and related properties of silver. *Phys. Rev. B*, 42(12):7322–7329, 1990.

[69] M. Chelvayohan and C. Mee. Work function measurements on (110), (100) and (111) surfaces of silver. *J. Phys. Condens. Matter*, 15(10):2305–2312, 1982.

[70] B. Cooper, H. Ehrenreich, and H. Philipp. Optical Properties of Noble Metals. II. *Phys. Rev.*, 138(2A):A494–A507, 1965.

[71] P. Johnson and R. Christy. Optical Constants of the Noble Metals. *Phys. Rev. B*, 6 (12):4370–4379, 1972.

[72] A. Maradudin, J. Sambles, and W. Barnes. *Modern plasmonics*. Number 4 in Handbook of surface science. Elsevier, Amsterdam Oxford Waltham, 2014.

[73] H. Böckmann, S. Liu, M. Müller, A. Hammud, M. Wolf, and T. Kumagai. Near-Field Manipulation in a Scanning Tunneling Microscope Junction with Plasmonic Fabry-Pérot Tips. *Nano Lett.*, 19(6):3597–3602, 2019.

[74] R. Rendell, D. Scalapino, and B. Mühlschlegel. Role of Local Plasmon Modes in Light Emission from Small-particle Tunnel Junctions. *Phys. Rev. Lett.*, 41(25):1746–1750, 1978.

[75] J. Aizpurua, S. Apell, and R. Berndt. Role of tip shape in light emission from the scanning tunneling microscope. *Phys. Rev. B*, 62(3):2065–2073, 2000.

[76] R. Berndt, J. Gimzewski, and P. Johansson. Inelastic tunneling excitation of tip-induced plasmon modes on noble-metal surfaces. *Phys. Rev. Lett.*, 67(27):3796–3799, 1991.

[77] T. Rojalin, B. Phong, H. Koster, and R. Carney. Nanoplasmonic Approaches for Sensitive Detection and Molecular Characterization of Extracellular Vesicles. *Front. Chem.*, 7:279, 2019.

[78] S. Kühn, U. Håkanson, L. Rogobete, and V. Sandoghdar. Enhancement of Single-Molecule Fluorescence Using a Gold Nanoparticle as an Optical Nanoantenna. *Phys. Rev. Lett.*, 97(1):017402, 2006.

[79] P. Anger, P. Bharadwaj, and L. Novotny. Enhancement and Quenching of Single-Molecule Fluorescence. *Phys. Rev. Lett.*, 96(11):113002, 2006.

[80] P. Bharadwaj, B. Deutsch, and L. Novotny. Optical Antennas. *Adv. Opt. Photonics*, 1(3):438–483, 2009.

[81] W. Barnes. Fluorescence near interfaces: The role of photonic mode density. *J. Mod. Opt.*, 45(4):661–699, 1998.

[82] J Goniakowski, F. Finocchi, and C. Noguera. Polarity of oxide surfaces and nanostructures. *Rep. Prog. Phys.*, 71(1):016501, 2008.

[83] C. Freeman, F. Claeyssens, N. Allan, and J. Harding. Graphitic Nanofilms as Precursors to Wurtzite Films. *Phys. Rev. Lett.*, 96(6):066102, 2006.

[84] X. Deng, K. Yao, K. Sun, W.-X. Li, J. Lee, and C. Matranga. Growth of Single- and Bilayer ZnO on Au(111) and Interaction with Copper. *J. Phys. Chem. C*, 117(21): 11211–11218, 2013.

[85] F. Stavale, L. Pascua, N. Nilius, and H.-J. Freund. Morphology and Luminescence of ZnO Films Grown on a Au(111) Support. *J. Phys. Chem. C*, 117(20):10552–10557, 2013.

[86] J. Li, W. Schneider, R. Berndt, O. Bryant, and S. Crampin. Surface-State Lifetime Measured by Scanning Tunneling Spectroscopy. *Phys. Rev. Lett.*, 81(20):4464–4467, 1998.

[87] L. Giordano, F. Cinquini, and G. Pacchioni. Tuning the surface metal work function by deposition of ultrathin oxide films: Density functional calculations. *Phys. Rev. B*, 73(4):045414, 2006.

[88] S. Liu. *Development of Low-Temperature Photon Scanning Probe Microscopy and Nanoscale Characterization of Ultrathin ZnO Layers on Ag(111).* PhD Thesis, FU Berlin, 2019.

[89] R. Shantyr, C. Hagendorf, and H. Neddermeyer. Scanning tunneling microscopy and spectroscopy studies on structural and electronic properties of thin films of Co oxides and oxide precursor states on Ag(001). *Thin Solid Films*, 464-465:65–75, 2004.

[90] I. Sebastian and H. Neddermeyer. Scanning tunneling microscopy on the atomic and electronic structure of CoO thin films on ag(100). *Surf. Sci.*, 454-456:771–777, 2000.

[91] J. Mooney and P. Kambhampati. Get the Basics Right: Jacobian Conversion of Wavelength and Energy Scales for Quantitative Analysis of Emission Spectra. *J. Phys. Chem. Lett.*, 4(19):3316–3318, 2013.

[92] A. Strózecka, J. Li, R. Schürmann, G. Schulze, M. Corso, F. Schulz, C. Lotze, S. Sadewasser, K. Franke, and J. Pascual. Electroluminescence of copper-nitride nanocrystals. *Phys. Rev. B*, 90(19):195420, 2014.

[93] A Martín-Jiménez, A. Fernández-Domínguez, K. Lauwaet, D. Granados, R. Miranda, F. García-Vidal, and R. Otero. Unveiling the radiative local density of optical states of a plasmonic nanocavity by STM. *Nat. Commun.*, 11(1):1021, 2020.

[94] P. Johansson, R. Monreal, and P. Apell. Theory for light emission from a scanning tunneling microscope. *Phys. Rev. B*, 42(14):9210–9213, 1990.

[95] S. Liu, B. Cirera, Y. Sun, I. Hamada, M. Müller, A. Hammud, M. Wolf, and T. Kumagai. Dramatic Enhancement of Tip-Enhanced Raman Scattering Mediated by Atomic Point Contact Formation. *Nano Lett.*, 20(8):5879–5884, 2020.

[96] W. Zhu, R. Esteban, A. Borisov, J. Baumberg, P. Nordlander, H. Lezec, J. Aizpurua, and K. Crozier. Quantum mechanical effects in plasmonic structures with subnanometre gaps. *Nat. Commun.*, 7(1):11495, 2016.

[97] K. Kuhnke, C. Große, P. Merino, and K. Kern. Atomic-Scale Imaging and Spectroscopy of Electroluminescence at Molecular Interfaces. *Chem. Rev.*, 117(7):5174–5222, 2017.

[98] C. Große, P. Merino, A. Roslawska, O. Gunnarsson, K. Kuhnke, and K. Kern. Submolecular Electroluminescence Mapping of Organic Semiconductors. *ACS Nano*, 11(2):1230–1237, 2017.

[99] C. Harris, N. Ge, R. Lingle, J. McNeill, and C. Wong. Femtosecond Dynamics of Electrons on Surfaces and at Interfaces. *Annu. Rev. Phys. Chem.*, 48(1):711–744, 1997.

[100] K. Schubert, A. Damm, S. Eremeev, M. Marks, M. Shibuta, W. Berthold, J. Güdde, A. Borisov, S. Tsirkin, E. Chulkov, and U. Höfer. Momentum-resolved electron dynamics of image-potential states on Cu and Ag surfaces. *Phys. Rev. B*, 85(20): 205431, 2012.

[101] S. Liu, A. Shiotari, D. Baugh, M. Wolf, and T. Kumagai. Enhanced resolution imaging of ultrathin ZnO layers on Ag(111) by multiple hydrogen molecules in a scanning tunneling microscope junction. *Phys. Rev. B*, 97(19):195417, 2018.

[102] SAES Group. NEXTorr© UHV pumps. URL `www.saesgroup.com`.

[103] T. Madey and J. Yates. Electron-Stimulated Desorption as a Tool for Studies of Chemisorption: A Review. *J. Vac. Sci. Technol.*, 8(4):525–555, 1971.

7 Appendix

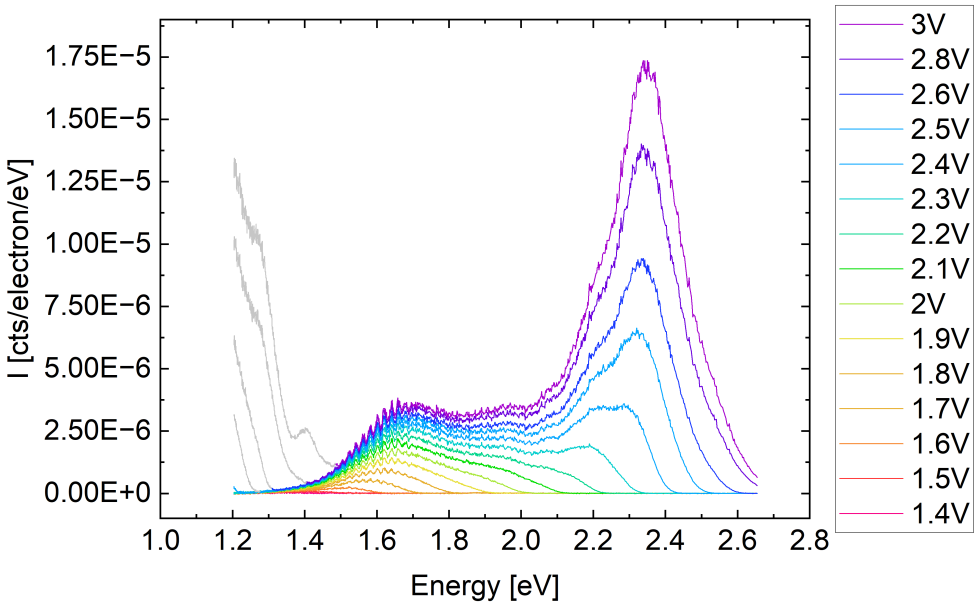

Figure 7.1: Line spectra of the bias-dependent STML spectra (I [cts/electron/eV]) of the Ag(111)-Ag tip junction in constant current mode at 3 nA.

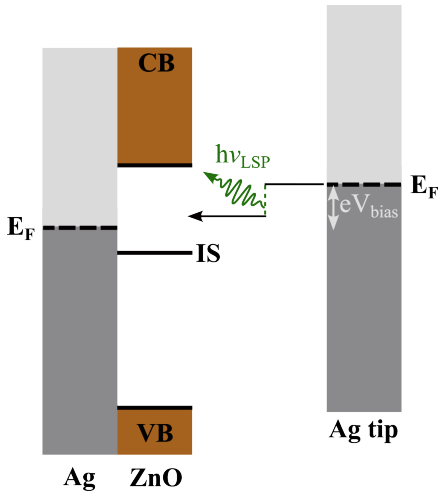

Figure 7.2: Schematic energy diagram of the ZnO/Ag(111)-Ag tip junction at positive bias voltage below the CBE of ZnO. Inelastic tunneling inside the band gap excites LSP of the junction which radiatively decays.

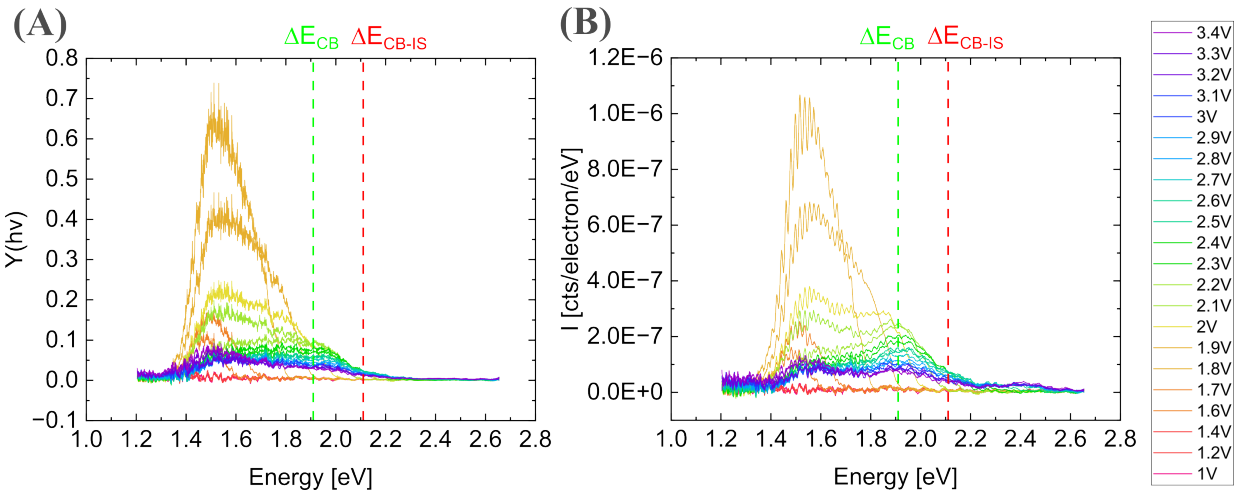

Figure 7.3: Line spectra of the bias-dependent STML spectra as relative photon yield $Y(h\nu)$ (A) and as intensity only normalized to the electron number (B) on 2 ML ZnO in constant current mode at 8 nA at positive bias voltage. The CBE-IS transition energy (light green dashed line) and the CBE energy relative to Fermi level (red dashed line) are marked.

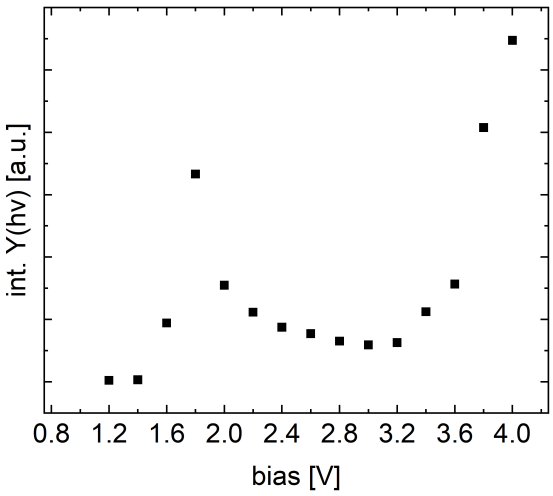

Figure 7.4: Integrated intensity of $Y(h\nu)$ as a function of the bias voltage on 2 ML ZnO.

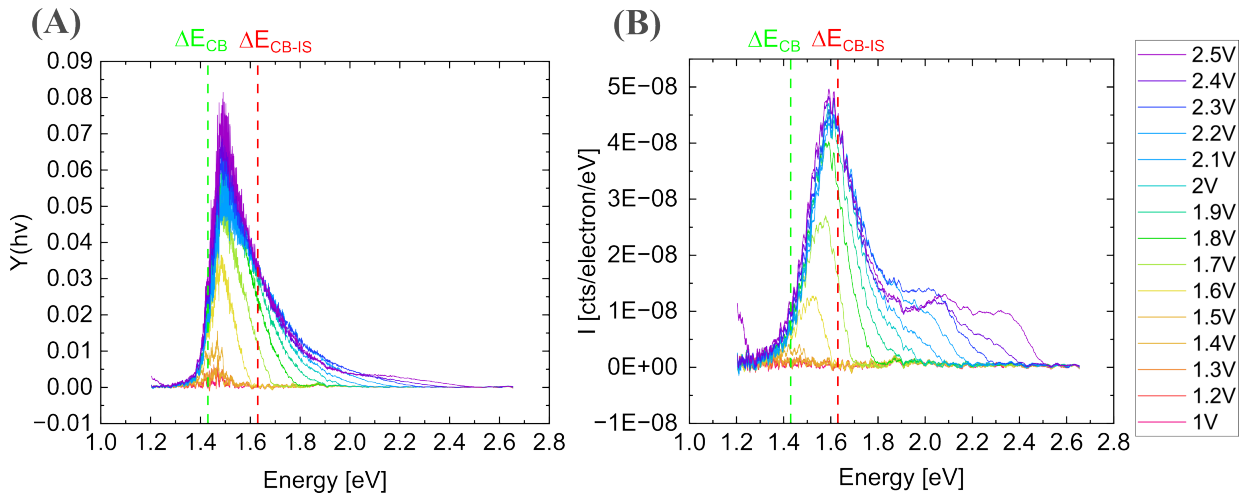

Figure 7.5: Line spectra of the bias-dependent STML spectra as relative photon yield $Y(h\nu)$ (A) and as intensity only normalized to the electron number (B) on 3 ML ZnO in constant current mode at 50 nA at positive bias voltage. The CBE-IS transition energy (light green dashed line) and the CBE energy relative to Fermi level (red dashed line) are marked.

Destruction of ZnO islands

At higher bias voltages, it has been observed that the moiré pattern of 2 ML and 3 ML ZnO islands is destroyed and that the electronic structure is altered. Fig. 7.6 and 7.7 show an exemplary progress of the destruction of the moiré pattern of a 2 ML and 3 ML ZnO island, respectively, during the bias-dependent measurement after certain bias voltages at a tunneling current of 8 nA. The moiré pattern on 3 ML ZnO is completely destroyed in-between 2.6 V and 2.9 V while on 2 ML ZnO, the moiré pattern is only partially destroyed after measuring at 3.4 V. However, the destruction also depends on the tunneling current and the exposure time when a certain bias voltage threshold is exceeded. In comparison to the 2 ML ZnO islands, the 3 ML islands are much more fragile and easier destroyed probably because the 3 ML ZnO islands are more inhomogeneous and exhibit a surface dipole moment.[83, 41] The observed alternation of the electronic structure is most likely caused by the electron bombardment and local heating which induces defects inside the ultra-thin ZnO films. Interestingly, positions deviating from the tip position were also destroyed. Electron-stimulated desorption is a surface science technique, which is based on the bombardment with low-energy electrons causing desorption, bond alternation and decomposition.[103] Liu et al. concluded that efficient local heating occurs on 2 ML ZnO via resonant electron tunneling into the CB and subsequent electron-phonon coupling.[44] Kumagai et al. did not observe any destruction of the ZnO films at 5 K even though they measured STS spectra up to a bias voltage of 8 V.[12] The deviation of the moiré pattern periodicity (see Fig. 3.5, Experimental Part) from their observations might be an indication that a different coincidence structure was prepared in this thesis.[40] According to Shiotari et al., the ZnO(0001)-(7x7)/Ag(111)-(8x8) coincidence structure is thermodynamically more stable than the ZnO(0001)-(5x5)/Ag(111)-($3\sqrt{3}$x$3\sqrt{3}$) R30° coincidence structure, which forms smaller domains.[40] Thus, measurements in the future will be conducted on larger and more stable ZnO films. In order to exclude any effects of degradation, future bias-dependent STML measurements will be conducted in a forward and backward fashion with STS spectra or maps taken in-between.

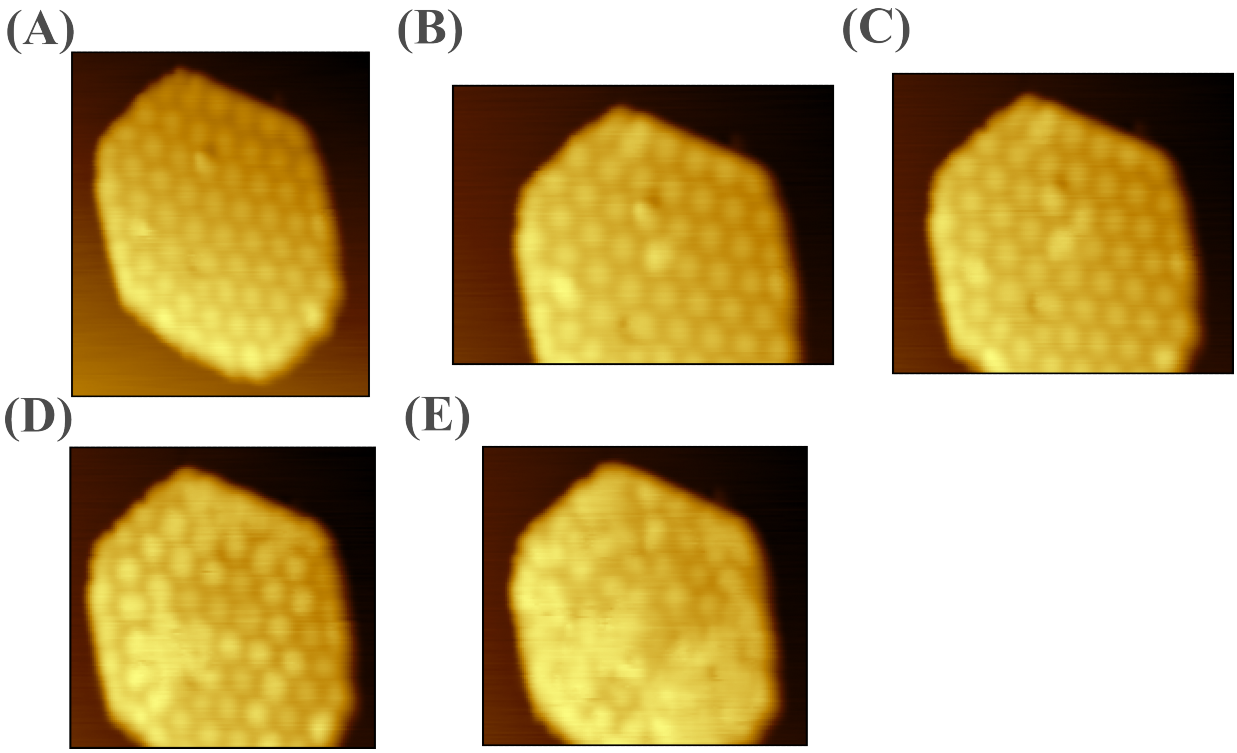

Figure 7.6: STM images ($V_{\text{bias}} = 1\,\text{V}$, $I_{\text{t}} = 100\,\text{pA}$) of a 2 ML ZnO island during a bias-dependent measurement at 8 nA before (A), after 2.1 V (B), after 2.6 V (C), after 3.1 V (D) and after 3.4 V (E). The moiré pattern changes and is partially destroyed with increasing bias voltage.

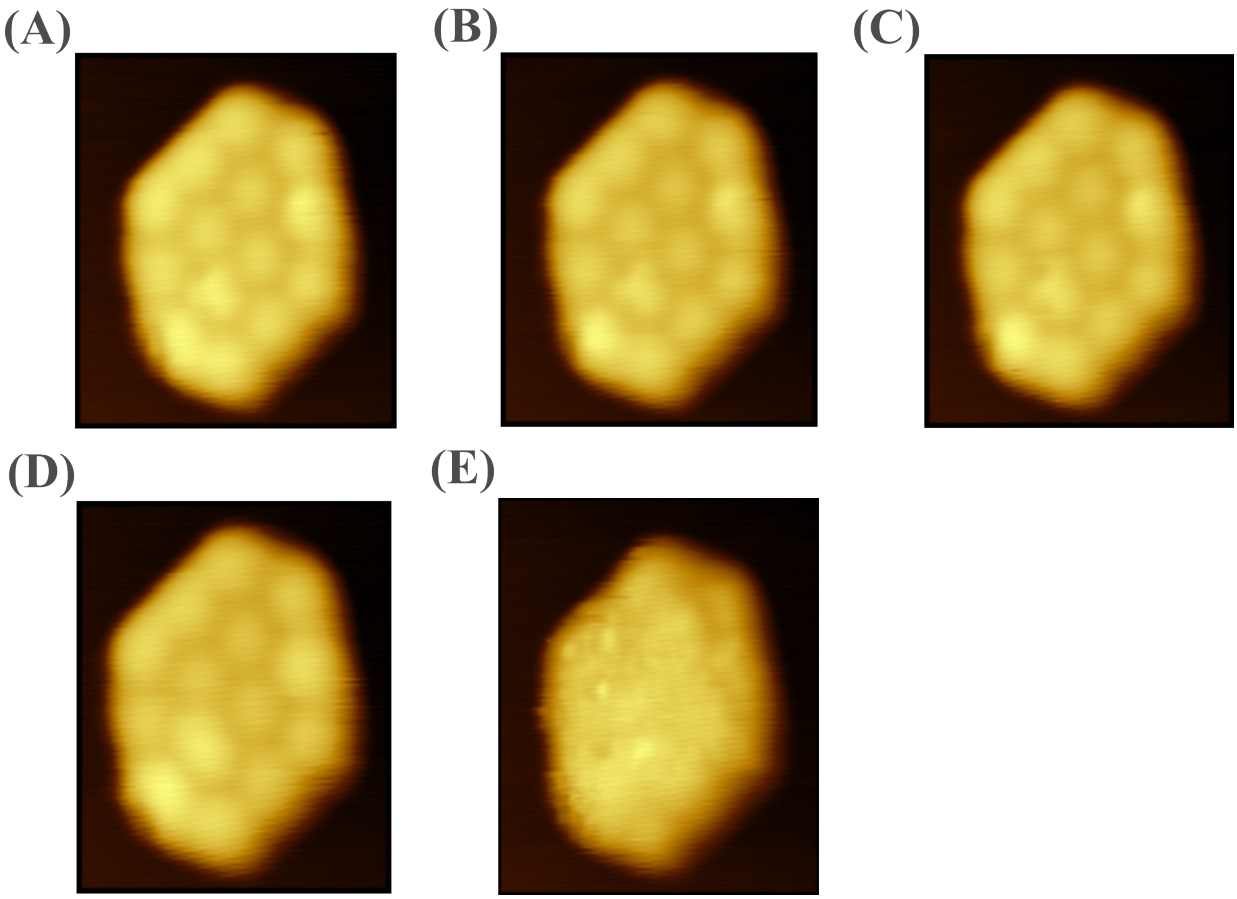

Figure 7.7: STM images ($V_{\text{bias}} = 1\,\text{V}$, $I_{\text{t}} = 100\,\text{pA}$) of a 3 ML ZnO island during a bias-dependent measurement at 8 nA before (A), after 1.5 V (B), after 2 V (C), after 2.5 V (D) and after 2.9 V (E). The moiré pattern changes and is partially destroyed with increasing bias voltage.

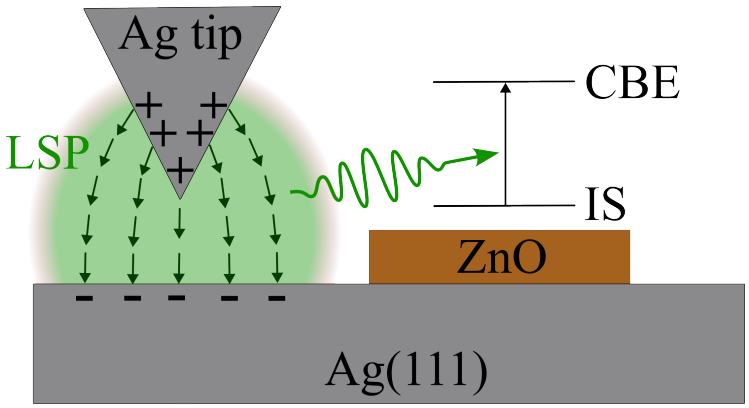

Figure 7.8: Schematic drawing of the Ag tip-Ag(111) surface junction and quenching of the LSP of the junction via energy transfer. A lateral distance-dependent STML response in close proximity to the ZnO island is expected.

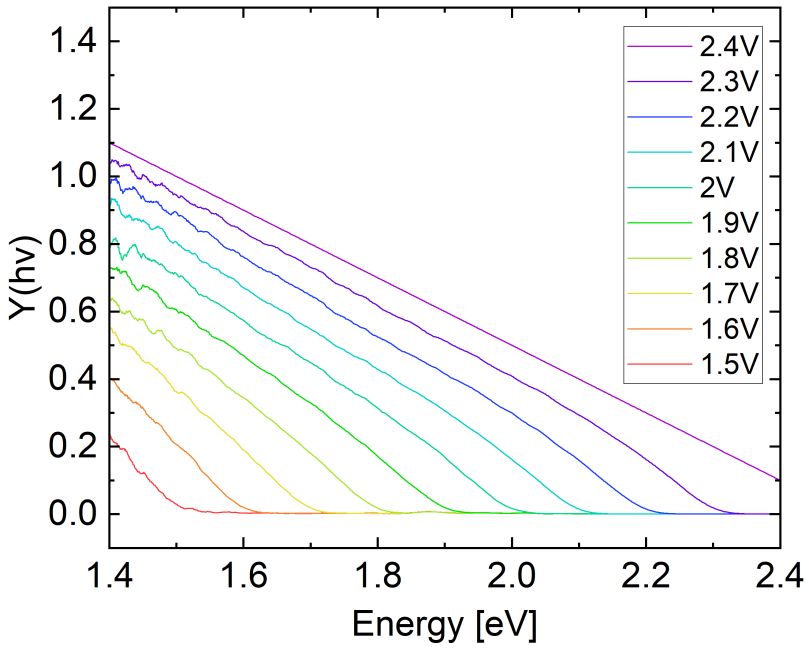

Figure 7.9: $Y(h\nu)$ of the the plasmonic response from the Ag(111)-Ag tip junction in constant current mode $I_\mathrm{t} = 3\,\mathrm{nA}$. $Y(h\nu)$ decreases proportional to $(eV_\mathrm{bias} - h\nu)$.

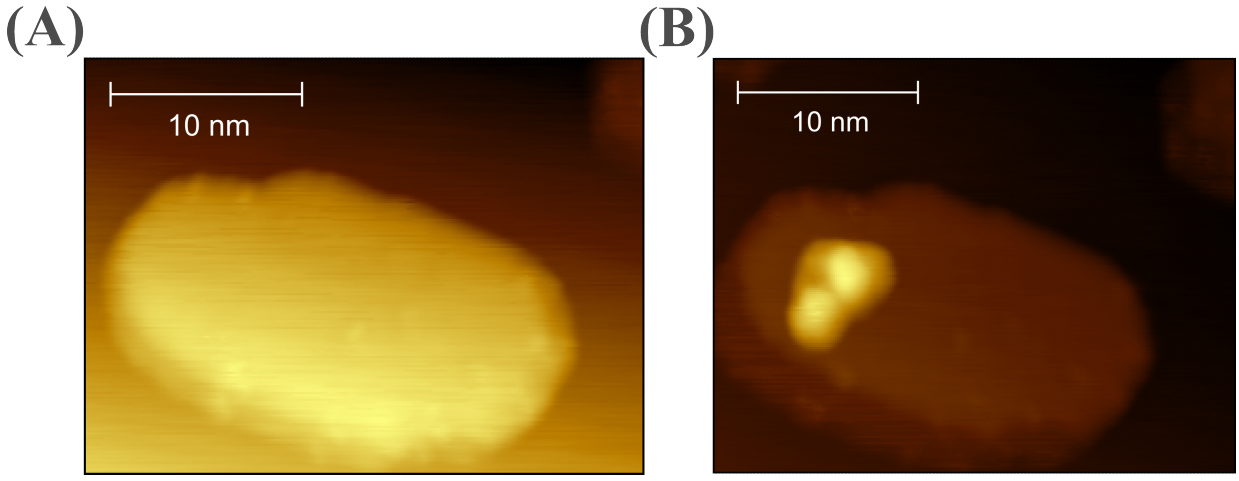

Figure 7.10: STM images ($V_\mathrm{bias} = -1\,\mathrm{V}$, $I_\mathrm{t} = 100\,\mathrm{pA}$) of a 2 ML ZnO island before (A) and after (B) the bias-dependent measurement with the lowest bias voltage at $-2.7\,\mathrm{V}$ and $5\,\mathrm{nA}$.

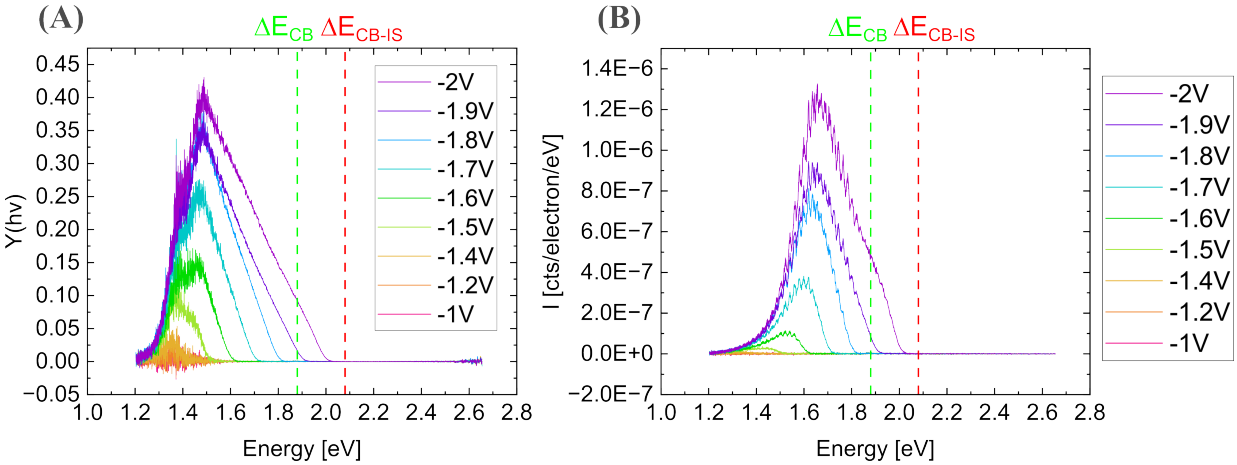

Figure 7.11: Line spectra of the bias-dependent STML spectra as relative photon yield $Y(h\nu)$ (A) and as intensity only normalized to the electron number (B) on 2 ML ZnO in constant current mode at 40 nA at negative bias voltage. The CBE-IS transition energy (light green dashed line) and the CBE energy relative to Fermi level (red dashed line) are marked.

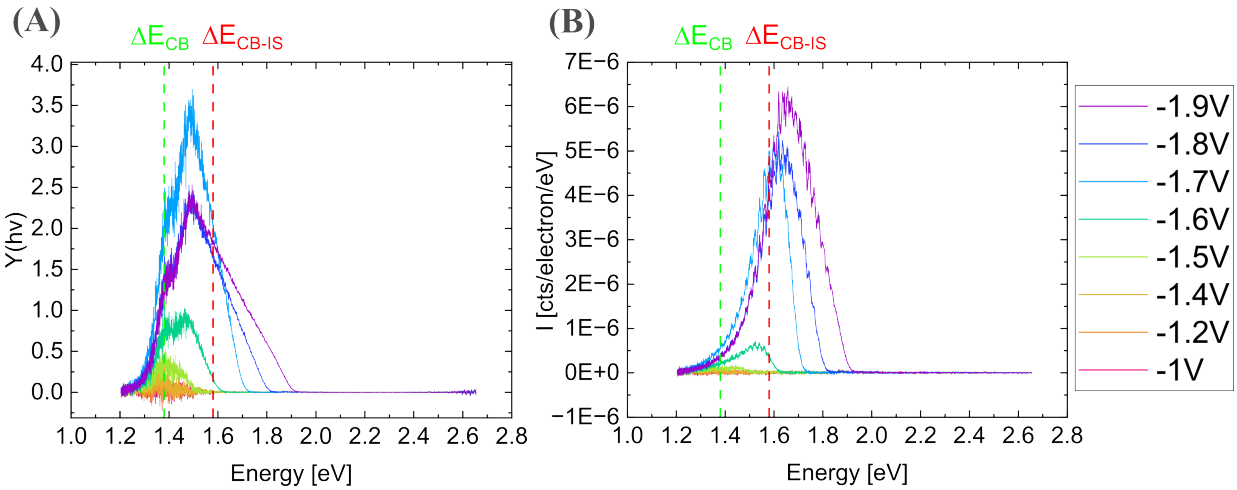

Figure 7.12: Line spectra of the bias-dependent STML spectra as relative photon yield $Y(h\nu)$ (A) and as intensity only normalized to the electron number (B) on 3 ML ZnO in constant current mode at 40 nA at negative bias voltage. The CBE-IS transition energy (light green dashed line) and the CBE energy relative to Fermi level (red dashed line) are marked.

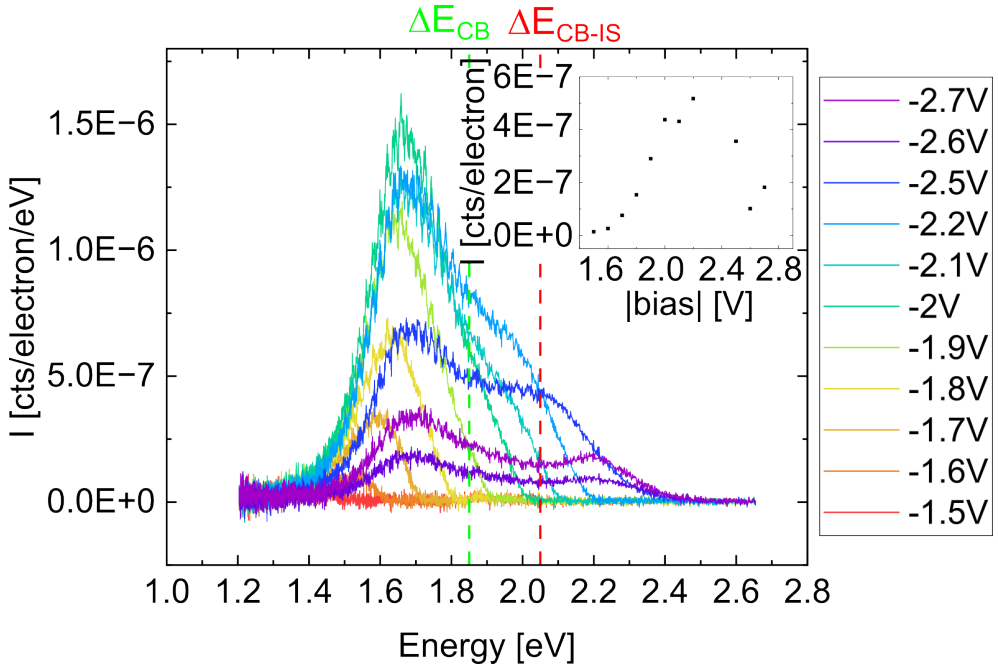

Figure 7.13: Bias-dependent STML spectra on 2 ML ZnO at negative bias voltage in constant current mode at 5 nA. The CBE-IS transition energy (light green dashed line) and the CBE energy relative to Fermi level (red dashed line) are marked. The condition of the ZnO/Ag(111)-Ag tip junction changed below a bias voltage of −2 V. Inset shows the integrated intensity.

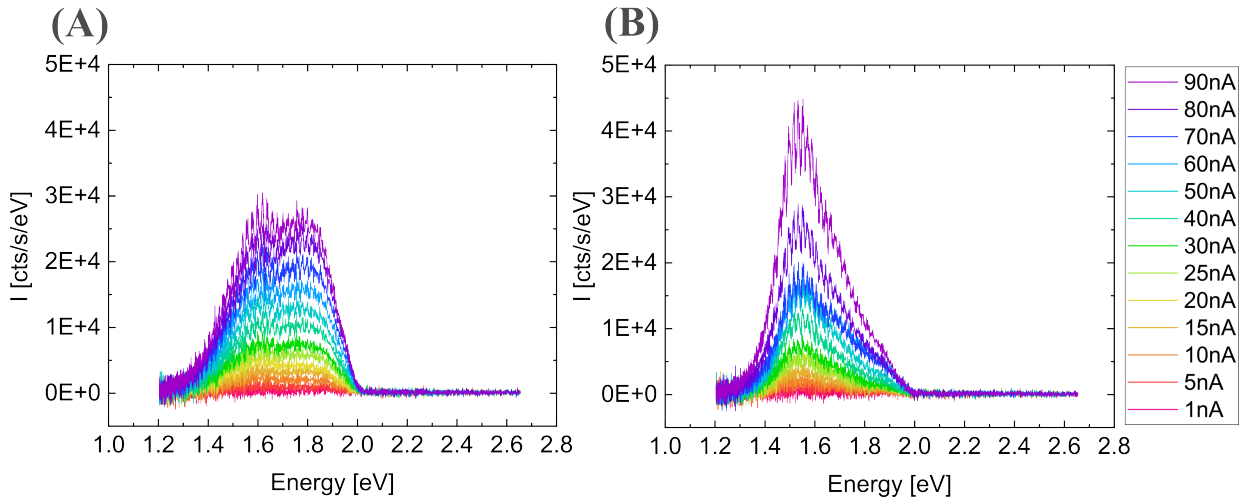

Figure 7.14: The STML response on 2 ML (A) and 3 ML (B) ZnO dependent on the tunneling current (1 nA to 90 nA) at a constant bias voltage of 2 V. Note that the counts are merely normalized to the integration time.

Acknowledgments

First of all, I would like to thank Prof. Dr. Martin Wolf and Prof. Dr. Thomas Risse as supervisors who reviewed this master thesis. I am grateful to Prof. Dr. Martin Wolf for letting me write this master thesis in his department and to Prof. Dr. Thomas Risse for his expertly advise. A special thanks belong to the group leader Dr. Melanie Müller for her ideas, mentorship, introduction to the experiment and LT-STM setup as well as her feedback on the thesis and her willingness to answer my questions.

I would like to express my gratitude to Dr. Akitoshi Shiotari and Dr. Youngwook Park for introducing me to the LT-STM setup and their support during the experiments. I would also like to thank Dr. Luis Parra López for his help setting up the spectrometer and his patience in discussions regarding scientific results and physics in general.

I want to thank all members of Melanie's research group (Luis, Vivien and Alkisti) for the great atmosphere and discussions during lunch break.

Des Weiteren möchte ich mich bei Holger Oertel für die Planung und Konstruktion der UHV suitcase bedanken. Besonderer Dank gilt Sven Kubala, unter dessen Anweisungen ich die UHV suitcase zusammengebaut habe, und Oscar Radke für die Hilfe beim Zusammenbauen. Außerdem möchte ich Harald Kirsch für die schnelle Anfertigung von geätzten Au-Spitzen danken.

Den zahlreichen Studierenden, die ich in den letzten eineinhalb Jahren in den Tutorien der Chemischen Thermodynamik begleiten durfte, möchte ich für die angenehme Abwechselung und die Diskussionen danken. Ich werde die Lehre an der Freien Universität Berlin vermissen.

Ich bin meinem Vater und meiner Mutter für die finanzielle Unterstützung während des gesamten Studiums unglaublich dankbar. Besonderer Dank gilt meiner lieben Mutter für ihre Fürsorge. Luise und Daniel danke ich für das Gegenlesen der Arbeit. Der allergrößte Dank geht an meine bessere Hälfte und Lebensgefährtin Luise für die schöne Zeit und

Geborgenheit. Zuallerletzt danke ich Opa Helmut für sein aufrichtiges Interesse und die schönen Gespräche, die ich sehr vermisse.

Statutory declaration

I hereby declare that I have written the present report independently. I have not used other than the declared sources. It has not been submitted to any examination body.

Berlin, 24. March 2023

Henrik Wiedenhaupt